Nano Energy 138 (2025) 110825

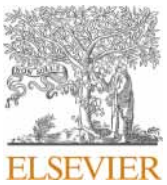

Contents lists available at ScienceDirect

Nano Energy

journal homepage: www.elsevier.com/locate/nanoen

Review

Triboelectric nanogenerators from fundamentals to applications

Doga Doganay [a,*], Mete Batuhan Durukan [a], Murathan Cugunlular [a], Onuralp Cakir [a], Melih Ogeday Cicek [b], Onur Demircioglu [a], Di Wei [c], Husnu Emrah Unalan [a,*]

[a] Department of Metallurgical and Materials Engineering, Middle East Technical University (METU), Ankara 06800, Türkiye
[b] NanoElectronics Group, MESA+Institute for Nanotechnology and BRAINS Center for Brain-Inspired Nano Systems University of Twente, Enschede 7500AE, the Netherlands
[c] Beijing Institute of Nanoenergy and Nanosystems, Chinese Academy of Sciences, Beijing 101400, China

ARTICLE INFO

Keywords:
Energy harvesting
Triboelectric nanogenerators
Contact electrifications
Theoretical models of TENGs
Energy harvesting efficiency
Energy transfer efficiency

ABSTRACT

Triboelectric nanogenerators (TENGs) represent an innovative approach to energy harvesting, enabling the conversion of mechanical energy into electrical energy through contact electrification and electrostatic induction. This review comprehensively covers the fundamental principles of TENGs, starting from the fundamental mechanisms of contact electrification, including electron transfer, ion transfer, and material transfer models. The review discusses four primary operation modes—vertical contact separation, lateral sliding, single-electrode, and freestanding—each with distinct operational characteristics and potential applications. Theoretical models, including equivalent circuit and quasi-electrostatic models used to predict TENG output are examined. Strategies to enhance energy harvesting and transfer efficiencies are discussed. The article concludes by discussing the wide-ranging applications of TENGs, from wearable electronics and biomedical devices to large-scale systems for environmental energy harvesting. This review serves as a comprehensive resource for researchers, providing both fundamental knowledge and insight into the latest technological advances in TENGs to guide future developments in this rapidly evolving field.

1. Introduction

There has been considerable interest in energy harvesting technologies in the 21st century, driven primarily by three key factors: environmental concerns, political considerations, and increasing energy demand. In recent years, developed countries have made significant investments in harvesting various energy sources to meet the growing global demands. Solar and wind energy are particularly notable as the energy sources receiving the highest levels of investment and research funding. The use of these natural resources offers significant advantages in terms of energy production on macro-scale (more than kW) to meet industrial and household consumption. With the development and widespread use of 5G technology, significant barriers are being overcome in Internet of Things (IoT) applications. Devices equipped with various sensors can communicate with each other via the Wi-Fi protocol, which is used not only in daily life for health monitoring but also in diverse fields, ranging from mass production lines to waste collection systems. The number of IoT devices is steadily increasing, with predictions indicating that 100 billion will be in use by 2030 [1]. These developments in the IoT fields have significantly increased the demand for decentralized energy sources at the micro-scale. This demand is often met by energy storage devices such as batteries and capacitors. However, their use in IoT applications presents several challenges. First, they need to be recharged at regular intervals. This leads to significant labor losses and increased costs in systems that are remote or require halting the production line for battery replacements. Additionally, wearable IoT devices become uncomfortable when used with traditional batteries. Micro-scale energy harvesting emerges as a promising solution to eliminate batteries or, at the very least, extend their charging intervals. Solar, thermal, and mechanical sources are often suggested in the literature as alternatives for micro-scale power generation, either as standalone or hybrid systems. Each has its own unique working principles, advantages and disadvantages over the others. Therefore, it is not right to suggest that one is better than the other. It is more practical to tailor the selection to the specific application, considering the consistency of the harvested energy source. For example photovoltaic cells harvest solar energy via photovoltaic effect. They can be constructed onto various substrates including flexible ones. While photovoltaic cells

* Corresponding authors.
E-mail addresses: doganay@metu.edu.tr (D. Doganay), unalan@metu.edu.tr (H.E. Unalan).

https://doi.org/10.1016/j.nanoen.2025.110825
Received 29 November 2024; Received in revised form 7 February 2025; Accepted 25 February 2025
Available online 26 February 2025

perform efficiently under favorable weather conditions, their effectiveness declines in cloudy or snowy weather' as well as indoor environments. Additionally, solar cells cannot meet the energy needs of systems designed to operate inside the body.

Mechanical energy can be harvested through a variety of methods, including electromagnetic generators (EMG), piezoelectric generators (PEG), and triboelectric nanogenerators (TENGs). EMGs have a long history of extracting mechanical energy, dating back to Faraday's discovery of electromagnetic induction in 1831 [2]. Electromagnetic induction is based on magnetic field changes along a conductor. EMGs produce high current and low voltage. Despite their historical importance, EMGs face challenges such as inefficiency at low frequencies and high weight due to the use of conductive copper coils and magnets. This makes them unsuitable for use in wearable and implantable devices. Alternatively, the piezoelectric effect provides another means to convert mechanical energy into electrical energy via PEG devices. These devices consist of two conductive electrodes attached to opposite sides of a piezoelectric material. When strain is applied to the material, an electric potential is created through piezoelectric charge polarization. This potential is balanced by the movement of free electrons between the conductive electrodes when connected with an external load. PEGs offer distinct advantages over TENGs and EMGs in certain applications, particularly due to their simple device structure. However, challenges arise in wearable applications due to the limitations of piezoelectric materials, which are often brittle. Additionally, the number of materials with unique crystal structures that exhibit the piezoelectric effect is limited, which places constraints on device design.

The use of contact electrification (triboelectrification) and electrostatic induction to harvest mechanical energy was first demonstrated by James Wimshurst (Wimshurst Machine) in 1891 and then by Robert J. Van de Graaff (the Van de Graaff generator) in 1929 [3,4]. However, for a long time, avoiding the negative effects of contact electrification has been a primary concern in both industry and scientific research. In 2012, Wang's research group demonstrated TENGs as mechanical energy harvesters using the combined effects of contact electrification and electrostatic induction as promising solutions for some of today's technology/energy problems at micro-scale [5–8]. Wang's works shifted the focus of triboelectrification research toward utilization rather than inhibition or prevention.TENGs have significant advantages over other mechanical energy harvesters. It is known that all kinds of surfaces are charged upon contact. This provides a wide range of material options in the development of TENG devices. Depending on the application, various materials and morphologies can be utilized, ranging from polymers to ceramics and metals, and from flat surfaces to fibers. Therefore, it is possible to fabricate cost-effective TENG devices using lightweight materials. Additionally, as will be explained in the following sections, the ability to create diverse device structures for different working modes allows for cost-effective, application-specific designs. Due to these advantages, interest in TENGs has been increasing since 2012. Fig. 1(a) shows the annual number of articles published each year from 2012 to 2024. The number of research articles increased each year, except in 2023. China, USA and South Korea are the three countries that publish the most TENG-related articles. Of all TENG-related publications, 49.0 % were from China, while 14.5 % and 11.4 % were from the USA and South Korea, respectively. Fig. 1(b) shows the number of published patents since 2016. The number of published patents related to TENGs increased, similar to research articles, except in 2023.

So far, 959 review articles have been published for TENGs. There are many valuable examples among these review articles. But almost all of them are written with a focus on certain applications or certain materials. For example, according to the WOS database, 204 review articles related to TENGs were published in 2024. Of these, 115 mainly focused on TENGs. Most of these studies (95 out of 115) written to explain the use of specific materials (such as MXene, cellulose-based TENGs) or morphologies (porous, fiber, 3D fractal TENGs) for TENGs, or applications (harvesting, sensing) of TENGs. However, none of them explain the basics of TENGs in sufficient detail, aside from a brief mention. Out of 959 review articles, only three stand out for their more comprehensive approach, covering the basics [9–11]. However, there are some missing concepts in these three important review articles. For example, Wang et al. cover only the electron transfer model for contact electrification in their review paper [9]. On the other hand, Coi et al. did not mention material transfer model for contact electrification, which is an important mechanism to explain contact electrification of polymers [10]. Physical models to explain the working mechanisms of TENGs and predict their outputs were not mentioned in any of these studies. However, understanding physical models is critical, especially for those new to the field to develop efficient TENGs. For these reasons, researchers in this emerging field often struggle to find a single source of fundamental information. Therefore, this article aims to comprehensively cover all critical aspects of TENGs, including contact electrification mechanisms, physical models, energy harvesting enhancement strategies, circuitry for energy transfer, and applications, ensuring no key components are overlooked. Although the article is worth reading for researchers at all levels, its main purpose is to guide researchers who are just starting to work in this important field. Therefore, this review covers the basic

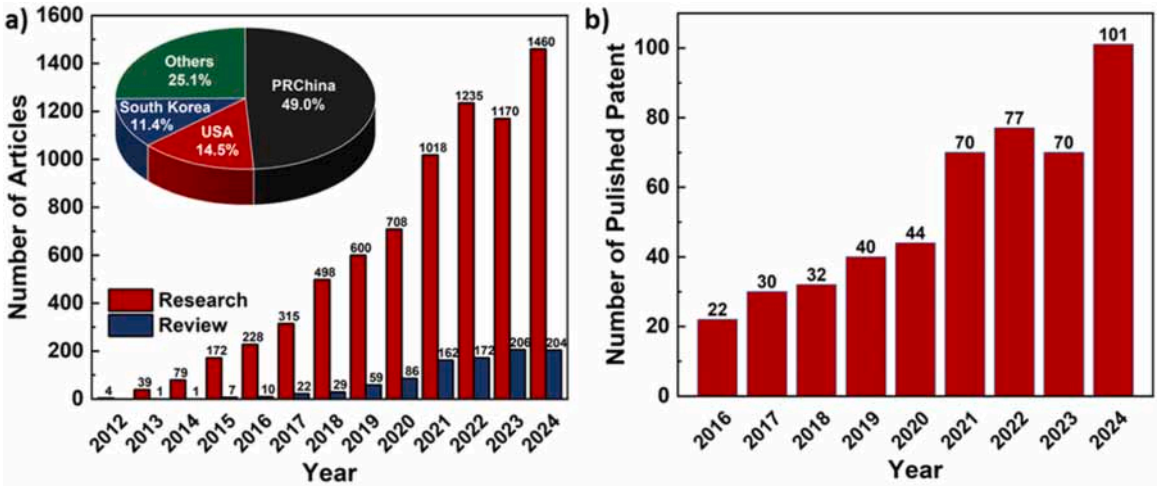

Fig. 1. Trends showing interest in TENG research. (a) Number of scientific articles published since 2012 according to WOS database. The inset figure shows the percentages of articles published by country. (b) Number of patents published since 2016 according to WIPO: PATENTSCOPE. "Triboelectric Nanogenerators" was the keyword for both article and patent searches. Only one patent was included from the same patent family.

processes of TENGs as concisely as possible.

2. Fundamentals of TENGs

This part of the review will cover the fundamentals of TENGs including the proposed mechanisms for the contact electrification, working modes and theoretical models of TENGs. Contact electrification can be observed in all surface pairs. These pairs can be solid-solid, solid-liquid, solid-gas, liquid-liquid, liquid-gas or gas-gas pairs. However, pointing out all contact pairs within this review article will shift the scope of it. Mostly solid-solid contact pairs will be discussed in the following parts, as most of the TENG articles utilize solid-solid pairs.

2.1. Contact electrification

Contact electrification is one of the first observed electrical phenomena in human history described as the "amber effect" in ancient times [12]. Initially, friction (rubbing) was thought to be necessary for electrification. For this reason, the phenomenon is also called triboelectrification. Today, it is known that surface contact is sufficient for electrification. Contact electrification was first reported by Plato in his Timaeus (300 BCE) [13]. Its effects on our lives have been quite significant. Even the origin of life is thought to be the result of the contact electrification [14]. Surprisingly, little progress has been made since Plato's time in understanding the mechanism of the triboelectric effect. Discussions regarding the mechanisms of contact electrification have been going on in the same scope for centuries [15,16].

William Gilbert conducted the first scientific research on contact electrification and published his findings in his book De Magnete in 1600 [17]. Gilbert rubbed different types of materials and tried to attract or repel light bodies with the rubbed materials. He classified materials that are charged after rubbing and attract light objects as "electrics", and those that are not charged after rubbing as "analectrics" (Today we know that all materials are charged to some degree upon contact). He also stated that charged objects only attract but not repel other objects. Later, Charles du Fay falsified this statement by discovering charge duality and showed that the materials having the same charge repel each other [18] (Later, Benjamin Franklin described these charges as negative and positive [19]). In du Fay experiments, he observed that some materials became positively ("vitreous" by his definition) charged, while others became negatively ("resinous" by his definition) charged when rubbed with his skin or silk. But later it was observed that the same material can have positive or negative charge, depending on the material it is rubbed with. These observations forced scientists to categorize materials empirically in a triboelectric series. Materials are ranked in the triboelectric series based on the sign and magnitude of the charge they acquire when rubbed against other materials. The triboelectric series consisting of common materials is provided in Fig. 2. Materials in the positive region of the series tend to be positively charged, while materials in the negative region tend to be negatively charged. However, since the first triboelectric series was reported by Wilcke in 1757, many conflicting results have been expressed [20]. For example, in 1917 Shaw showed that mechanical deformation changes material's position in the triboelectric series [21]. In addition, in 1926, he proved that identical materials are charged oppositely when they contact each other [22]. These conflicting results show that contact electrification is not only dependent on the chemical composition of materials but also on other factors. Resolving these contradictions requires understanding the mechanism of contact electrification. Nonetheless, the actual mechanism -or the dominant mechanisms according to the conditions- remains unclear. There are several reasons for these contradictions and uncertainty. For example, surface charge densities that create high potential are quite low (approximately one elementary charge per 100,000 surface atoms). Therefore, possible contamination and surface roughness significantly affect the potential created by surface charge. Moreover, surface morphology, intermolecular adhesion between contacting materials, and the humidity of the measurement environment have a drastic effect on triboelectrification [23–28]. This makes it difficult to measure contact electrification and understand its nature. The types of contact pairs are also important to clarify the mechanisms of contact electrification. For example, electron transfer can explain contact electrification for metal contact pairs. However, it is not sufficient to illustrate contact electrification if one of the contact materials is an insulator. Moreover, if the ion transfer mechanism is not taken into account, the effect of relative humidity on contact electrification will remain unclear. The following sections will discuss the proposed mechanisms along with their significant experimental evidence.

Fig. 2. Triboelectric series including commonly used materials for TENGs.

2.1.1. Electron transfer

Electron transfer was initially thought to be the mechanism of contact electrification. Early models were based on band diagrams of the materials. Valence and conduction bands overlap for metals and electrons can move from one metal to another without encountering the energy barrier upon contact. Therefore, the mechanism of contact electrification between metal-metal surfaces is agreed to be electron transfer [29,30]. When two metal surfaces come into contact electrons flow from the metal having lower work function to the one with the higher work function until the system reaches a thermodynamic equilibrium state. Transferred electrons tunnel back as these metals are separated if the distance is small. Tunneling becomes difficult when the distance between the metal surfaces increases and stops after a critical separation distance (around 100 nm) As a result, the surfaces become charged, as schematically shown in Fig. 3 **(a)**. Experimental results show the correlation between work function and surface charges of metal-metal contact pairs [29]. However, metals always form an oxide layer under atmospheric conditions. Consequently, the insulating oxide layers prevent the two metal surfaces from making direct contact. This necessitates a more inclusive explanation for the contact electrification between metal-metal surfaces.

Contact electrification between insulators via electron transfer is more difficult since insulators have large band gaps. Transferring an electron from the valence band to the conduction band for insulators requires high thermal energy ($kT \approx 0.0026$ eV) [31]. On the other hand, it is known that insulators charge more than metals upon contact. The existence of surface/defect states within the band gap was proposed to explain the mechanisms of electron transfer in insulators. Electrons located in intermediate states (surface or defect) within the band gap are often regarded as the electron source (schematically shown in Fig. 3 **(b)**). However, the number of electrons located in the intermediate states are lower than the charge created by contact electrification [32].

Recently, Wang et al. stated that electron transfer is the dominant mechanism for contact electrification for all solid-solid pairs [33]. An interatomic interaction model was developed to explain electron transfer for contact electrification in their work. According to the interatomic interaction model for contact electrification, electron transfer occurs between two materials when the interatomic distance between the materials is shorter than bond length (repulsive force regime). In this regime electron clouds of the atoms overlap with each other. As a result of this overlap, separate potential wells of the atoms become asymmetric double wells. The potential barrier between two atoms is lowered, resulting in electron transition from one atom/-molecule to the other atom/molecule schematically shown in Fig. 3 **(c)**. The transferred electrons remain in their new positions as the atoms separate, unless thermionic or photoelectron emissions occur. This model does not necessitate an intermediate state to explain electron

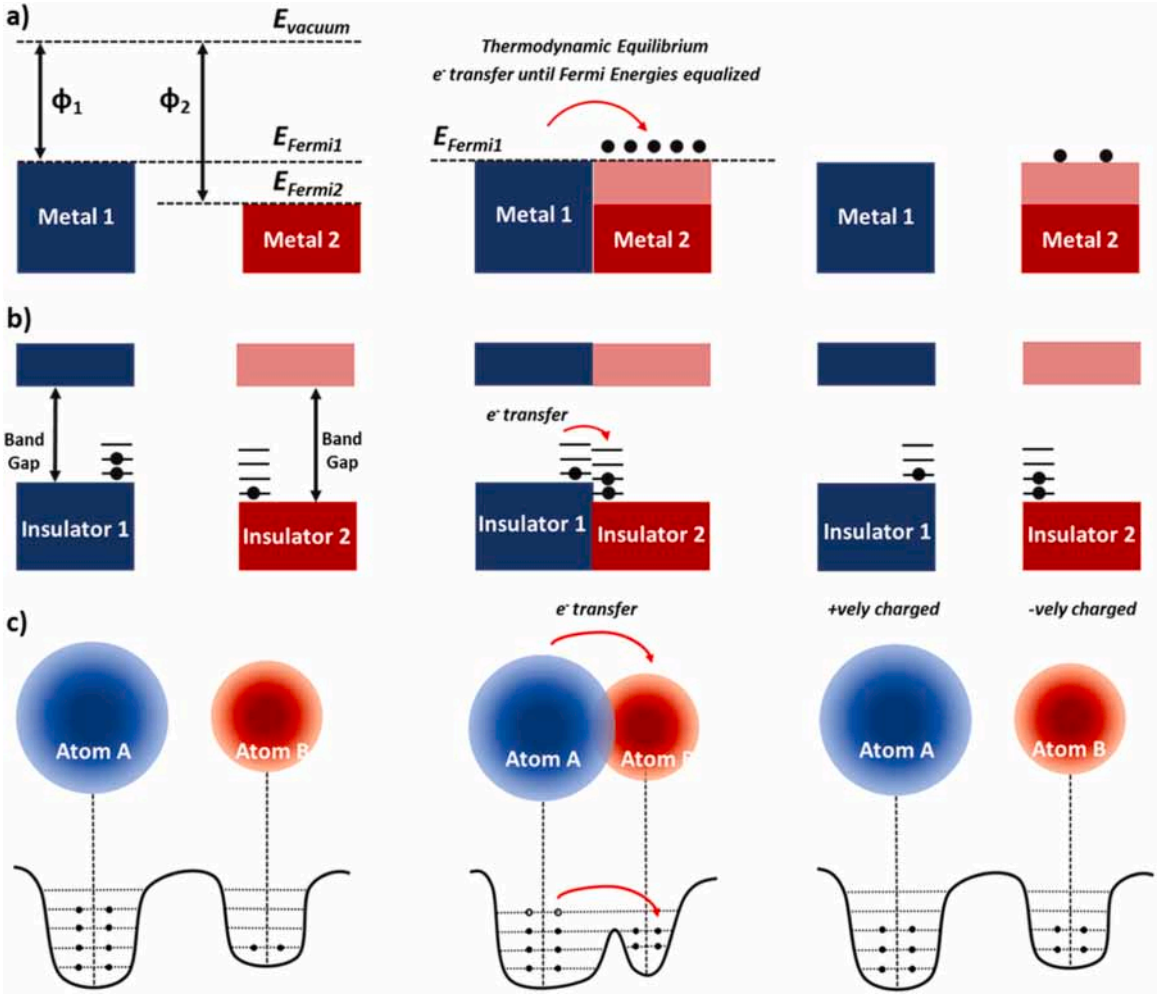

Fig. 3. Electron transfer mechanisms for contact electrification. Schematics of electron transfer mechanism based on energy band model for contact electrification of (a) metal-metal and (b) insulator-insulator surface pairs. (c) Electron-cloud-potential-well model of electron transfer mechanisms for contact electrification. (c) Adapted with permission from Ref. [33]. Copyright 2019, Elsevier.

transfer between insulators.

There are several studies that were conducted to elucidate electron transfer mechanisms for insulators in the late 2000s and early 2010s. For example, Liu and Bard charged two polymers by rubbing and used the negatively charged polymer to drive some electrochemical reactions like metal deposition, chemiluminescence, and hydrogen formation [34–36]. According to their results, negatively charged polymers were able to drive the reactions. They concluded that electron transfer is the charging mechanism for contact electrification because electrons are needed to carry out these reactions. However, observed charge densities of contact electrification as the result of their experiments were higher than the theoretical calculations [35]. Then, Baytekin et al. stated that it was the mechanoradicals produced by the mechanical stress during contact electrification that carry out these redox reactions instead of the transfer of electrons [37]. Additionally, they demonstrated that the positively charged polymer can also facilitate these electrochemical reactions. Therefore, these reactions are not exclusively driven by transferred electrons; if they were, the positively charged polymer would not be able to carry them out. It should also be noted that solid-liquid contact electrification can also trigger electrochemical reactions [38,39]. Therefore, contact electrification chemistry will be an important tool to understand contact electrification mechanisms.

2.1.2. *Ion transfer*

Ion transfer model has also been proposed as the origin of contact electrification [29–31]. There are basically two approaches that existed in this model depending on the type of insulators in contact. If the contact materials contain mobile ions, contact electrification occurs as the result of mobile ion transfer. A schematic representation of this model is provided in Fig. 4 **(a)**. In the schematic, cations are covalently bonded to the polymer and anions are mobile (The same mechanism is valid if the anions are covalently bound, and the cations are mobile). When two surfaces come into contact, mobile ions are transferred from the ionic polymer to the other surface. Mendley used ion exchange resins to prove this mechanism [40]. The resins were charged with the same sign as the covalently bonded ion since mobile ions were transferred to the contacted surface. Later, Diaz et al. extended this work with different ionic polymers and observed that ion-containing polymers are always charged with the same sign of covalently bound ions [41,42]. They also showed that increasing the concentration of mobile ions increases surface charge. These results showed that ion transfer is an important mechanism for contact electrification of ionic polymers.

Mobile ion transfer mechanism, however, is not sufficient to explain contact electrification of non-ionic polymers. Therefore, the ion transfer model was improved to also explain the contact electrification of non-ionic polymers. Diaz et al. suggested a water bridge model to explain the ion transfer mechanism for both ionic and non-ionic polymers [23]. This model is based on the fact that, less than 0.5 nm thick water film is adsorbed from the ambient atmosphere on the polymer surfaces (including hydrophobic polymers). According to this model, mobile ions

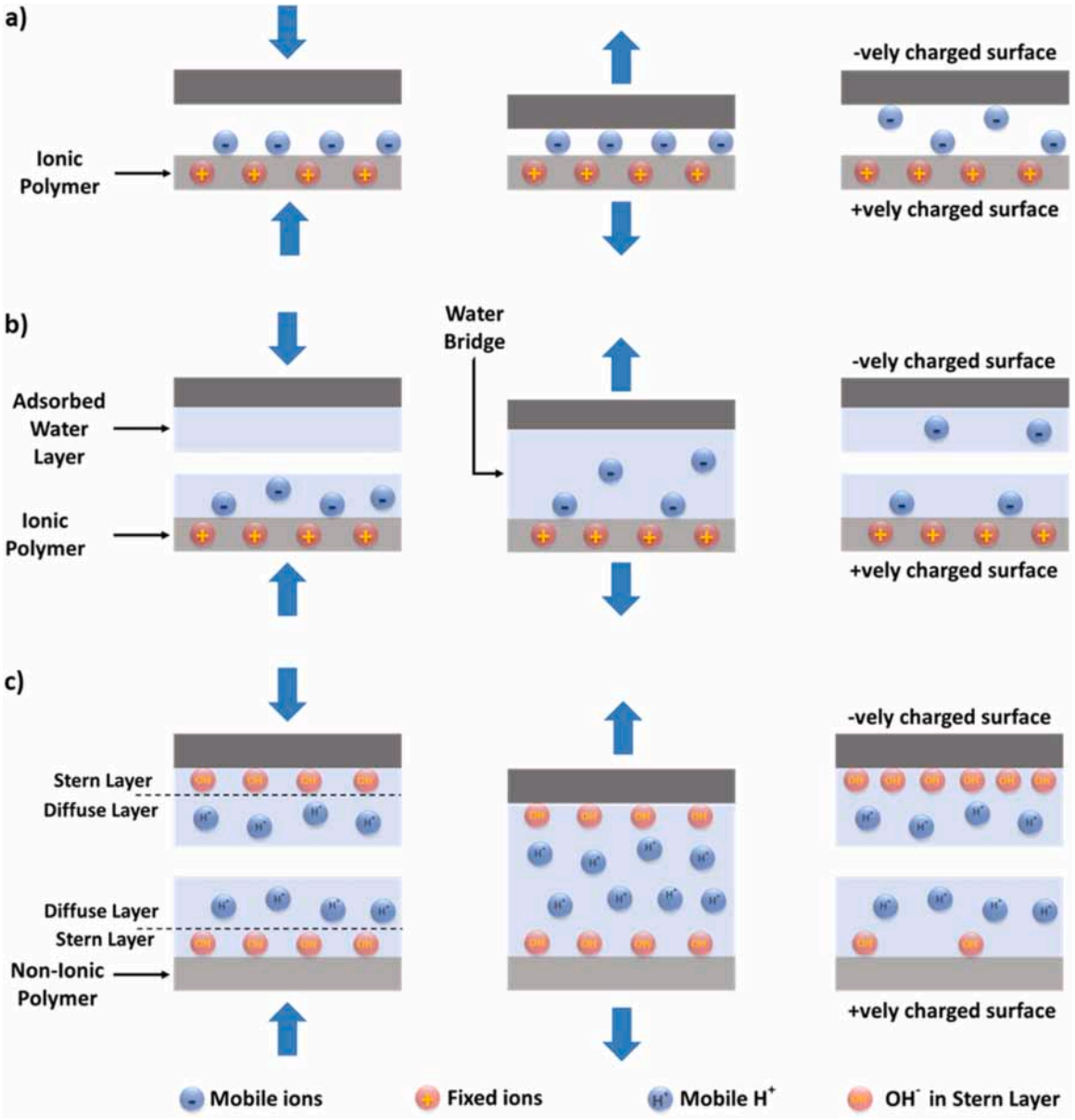

Fig. 4. Ion transfer and water bridge models for contact electrification in polymers. Schematic representation of (a) ion transfer model of contact electrification for ionic polymers. Schematic representations of water bridge model to explain ion transfer mechanism of contact electrification for (b) ionic and (c) non-ionic polymers. (a)–(c) Adapted with permission from Ref. [31]. Copyright 2008, Wiley-WCH.

of ionic polymers are redistributed onto surfaces upon contact as schematically represented in Fig. 4 **(b)**. Since the dielectric constant of water is quite high, the mobile ions can be separated from their counterions by overcoming electrostatic forces and the surfaces are charged. On the other hand, the source of the contact charges is OH^- ions for non-ionic polymers. OH^- ions are accumulated in the Stern layer and H^+ ions are dissolved in the diffuse layer. Once two polymers are in contact, the OH^- ions are redistributed onto the surfaces of the polymers depending on the OH^- accumulation affinities of the surfaces. The surface having more OH^- ions is negatively charged and the surface having less OH^- ions is positively charged as schematically shown in Fig. 4 **(c)**. OH^- adsorption affinities of the surfaces can be characterized by Zeta-potential analyses [31]. A positive correlation between Zeta potential and contact electrification for several polymers was also reported [31]. This correlation can explain the position of these polymers in triboelectric series yet there are also some contradictory cases reported in the literature [16]. Moreover, Whitesides et al. showed that contact charging of polystyrene increases in an alkaline environment and decreases in an acidic environment [43]. Their results support the OH^- adsorption model for contact electrification.

The effects of relative humidity on contact electrification were investigated in different studies to validate the water bridge model [23, 25,43]. The research statement behind these studies was: if the water bridge model is valid, the difference in relative humidity will affect the contact charge. This was because the thickness of the water adsorbed on the polymer surfaces changes with relative humidity. In one of these studies, Whitesides et al. observed that surface charge increases in higher relative humidity [43]. Diaz et al. also investigated the effect of relative humidity on the contact electrification [23]. They observed an increase in contact electrification up to 30 % relative humidity, followed by a decrease above 40 % relative humidity. They attributed this decrease to the increase in the conductivity of the surface which may cause a discharge of the contact charge. More recently, Baytekin et al. conducted several contact electrification experiments at zero humidity and showed that water is not necessary for contact electrification, yet it increases the amount of contact charge [25]. However, there are also

conflicting cases reported in literature. For example, Sutka et al. reported a significant increase in contact electrification at temperatures exceeding 100 °C, where water adsorption is minimal [44]. This significant increase in contact electrification has been attributed to enhanced material transfer, as the polymers used by Sutka et al. become rubbery at the reported temperatures. In another study, poly(tetrafluoroethylene) (PTFE) was similarly charged under vacuum and air in Homewood's experiment [45]. More interestingly, Wang et al. showed that contact electrification increases under vacuum since, the air breakdown effect (the discharge of contact charges) decreases [46]. In addition, contact electrification between identical polymers has been reported multiple times [22,47]. These studies demonstrate that ion transfer is not the only mechanism, as the OH^- adsorption affinities of identical materials should be the same. These results indicate that the role of adsorbed water has different effects on contact electrification under different conditions and contact pairs.

2.1.3. Material transfer

Material transfer has been considered as one of the contact electrification mechanisms since 1960s. In 1962 Henniker thought that free radicals produced by mechanical stress during contact electrification generated high-energy electrons that can be easily excited to the conduction band [48]. Later, material transfer from polymer surface to metal surface resulting from polymer-metal contact was shown via Auger electron spectroscopy in early 1970s [49,50]. Soon after, Salaneck et al. observed material transfer between polymer-polymer surfaces via X-ray photoemission spectroscopy [51]. They suggested that the amount of material transferred was sufficient to explain the amount of charge created by contact electrification. Later, magnetic force microscopy (MFM) and electron paramagnetic resonance (EPR) techniques revealed that polymer chains fracture and mechanoradicals and mechanoions are generated by bond cleavage when two polymer surfaces are in contact. Mechanoradicals are generated with homolytic bond cleavage whereas, mechanoions are generated with heterolytic bond cleavage upon contact [52]. Basically, in homolytic bond cleavage, each part of the broken chain receives one of the shared electrons of a covalent bond, whereas in heterolytic cleavage, both shared electrons of a covalent bond are taken by one part of the broken chain. In this case, it

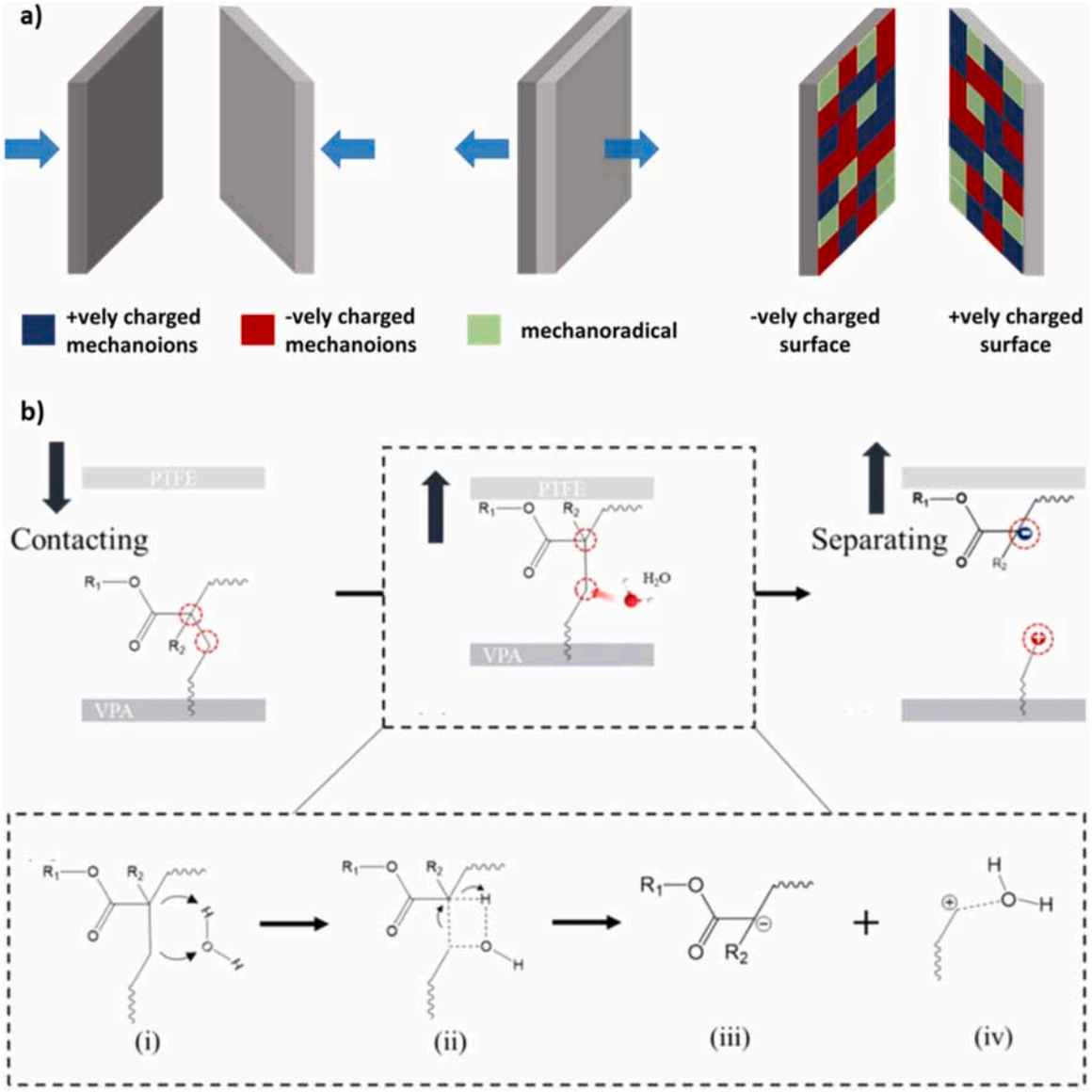

Fig. 5. Material transfer model explaining contact electrification. **(a)** Schematic representation of the mosaic charge pattern of two surfaces after contact electrification. **(b)** Schematic representation of mechanoion formation with water assisted heterolytic bond cleavage (b) Reproduce with permission from Ref. [55] Copyright 2024, Royal Society of Chemistry.

would be reasonable to state that the created surface charge is a result of heterolytic bond cleavage. Schematic representation of contact electrification with material transfer mechanisms is provided in Fig. 5 **(a).** According to this model, adhesion between the surfaces, chain entanglement, crosslinking and non-covalent domain interaction causes bond cleavage. In fact, the first ionization energy (670–890 kJ/mol) (the minimum energy for electron transfer) is higher than the energy required for homolytic bond cleavage (360–430 kJ/mol for C-C bond) [53,54]. In other words, homolytic bond cleavage is energetically favorable than electron transfer. However, there is an electrostatic attractive force between the newly formed charged chains in heterolytic bond cleavage. Therefore, the energy required for heterolytic cleavage is higher than homolytic bond cleavage. That means, the formation of mechanoradicals should be energetically more favorable than the formation of mechanoions. Recently, Fu et al. claimed that polar structures like water in the environment assist mechanoion formation [55]. Schematic representation of heterolytic bond cleavage during contact electrification of PTFE and viscoelastic polymer adhesive (VPA) pair is provided in Fig. 5 **(b).** C—C bond of the polymer chain is stretched due to adhesion, crosslinking and chain entanglement. Adsorbed water on the surface acts as a nucleophilic agent and facilitates heterolytic bond cleavage by reducing energy cost. Carbon atoms interact via dipole-dipole and dipole induced dipole interactions with oxygen and hydrogen, respectively. Further separation causes the formation of new polymer chains with opposite charges. According to the schematics, the negatively charged chain is transferred to the PTFE surface. Positively charged polymer chain remains on the VPA matrix.

When radical scavengers such as Vitamin E, DPPH (1,1-diphenyl-2-picrylhydrazil) and lignin are added to the polymer matrix, the amount of contact charge is significantly reduced [56–58]. These radical scavengers stabilize (neutralize) the radicals formed as a result of contact. For centuries, surfaces were believed to become entirely positively or negatively charged upon contact. This assumption was first disproven with the advent of equipment designed for surface characterization. In 1989 Terris et al. reported bipolar charge exchange between the polymer surface and the tip of the force microscope [59]. That is, they detected both negatively and positively charged macroscopic regions on the polymer surface that came into contact with the tip of the force microscope. Later, in 2011, Baytekin et al. reported that the polymer surfaces have randomly distributed charges with opposite signs at nanoscopic dimensions after contact (schematically shown in Fig. 5(a)) [60]. In this study, XPS analyses showed that the mosaic charge patterns arise as the result of material transfer. Later on, contact electrification between microdome patterned PDMS and flat gold surface is investigated [61]. Upon contact, the flat gold surface charged with the same PDMS microdome pattern is observed using Kelvin probe force microscopy (KPFM). This result suggests that contact electrification on the gold surface is due to material transfer. If electron transfer were the sole mechanism, the charges would be evenly distributed across the gold surface, given its conductive and equipotential nature. In another study, PTFE beads are rolled onto a PMMA dish for a certain time. Initially, the PMMA dish is positively charged, but after some time, the charge polarity reverses [62]. This is attributed to the accumulation of transferred material on the surfaces. After a certain accumulation, the transferred materials are transferred back to the opposite surface. These results show that material transfer is an important mechanism in contact electrification for metal-polymer and polymer-polymer pairs.

There are several important studies reported in literature which investigate the relationship between mechanical properties of surfaces and contact electrification. In one of these studies, the polyvinyl chloride (PVC) and polydimethylsiloxane (PDMS) pair is investigated with different PDMS curing ratios [63]. The variation in the PDMS curing ratio leads to differences in its mechanical properties. It is observed that softer PDMS has a higher number of surface charges compared to harder counterparts. XPS analyses showed that the degree of material transfer is higher when PDMS is softer. In addition, the mechanical strain applied to the polymers changes the sign and amount of contact charge [64–66]. Natural rubber is examined for these purposes in different studies. In one of these studies PTFE is negatively charged when contacted with unstretched rubber and positively charged when contacted with stretched rubber. Contact charging between chemically identical materials having different elastic deformation also proves the effect of mechanical strain on contact electrification [66]. The material transfer mechanism instinctively suggests that the effect of adhesion between contact surfaces is important. One can state that increased adhesion force should increase material transfer. In fact, there are important studies in literature that confirm this statement [28,67,68]. In one of these studies, Shi et al. showed that increased adhesion force promotes mechanoion formation, resulting in higher surface charges [67]. In another study, Sherrell et al. conducted a set of contact electrification experiments by creating 196 contact pairs with 14 different polymers [68]. It has been reported that softer polymers are negatively charged, while harder polymers are positively charged. It is claimed that the adhesive force between the polymers and the cohesive energies of the polymers determines the amount and sign of the surface charge. In summary, these studies along with other examples discussed in review articles (focusing specifically on contact electrification mechanisms) show that material transfer plays a significant role in the contact electrification of polymer surfaces [69,70].

In summary, the precise or dominating mechanism for the contact electrification of insulating materials is complex and requires extensive investigation. The origin of contact electrification seems to remain a mystery for a while. The invention of TENGs increased the attention to explain the origin of contact electrification and accelerated the studies conducted in this field. Hopefully, this attention will result in a universal explanation of contact electrification. This understanding will also help engineers design more efficient TENGs with higher energy conversion capabilities.

2.2. *Working modes of TENGs*

There are four operating modes of TENGs depending on the arrangement of the triboelectric and conductive layers, their relative motion, and the direction of charge polarization. The term “triboelectric layer” describes the layer that charges on contact. These charges are stationary. On the other hand, free electrons are induced from the “conductive layer” when there is a potential difference. Fig. 6 schematically illustrates these TENG modes.

The most basic mode of TENGs is the vertical contact separation mode. In this mode, the two electrodes physically come into contact and are separated by a certain distance. Triboelectric layers are oppositely charged as a result of contact. A potential difference occurs when the charged electrodes are separated from each other by external forces. When conductive layers are connected to an external load, electrons flow from one electrode to the other to balance the potential difference. Once the gap between the electrodes decreases, electrons flow in the opposite direction from the external load. As a result of this periodic motion, an alternating current is generated. The vertical contact separation mode offers advantages over other modes due to its simple design and ease of manufacture. Also, electrode life in this mode is higher than that in lateral sliding and freestanding modes. This is because in vertical contact separation mode there is very low wear acting on the electrodes.

In the lateral sliding mode, a potential difference exists between two electrodes due to lateral sliding of the electrodes. Electron flow occurs between the electrodes from the external load to balance the potential difference. Periodic sliding from one direction to the other results in an alternating current. The lateral sliding mode provides higher conversion efficiency than the vertical contact-separation mode because more contact charge is generated through friction. However, the electrode lifespan is limited due to increased wear.

Vertical contact separation and lateral sliding modes consist of two electrodes connected to each other via an external load. This structure

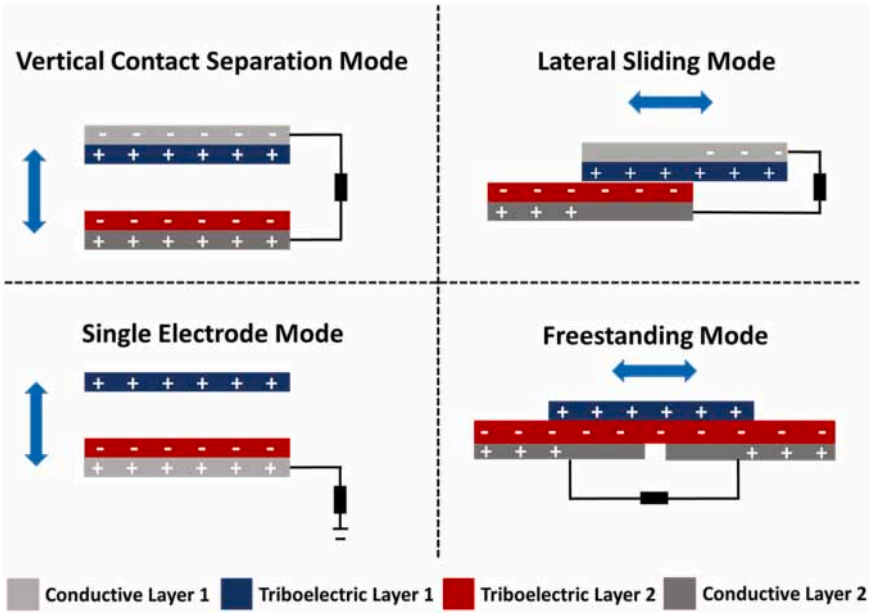

Fig. 6. Schematic illustrations of four fundamental working modes of TENGs. For each working mode dielectric materials are used as the triboelectric layer. However, conductive layers can also be used as triboelectric layers in certain TENG designs.

limits their applications when energy is converted from freely moving objects. On the other hand, the single electrode mode consists of one electrode connected to the ground with an external load. Electrons flow between the fixed electrode and the ground as the moving triboelectric layer approaches and moves away. The second triboelectric layer can freely move without an electrical connection to the system. This mode offers design advantages, but its power output is less than the other modes. In addition, the output signals are highly sensitive to coupled noise compared to other modes.

In freestanding mode, the two conductive layers are interconnected by an external load. A triboelectric layer is placed on top of these conductive layers. An asymmetric charge distribution is observed when the second triboelectric layer is brought in contact with the electrode. Electron flows are observed between the conductive layers which reduce the potential difference. This mode offers design advantages along with high conversion efficiency. However, electrode durability is limited due to excesive wear acting on the electrodes.

2.3. *Theoretical models of TENGs*

A comprehensive examination of theoretical models is essential for a deeper understanding of TENGs. In this section, we present the basic concepts underlying these models, without delving too far into mathematical derivations. For clarity and simplicity, the discussion on theoretical models will focus on the vertical separation mode.

It is appropriate to give a brief overview of the TENG energy harvester system, before discussing the various theoretical models. In general, the system consist of three basic components: mechanical input, TENG transducer and power management circuits. Fig. 7 schematically shows the above-mentioned components, where mechanical energy is converted into electrostatic energy within the TENG and then extracted as electrical energy by the power management circuit.

Two basic approaches exist to theoretically explain the operational mechanisms of TENGs: Equivalent circuit models and formal physical models, in other words, quasi-electrostatic models. Equivalent circuit models are built on lumped parameter models and depict TENGs as circuit elements that are voltage/current sources with inherent capacitance/impedance. In contrast, formal physical models are based on classical electromagnetic theory, primarily emphasizing the internal dynamics of the TENGs through the employment of Maxwell's equations. Please note that there are also other models proposed in literature like electromechanical coupling models, and models for tribovoltaic nanogenerators [71,72]. For the sake of simplicity, this review will cover equivalent circuit models and formal physical models specifically for contact separation modes, as they are used more frequently in literature.

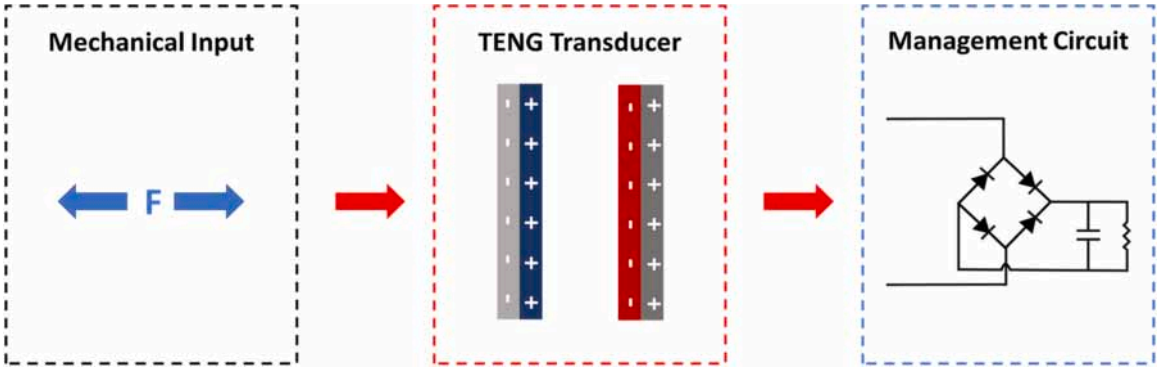

Fig. 7. Overall energy harvesting system via TENGs. Mechanical energy transformed into electrostatic energy within the TENG transducer then extracted to electrical energy by the management circuit.

2.3.1. Equivalent circuit models

2.3.1.1. Capacitive model. Capacitive model is the first theoretical model proposed to explain working principles of TENGs and predict their outputs [73–75]. A typical dielectric-dielectric TENG in vertical contact separation mode consists of two triboelectric layers and two conductive layers as schematically shown in Fig. 8 **(a)**. The potential difference between the two conductive layers can be represented by,

$$V = \frac{-Q}{C(x)} + Voc(x), \tag{1}$$

where Q is the transferred (induced) charges between the two conductive layers, $C(x)$ is the capacitance of the TENG system and $Voc(x)$ is the voltage generated by the separation of contact charges. Note that $C(x)$ and $Voc(x)$ are separation distance dependent. Eq. (1) is the relationship between V-Q-x and described as the governing equation of the capacitive model.

Two dielectric layers have thicknesses of d_1 and d_2, and relative dielectric permittivities of ε_{r1} and ε_{r2}, respectively (shown in Fig. 8 **(a)**). The dielectrics are positioned face to face with a distance of $x(t)$. Two conductive layers are deposited or attached to the outer surface of the dielectrics. The inner surfaces of the dielectrics are oppositely charged with a charge density of σ (contact charge) upon contact. Q is the induced charge at the conductive layers. The potential difference between two conductive electrodes is V, that develops upon separation of the dielectric layers. The area of the electrodes is A, which is larger than the total distance ($d_1 + d_2 + x$) between the conductive layers. Therefore, the electrodes are assumed to be infinitely large. Based on these the potential difference between two conductive layers can be represented by:

$$V = E_1 d_1 + E_2 d_2 + E_{air} x, \tag{2}$$

where E_1, E_2 and E_{air} are electric field strengths inside d_1, d_2, and air, respectively. Electric field strength for each can be calculated from the Gauss theorem.

$$E_1 = -\frac{Q}{A\varepsilon_0\varepsilon_{r1}}, \tag{3}$$

$$E_2 = -\frac{Q}{A\varepsilon_0\varepsilon_{r2}} \tag{4}$$

$$E_{air} = \frac{-\frac{Q}{A} + \sigma(t)}{\varepsilon_0} \tag{5}$$

When Eqs. (2)–(5) are combined, voltage becomes:

$$V = -\frac{Q}{A\varepsilon_0}\left(\frac{d_1}{\varepsilon_{r1}} + \frac{d_2}{\varepsilon_{r2}} + x\right) + \frac{\sigma x(t)}{\varepsilon_0} \tag{6}$$

If effective field strength d_0 is defined as $\frac{d_1}{\varepsilon_{r1}} + \frac{d_2}{\varepsilon_{r2}}$, then V-Q-x relation becomes:

$$V = -\frac{Q}{A\varepsilon_0}(d_0 + x(t)) + \frac{\sigma x(t)}{\varepsilon_0} \tag{7}$$

The Eq. (7) can be used to calculate output performance of TENGs. Note that the Eqs. (1) and (7) are the same since $C(x) = \left(\frac{A\varepsilon_0}{(d_0 + x(t))}\right)$. Under open circuit conditions, Q is 0. Thus, open circuit voltage (Voc) becomes;

$$Voc = \frac{\sigma x(t)}{\varepsilon_0} \tag{8}$$

Under short circuit conditions, V is 0. Thus, short circuit charge and current are;

$$Qsc = -\frac{A\sigma x(t)}{d_0 + x(t)}(d_0 + x(t)) \tag{9}$$

$$Isc = \frac{dQsc}{dt} = \frac{A\sigma d_0}{(d_0 + x(t))^2}\frac{dx}{dt} = \frac{A\sigma d_0 \nu(t)}{(d_0 + x(t))^2} \tag{10}$$

The output properties can be predicted when a resistor load is

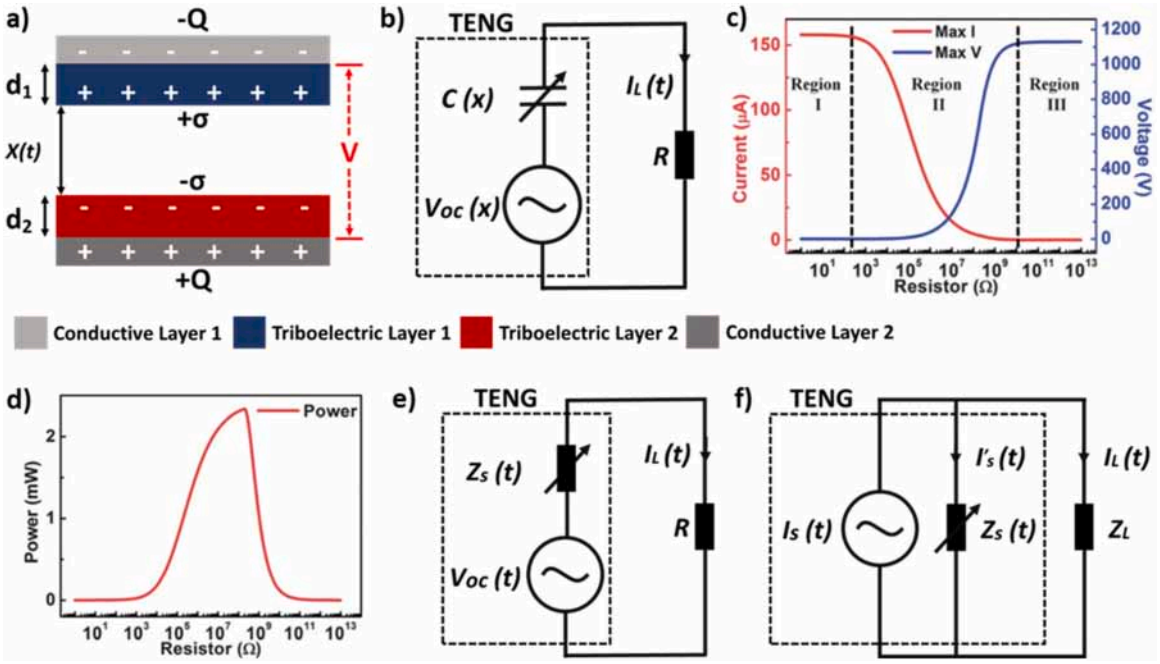

Fig. 8. Equivalent circuit models of TENGs. (a) A model of dielectric-dielectric TENG working in contact separation mode. (b) Circuit representation of TENG device as a voltage source and inherent capacitance. Theoretically calculated TENG outputs of (c) peak voltage and current, (d) power output under different resistance loads. (e) Thevenin's model consists of a voltage source and inherent impedance, (f) Norton's model consisting of a current source and inherent impedance. (a), (c) and (d) adapted/reproduce with permission from Ref. [74]. Copyright 2013, Royal Society of Chemistry. (b) Adapted with permission from Ref. [75]. Copyright 2013, Elsevier. (e), (f) adapted with permission from Ref. [76]. Copyright 2018, Wiley-VCH.

connected to TENGs (circuit drawing in Fig. 8 **(b)**) by combining governing *V-Q-x* Eq. (7) and Ohm's law;

$$R\frac{dQ}{dt} = -\frac{Q}{A\varepsilon_0}(d_0 + x(t)) + \frac{\sigma x(t)}{\varepsilon_0} \tag{11}$$

The equation is a first order differential equation and can be solved by defining boundary conditions [72–74]. The initial boundary condition is $Q = 0$ when $(t = 0)$. The final boundary condition is $Q(t) = Q$. With the help of these boundary conditions and defining periodic motion of the electrodes, output voltage, charge and current of the device can be predicted provided that different resistor loads are connected between conductive layers.

Theoretically calculated output voltage, current and power of a TENG system working in vertical contact separation mode are graphically provided in Fig. 8 **(c)–(d)** (Please refer to [74] for the details of TENG system and parameters). When a small load resistance is connected to the conductive layers, induced charges are easily transferred from one conductive layer to the other. On the other hand, high load resistance limits this charge transfer. Differences in charge transfer rates cause the difference for output current as can be deduced from Eq. (10). That is, when the resistance load is high, output current is low and vice versa. Unlike current and charge, the output voltage is high when the load resistance is high. This is because the high resistive load limits the charge transfer and potential difference cannot be balanced with induced electrons. The peak values of output current and voltage under different load resistances are graphically provided in Fig. 8 **(c)**. This graph can be divided into three different regions. Resistance load is low in Region I and current is approximately equal to short circuit conditions. The TENG device works as a current source. On the other hand, the device works similar to open circuit conditions when load is high (Region III). Therefore, output voltage is approximately equal to *Voc*. Current starts to decrease while voltage increases in Region II, when the load resistance is in the medium range. Therefore, output power is maximum in Region II, which can be seen in Fig. 8 **(d)**. The output power can be maximized as the impedance of the TENGs matches the load resistance.

2.3.1.2. Thevenin's and Norton's models. The capacitive model represents TENGs as an ideal voltage source and capacitor, both of which vary with time as discussed in the previous section. In this model the inherent impedance of the TENG system is modeled without a resistor and includes only a capacitive element as depicted in Fig. 8 **(b)**. On the other hand, inherent impedance of TENGs is considered as the circuit element in Thevenin's and Norton's models, which have been used since the 1880s to simplify complex circuits. In Thevenin's equivalent circuit model, the TENG system is represented by a serially connected voltage source and an inherent impedance element (provided in Fig. 8 **(e)**). Basically, the capacitor element is replaced with an impedance element. In Norton's equivalent circuit model, on the other hand, the TENG system is represented by a time-varying current source and a parallel connected inherent impedance element as schematically shown in Fig. 8 **(f)**.

Modeling the TENG system with Norton's equivalent circuit is important when the TENG devices have high inherent impedance. Reliable measurement of open circuit voltage may be difficult when the inherent impedance of the TENG system is too high since voltage measurement units have limited impedance. The generated current is divided between $Z_s(t)$ and load impedance when external load is connected in parallel to the TENGs. The current passing through the load at time t can be calculated by Eq. (12):

$$I_L(t) = I_S(t)\frac{Z_s(t)}{Z_S(t) + Z_L} \tag{12}$$

The power output of TENGs can then be calculated by:

$$P_{out}(t) = I_L(t)^2 Z_L \tag{13}$$

The maximum power from TENGs is attained when the load impedance is close to the inherent impedance of the TENG system.

2.3.2. Formal physical (quasi-electrostatic) models

The capacitive model discussed in the previous section is highly useful for predicting TENG outputs. However, this model is limited in explaining the internal dynamics of the TENG transducer. New models that relied on classical electromagnetics are proposed to overcome the limitations. These models are based on the calculation of the potential difference created by a charge at any point. The first model based on classical electromagnetics was proposed by Dharmasena et al. named as the distance dependent electrical field (DDEF) model [76–78]. Later, Shao et al. developed a 3D mathematical (finite-sized charged plane (FSCP)) model. In the following sections, these models will be briefly discussed [72,79,80]. In TENG systems, dielectric layers are charged as the result of contact electrification. These charges are static and upon separation, electrons are induced at the electrodes that are attached at the back side of the dielectrics. The electric field inside the dielectric and at the dielectric-electrode interface is only resulted from induced charge (effect of contact charge is neglected) in the parallel plate capacitor model. On the other hand, the situation is slightly different in the real case for TENGs. That is, the electric field propagating inside the dielectrics is not only due to induced charges but also due to contact charges (static charges at the dielectric) until it is shielded by electrodes.

2.3.2.1. Distance dependent electrical field (DDEF). In the DDEF model, electric field variation along the z-axis for a charged surface placed in the x-y plane can be derived from Gauss's law. Consider a uniformly charged plane with a charge density σ in the length (L) and width (W) dimensions. The total electric field along the z-axis above the midpoint of the plane can be obtained by dividing the charged plane into line segments along the y-axis shown schematically in Fig. 9 **(a)**. The overall electric field along the z-axis is,

$$E_z = \frac{\sigma}{\pi\varepsilon_0}\arctan\left(\frac{\frac{L}{W}}{2\left(\frac{z}{W}\right)\sqrt{4\left(\frac{z}{W}\right)^2 + \left(\frac{L}{W}\right)^2 + 1}}\right) = \frac{\sigma}{\pi\varepsilon_0}f(z) \tag{14}$$

Permittivity of free space is ε_o and z is the distance from the plane. (Derivation of the Eq. (14) can be found elsewhere [77]).

When two oppositely charged planes are positioned with a separation distance of z as in Fig. 9 **(b)**, the total electric field at any point at a distance x to a charge plane can be calculated as,

$$E = \frac{\sigma}{\pi\varepsilon_0}[f(x) - f(x+z)] \tag{15}$$

According to the electric field continuity, the change in the electric field entering a different medium is calculated as:

$$\varepsilon_1 E_1 = \varepsilon_2 E_2 \tag{16}$$

Eqs. (14)–(16) are the fundamental equations of the DDEF model for contact separation mode TENGs. When we have a TENG structure as provided in Fig. 9 **(c)**, electric potential at the interfaces between the conductive and triboelectric layers for electrodes 1 and 2, respectively are;

$$\phi_1 = \frac{-\sigma_U}{\pi\varepsilon_1}\left[\int_0^{x_1+x_2+z} f(x)dx\right] + \frac{\sigma_T}{\pi\varepsilon_1}\left[\int_{x_1}^{x_1+z} f(x)dx\right] \tag{17}$$

$$\phi_2 = \frac{\sigma_U}{\pi\varepsilon_2}\left[\int_0^{x_1+x_2+z} f(x)dx\right] - \frac{\sigma_T}{\pi\varepsilon_2}\left[\int_{x_2}^{x_2+z} f(x)dx\right] \tag{18}$$

Potential difference between electrode 1 and 2 at any separation distance (x) becomes.

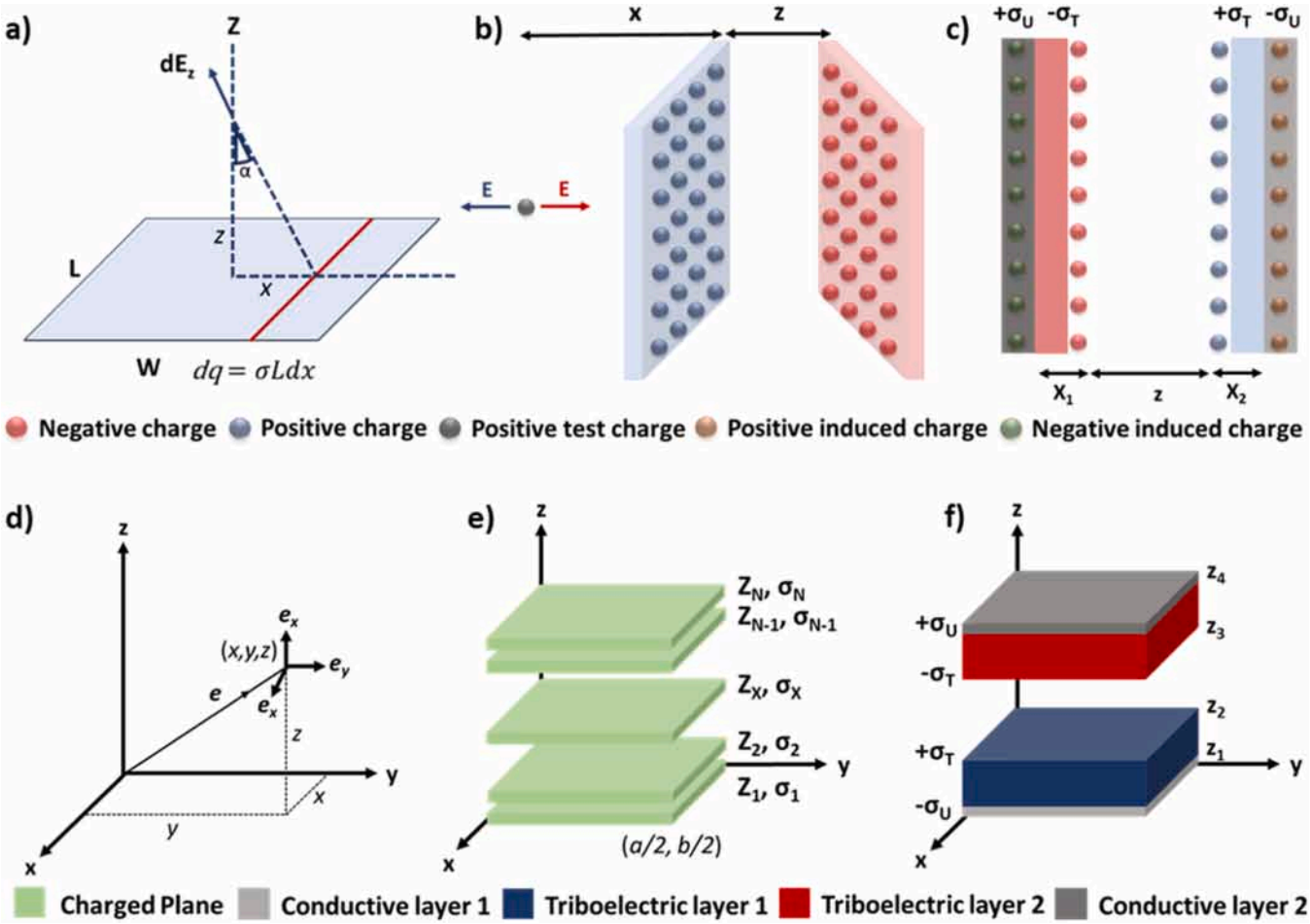

Fig. 9. Distance dependent electric field and 3D mathematical models of TENGs. (a) Uniformly charged plane having the length (L) and width (W) dimensions with charge density σ. (b) Electric field at an arbitrary point originating from two oppositely charged surfaces. (c) A schematic model and charge distribution of dielectric-dielectric TENG working in contact separation mode. Schematic illustration of (d) a Cartesian coordinate system, (e) N number of finite sized charged planes positioned at z_1, z_2,…. z_N, (f) TENGs structure working in vertical contact separation mode.
(a)–(c) are adapted with permission from Ref. [77]. Copyright 2017, Royal Society of Chemistry. (d)–(f) adapted with permission from Ref. [80]. Copyright 2020, Springer Nature.

$$V = \phi_1 - \phi_2 = \frac{-\sigma_U}{\pi}\left[\frac{1}{\varepsilon_1} + \frac{1}{\varepsilon_2}\right]\int_0^{x_1+x_2+z} f(x)dx + \frac{\sigma_T}{\pi\varepsilon_1}\left[\int_{x_1}^{x_1+z} f(x)dx\right] + \frac{\sigma_T}{\pi\varepsilon_2}\left[\int_{x_2}^{x_2+z} f(x)dx\right] \tag{19}$$

In open circuit condition σ_U is zero and V_{OC} is;

$$V_{OC} = \phi_1 - \phi_2 = \frac{\sigma_T}{\pi\varepsilon_1}\left[\int_{x_1}^{x_1+z} f(x)dx\right] + \frac{\sigma_T}{\pi\varepsilon_2}\left[\int_{x_2}^{x_2+z} f(x)dx\right] \tag{20}$$

In short circuit condition electrodes are at the same potential, thus;

$$V = \phi_1 - \phi_2 = 0 \tag{21}$$

$$\sigma_U = \frac{\sigma_T\left[\frac{1}{\varepsilon_1}\int_{x_1}^{x_1+z} f(x)dx + \frac{1}{\varepsilon_2}\int_{x_2}^{x_2+z} f(x)dx\right]}{\left(\frac{1}{\varepsilon_1}+\frac{1}{\varepsilon_2}\right)\int_0^{x_1+x_2+z} f(x)dx} \tag{22}$$

$$I_{SC} = A\frac{d\sigma_U}{dt} \tag{23}$$

2.3.2.2. 3D Mathematical (finite-sized charged plane (FSCP)) model.

DDEF was the first proposed model based on classical electromagnetic theory (based on Maxwell equations). However, the validity of this model was only proved when the movement of the TENG electrodes is in vertical direction. The horizontal movement of the TENG electrodes were not investigated by DDEF model yet. Shao et al. later proposed 3D mathematical model (based on classical electromagnetic theory) which overcomes the limitation of the previous model [79]. The 3D mathematical model is an overarching model that covers all operating modes of TENGs. Therefore, the DDEF model can be defined as a special case of the 3D mathematical model used when the movement of the electrodes is in the vertical direction. In this review, the fundamentals of the 3D mathematical model are covered in vertical contact separation mode to demonstrate the relationship between these two models. 3D mathematical model is based on the following expressions. The Maxwell-Poisson equation is.

$$\nabla . D = \rho(r) \tag{24}$$

where D is the electric displacement vector, ρ is the total charge density (composed of both contact and induced charge). When we have two different contact charged surfaces sandwiched between two electrodes having free charges, integral solution of this equation (please refer to [79,80] for the details of the solution) for the electrical potential at a point *(r)* in dielectric media α becomes,

$$\phi(r) = \frac{1}{4\pi\varepsilon_\alpha}\int \frac{\rho(r')}{|r-r'|}dV \tag{25}$$

In this equation r is the point where potential is calculated, $\rho(r')$ the charge density at point r' and ε_α is permittivity of the dielectric media α. A Cartesian coordinate system represented by the $\boldsymbol{e_x}$, $\boldsymbol{e_y}$ and $\boldsymbol{e_z}$ unit vectors is defined as shown in Fig. 8 **(d)**. A vector point (x, y, z) is the position vector. Consider N number of finite sized planes having the same dimensions a and b placed in x and y-directions, respectively, and positioned at z_1, z_2,…. z_N (provided in Fig. 8 **(e)**). The surface charge densities of the planes are σ_1, σ_2, …… σ_N, respectively. From Eq. (23), electrical potential at point $r\ (x, y, z)$ becomes.

$$\phi(x,\ y,\ z) = \sum_{i=1}^{N}\frac{\sigma_i}{4\pi\varepsilon(r)}\int_{-a/2}^{a/2}\times\int_{-b/2}^{b/2}\frac{dx'dy'}{\sqrt{(x-x')^2+(y-y')^2+(z-z')^2}} \tag{26}$$

$\varepsilon(r)$ is the permittivity of the dielectric media where electrical potential is calculated. This equation is used to calculate electrical potential in 3D mathematical model for any TENGs modes. When we have a TENG working in vertical contact separation mode as schematically illustrated in Fig. 8 **(f)**, electrical potentials at $z = z_4$ and $z = z_1$ are,

$$\phi(0,0,z_4) = -\frac{\sigma_u}{\pi\varepsilon_2}\left[\int_{z_4-z_1}^{\infty} f(z')dz'\right]+\frac{\sigma_u}{\pi\varepsilon_2}\left[\int_{0}^{\infty} f(z')dz'\right]+\frac{\sigma_T}{\pi\varepsilon_2}\left[\int_{z_4-z_2}^{\infty} f(z')dz'\right]-\frac{\sigma_T}{\pi\varepsilon_2}\left[\int_{z_4-z_3}^{\infty} f(z')dz'\right] \tag{27}$$

$$\phi(0,0,z_1) = -\frac{\sigma_u}{\pi\varepsilon_1}\left[\int_{0}^{\infty} f(z')dz'\right]+\frac{\sigma_u}{\pi\varepsilon_1}\left[\int_{z_1-z_4}^{\infty} f(z')dz'\right]+\frac{\sigma_T}{\pi\varepsilon_1}\left[\int_{z_1-z_2}^{\infty} f(z')dz'\right]-\frac{\sigma_T}{\pi\varepsilon_1}\left[\int_{z_1-z_3}^{\infty} f(z')dz'\right] \tag{28}$$

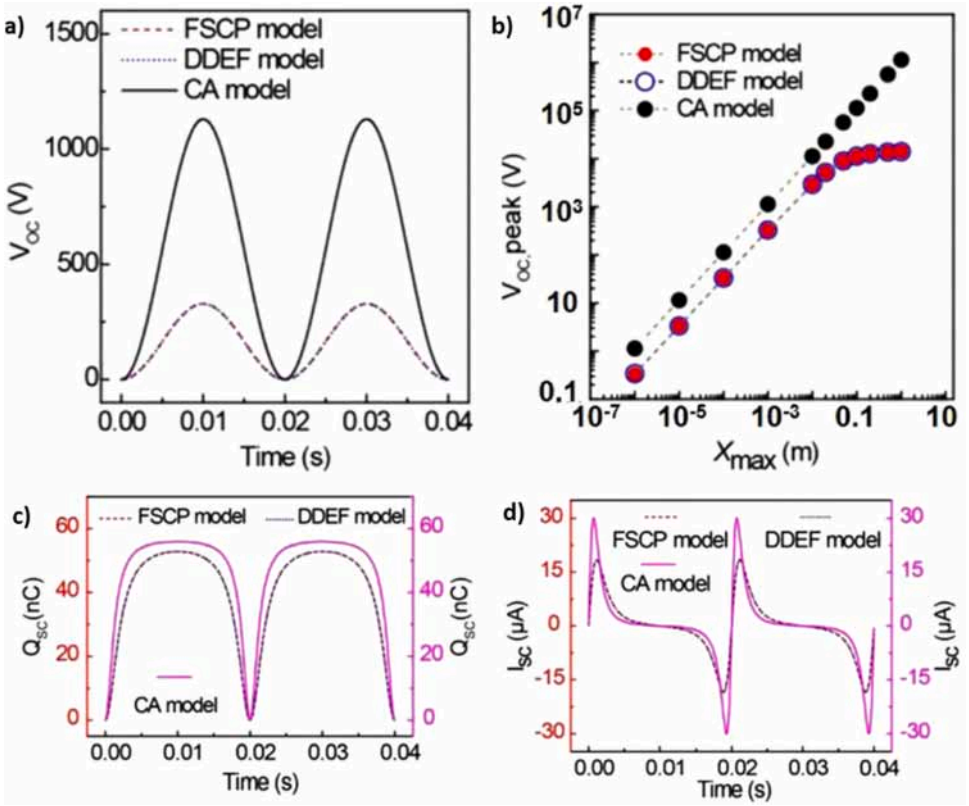

Fig. 10. Comparison of theoretical models for output performance of a dielectric-dielectric TENGs in contact-separation mode (a) Voc, (b) Voc at different separation contact materials, (c) Qsc and (d) Isc of a dielectric-dielectric TENG system working contact separation mode.
(a)–(d) Reproduce with permission from Ref. [79]. Copyright 2020, Elsevier.

Table 1
Comparison of frequently used theoretical models to predict TENGs outputs.

Model		Approach	Characteristics
Equivalent Circuit	Capacitive	Representing TENG device as serially connected ideal voltage source and inherent capacitance	Simple and effective for understanding of working principles TENGs. Overestimates voltage at large separation distances.
	Thevenin's and Norton's	Representing TENG device as time variant current source with internal impedance	Simple and effective for understanding of the working principles of TENGs. Give accurate simulation results.
Formal Physical	Distance Dependent Electrical Field	Calculating electric field at an arbitrary point perpendicular to charged surface.	Output performance of non-planar TENG geometries can be calculated precisely. Reported only for vertical movement direction.
	3D Mathematical	Calculate electric potential in a dielectric media at an arbitrary point using Maxwell-Poisson equation.	Provide time dependent 3D resolution. Valid for all operating modes.

where,

$$f(z') = \arctan\left(\frac{ab}{4z\sqrt{\left(\frac{a}{2}\right)^2+\left(\frac{b}{2}\right)^2+z^2}}\right) \tag{29}$$

In open circuit condition σ_U is zero and V_{OC} is;

$$V_{OC} = \phi(0,0,z_4) - \phi(0,0,z_1) = \frac{\sigma_T}{\pi\varepsilon_2}\left[\int_{z_4-z_2}^{z_4-z_3} f(z')dz'\right] + \frac{\sigma_T}{\pi\varepsilon_1}\left[\int_{z_1-z_3}^{z_1-z_2} f(z')dz'\right] \tag{30}$$

Eq. (30) is the same as Eq. (20) when a TENG system was constructed as Fig. 8(a). Unlike DDEF, the FSCP model is universal for the all-operating mode of TENGs and for both vertical and horizontal movement directions.

Comparisons of aforementioned models for performance outputs (*Voc*, *Qsc*, *Isc*) of vertical contact separation mode TENGs are provided in Fig. 10 **(a)–(d)**. It can be clearly seen that DDEF and FSCP models show the same output performances for *Voc*, *Qsc* and *Isc*. However, the capacitive model (CA) shows a significant deviation, especially at larger separation distances (Fig. 10 **(b)**). However, DDEF and FSCP models also deviate from the experimental results for output voltage of TENGs [77]. This deviation was attributed to the limited impedance of the measurement instruments that measure the output voltages. Therefore, Norton's model was proposed to overcome this issue as explained above [76].

Each of the theoretical models discussed in this review have unique approaches, advantages and disadvantages. Approach and characteristics of each model is provided in Table 1. In equivalent circuit models, TENGs are represented as circuit elements, whereas formal physical models focus on internal dynamics of TENG transducer. In formal physical models, electrical potentials are calculated at an arbitrary point with different approaches. In addition, one should note that equivalent circuit models and formal physical models can be linked with proper transport equations. (For details, please refer [72]). According to simulations reported in the literature, one can conclude that formal physical models have better success to predict TENG outputs compared to the capacitive model. The distortion of the electric field lines at the edge is neglected in the capacitive model. Moreover, parasitic capacitance which has an important effect on TENG output is also neglected in the capacitive model. More importantly, in the capacitive model, the TENG device is assumed to be infinitely large. In other words, the surface area of the electrode (*A*) is assumed to be infinitely larger than the total distance between the electrodes ($d_1 + d_2 + x(t)$). However, this assumption is wrong at large separation distances and overestimates the voltage. The use of 3D mathematical and DDEF (for vertical contact separation) models brought the simulation results very close to the experimental ones. Consistency of simulation and experiment is highly related to the reproducibility of experimental measurements. The reproducibility of TENG results depends on different parameters related to the experimental setup and environmental factors. Firstly, the contact charge is directly influenced by humidity and contact pressure, as discussed in the previous section. Secondly, the periodic motion of the contact and separation process is a key parameter in simulations. Therefore, controlling the movement frequency is crucial.

3. Strategies to enhance the efficiency of TENGs

The efficiency of any energy harvesting system is crucially important for its overall performance and viability. The definition of efficiency can be divided into two basic subheadings which are energy harvesting efficiency and energy transfer efficiency. The ratio of input mechanical energy and output electrical energy is defined as energy harvesting efficiency. Enhancing energy harvesting efficiency of a TENG system equals the work done by the TENG system. To increase work done by the TENG system, electrostatic force and/or displacement of the electrostatic charges need to be increased. Electrostatic force is increased by increasing surface charge density. Increasing displacement of these charges on the other hand depends on the device design. However, separation distance between two contact surfaces is generally limited due to design difficulties. Therefore, the main focus of improving energy harvesting efficiency in the literature is trying to increase surface charge densities. The following parts will cover the strategies to increase surface charge density upon contact. On the other hand, energy transfer efficiency is the ratio of the stored electrical energy to harvested electrical energy. The source of the energy harvested by TENGs almost never shows a constant characteristic. For example, biomechanical energy occurs when a living thing is in motion and varies depending on the speed, acceleration and frequency of movement. Moreover, although a few direct current (DC)-TENG structures were proposed in the literature, almost all TENG devices harvest mechanical energy and convert that to alternating current (AC). Inconsistent characteristics and AC nature of the harvested energy cannot be used directly for typical electronics since they require constant and stable DC supply. Therefore, harvested energy is first converted to DC and stored in a kind of energy storage device using proper circuit elements. The following parts of this review will cover approaches to enhance energy harvesting, transfer and storage efficiencies.

3.1. Strategies to enhance energy harvesting efficiency

3.1.1. Surface modifications of triboelectric layer

Surface modifications include physical modifications on the triboelectric layer such as adding roughness/nanoarchitecture or chemical modifications such as adding chemical groups or chemical grafting. Both methods, which alter the surface properties of the triboelectric layers, aim to increase the contact charge at the surface.

3.1.1.1. Physical modifications on triboelectric layer. Physical modification of the triboelectric layer is one of the most fundamental ways to improve contact charge. The main idea is to create a micro/nano-structured surface to enhance contact area, thereby increasing the effective surface area or introducing a controlled 3D texture to maximize

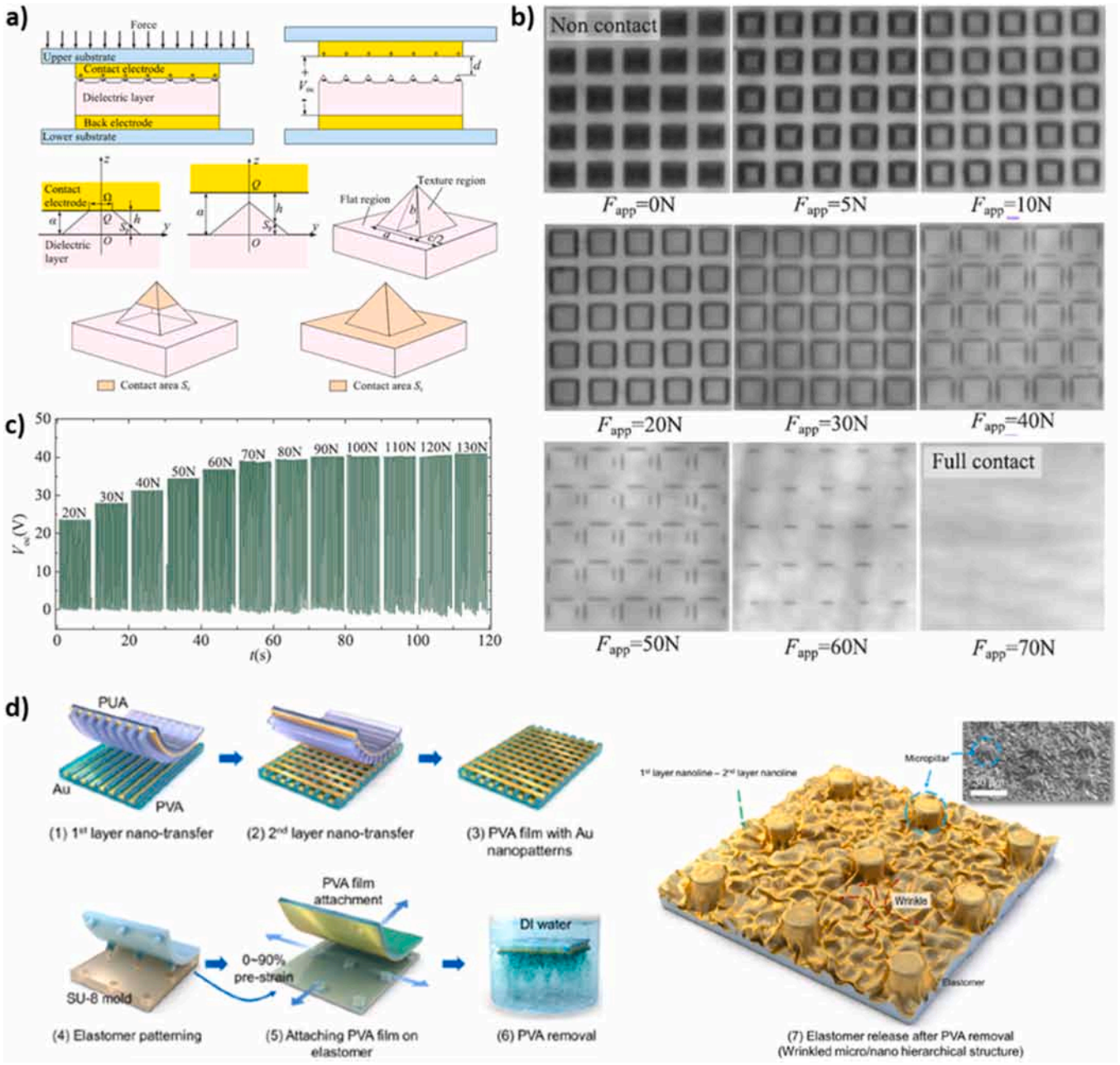

Fig. 11. TENGs with surface modifications for improved output performance. a) Schematic diagrams of pyramid texture in contact and separation state. b) Contact images of textured PDMS under different applied forces. c) Variations of open circuit voltage with different applied pressure. d) Schematics of the fabrication of wrinkled micro/nano hierarchical structure.
(a)–(c) Reproduce with permission from Ref. [87]. Copyright 2019, Elsevier. (d) Reproduce with permission from Ref. [97]. Copyright 2021, Elsevier.

charge generation during triboelectrification [6,81–83]. Tremendous efforts have been made since then to obtain a patterned triboelectric layer – mainly via templating, etching, inducing wrinkles or crumples and adding nanostructures onto triboelectric layers via coating.

Texturing, especially adding specific structures such as pyramid structure to the triboelectric layers are widely used to increase the triboelectrification [6,84–86]. Yang et al. recently attempted to explain this phenomenon through simulations, comparing the sizes of pyramid textures and their effect on triboelectrification [87]. Effective dimensions are presented in Fig. 11 **(a)**. PDMS patterns were fabricated with respect to these, and optical images were taken under different loadings to show the change in area (Fig. 11 **(b)**). They have found that especially under lighter loadings, there is a change in the open-circuit voltage due to changing contact area, while it becomes constant at higher loadings due to unchanged contact area (Fig. 11 **(c)**). However, they observed a decrease in the output performance of TENGs when the texturing is too dense and frequent, ultimately reducing the effective surface area. In the light of this, a simple texturing done by Tantraviwat et al. compared three different PDMS surface structures, which were highly porous, micropillars and flat surfaces [88]. A highly randomized and porous surface with random cavities, obtained through dry-etching techniques, has demonstrated higher Voc and Isc compared to micro-pillared and flat surfaces – indicating that incorporating randomized small cavities is more effective than a periodic structural arrangement. Nevertheless, researchers have also observed that micro-pillars yield better results than a simple flat PDMS surface, indicating that surface texturing remains a viable approach for enhancing TENG output performance.

Apart from increasing the contact area, surface roughness is also utilized in order to create a hydrophobic surface, eliminating the charge dissipation due to surface-adsorbed moisture [89,90]. Although some research presents conflicting views on the effect of moisture, several studies have shown that triboelectric performance improves with reduced moisture [91,92]. Jang et al. in 2016 have shown that with the introduction of dual-sized morphology based on microstructures and nanostructures, PDMS-based TENG delivers stable performance across a wide range of relative humidity (RH) [93]. Researchers observed that with the changing RH from 20 % to 80 %, a flat-surface PDMS lost an output voltage from 73 to 11 V. However, with the superhydrophobicity introduced by an embossed surface with dual-sized morphology, they achieved an output voltage of 174 V at 80 % RH, losing only 16 % from the initial output voltage measured at 20 % RH. A similar strategy is conducted by Zhou et al. in 2019 by fabricating a 3D, hierarchical, and porous pattern for improved triboelectric performance with high humidity resistance [94]. With the 3D PDMS structure, they have improved the output voltage and current density from approximately 100 V and 5 μA cm^{-2} to 400 V and 17 μA cm^{-2}, respectively. The overall performance improvement is again attributed to the contact area due to 3D hierarchical structure compared to the flat surface. Moreover, it is found that the capacitance of the 3D structure is higher than that of the flat surface, which was correlated with an increased charge density. More importantly, this 3D PDMS layer with a surface contact angle (SCA) of 161° can retain 86 % of its initial open-circuit voltage from 20 % RH to 80 %RH. In the case of the flat PDMS surface, only 19 % of the initial output voltage is retained when the RH increase from 20 % to 80 %. Overall, texturing the triboelectric layer's surface to achieve superhydrophobicity enhances triboelectric output by increasing the contact area and ensures humidity-resistance in TENGs.

Polarization differences due to the introduction of roughness are shown to play a crucial role in the output performance of TENGs. Verners et al. in 2022 have shown that introducing roughness to polymer surfaces can shift their polarity toward positive, whereas polymers with smooth surfaces tend to charge negatively [95]. The research is conducted with 6 different polymers, namely polyamide 6,6 (PA 66), ethylene-octene copolymer (EOC), polyvinyl acetate (PVAc), polystyrene (PS), polyvinylidene fluoride (PVDF), and PDMS. Each polymer was prepared with a smooth surface using spin-coating, while rough surfaces were created through methods like non-solvent treatment or sugar-templating. When identical polymers with smooth and rough surfaces are electrified in contact-separation mode, the smooth surfaces become negatively charged, while the rough surfaces become positively charged. This phenomenon is observed for all 6 of the aforementioned polymers and further proven by kelvin probe force microscopy (KPFM). For the case of PDMS, the initial scan shown an average surface potential of 208 mV and 888 mV for the smooth and rough surfaces, respectively. After the contact-separation, the average potentials are changed to −638 mV and 8026 mV for the smooth and rough surfaces, respectively. To further explore this, researchers conducted computational studies by the means of Finite Element Method (FEM) and Reactive Molecular Dynamics (RMD). FEM analysis shows that smooth surfaces experience higher tensile strain compared to rough surfaces. RMD is used to understand this strain effect on bond scission, which is the primary reason for contact electrification by material transfer in the case of non-ionic polymers, where a more extensive bond scission is found on smooth surfaces [26,60,62]. Further analysis is done on PDMS, PS, and EOC based on their energetically favorable terminations. For the case of PDMS, from the terminals of O and Si, it is observed that the negatively charged fragments have lower potential energies compared to the positively charged counterparts. Simply, negatively charged fragments are found to have smaller scission energies compared to the positively charged ones. This suggests that after bond cleavage, the generated fragments, which move freely, tend to carry a negative charge. Coupled with the knowledge of a higher strain effect on smooth surface, it suggests that the rough surface should be charged negatively, which is the opposite of what is found experimentally. This is further explained by the presence of the physisorption, noting the negatively charged fragments are more likely to accumulate on smooth surfaces rather than the rough ones. Ultimately, while the mechanism depends on the choice of material, experimental and computational studies consistently show that smooth polymer surfaces charge negatively, while rough surfaces charge positively.

It is also possible to improve triboelectrification by simply adding nanomaterials onto the triboelectric surface. Bhavya et al. simply used liquid-phase exfoliated 2D hexagonal boron nitride nanosheets (BNNS) to modify the triboelectric layer [96]. Spin coating method is used to deposit BNNS onto biaxially-oriented polyethylene terephthalate (BoPET). BNNS doposition on BoPET improved the triboelectrification at least 70 times. This shows a feasible and cost-effective way to improve triboelectrification by simply depositing nanomaterials onto the triboelectric layer. Ahn et al. introduced wrinkled structures coexisting with micropillars to enhanceTENG performance by combining regularly arranged microstructures with randomly distributed nano-texturing [97]. To obtain this structure, common surface texturing methods such as nanotransfer, molding, and buckling are combined. The fabrication route of this structure is schematically shown in Fig. 11 **(d).** A typical SU-8 resist is used for the molding yet treated with photolithography to obtain a microstructure for the elastomeric substrate. In the side, nanopatterned polyvinyl alcohol (PVA) is prepared via krypton fluoride (KrF) lithography of a silicon (Si) master, where polyurethane resin is used to obtain the nanopatterned mold. Subsequent gold (Au) deposition using an e-beam evaporator and transfer onto PVA films are practiced to have a nanopatterned surface on PVA films. The elastomer used for micropatterns, on the other hand, treated with (3-Aminopropyl)triethoxysilane (APTES) and coated with UV curable adhesive to transfer nanostructures on PVA to the previous structure. After PVA is dissolved in water, authors obtained morphology-controllable wrinkled micro/-nano hierarchical structure (WHS) on a single substrate, which is normally very challenging to obtain. Nanostructures on wrinkled surfaces impart superhydrophobicity, which is essential for TENG devices, as triboelectrification is highly influenced by moisture. All in all, with the WHS structure, the output performance of TENGs is increased by 608 % when compared to a simple flat surface. The effect on the pre-stretching and dimensions of the nanopattern in terms of output voltage, showing the micro/nano pattern and its effect on the output performance is controllable. This highlights the significant impact of surface morphology and modifications on the output performance of TENGs.

3.1.1.2. Chemical modification of the surface of triboelectric layer. Apart from physical modifications to the triboelectric layer, chemical modifications applied directly to the surface can also enhance performance [98–101]. Although this approach shows promise, particularly to increase the contact charge, recent research on the topic remains limited. Byun et al. in 2016 explored the concept of chemical functionalization of the surface of the triboelectric layer by thoroughly controlling the surface dipoles and surface electronic states [102]. To realize that they have used electron-donating and -withdrawing functional groups, which are self-assembled as monolayers (SAM) on silica (SiO_2) surfaces (Fig. 12 **(a)**). The surface potentials measured by KPFM (Fig. 12 **(b)**) reveals that surface charges upon contact electrification can be controlled by changing the type of SAM on SiO_2 layer. SAM modification of substrates other than SiO_2, such as alumina (Al_2O_3) and indium tin oxide (ITO) has also been shown to significantly alter surface potentials. Amino (NH_2) groups tend to behave as an electron-donating layer, resulting in a more positive triboelectricity. On the other hand, CF_3 behave as electron-withdrawing layer, resulting in a more negative triboelectricity [102]. With this knowledge, researchers modified various surfaces, and used it even in textile-based TENGs. As an example, Sun et al. in 2022 modified silk-based fabrics with different functional groups, organo-siloxanes such as n-Butyltrimethoxysilane (BTMS),

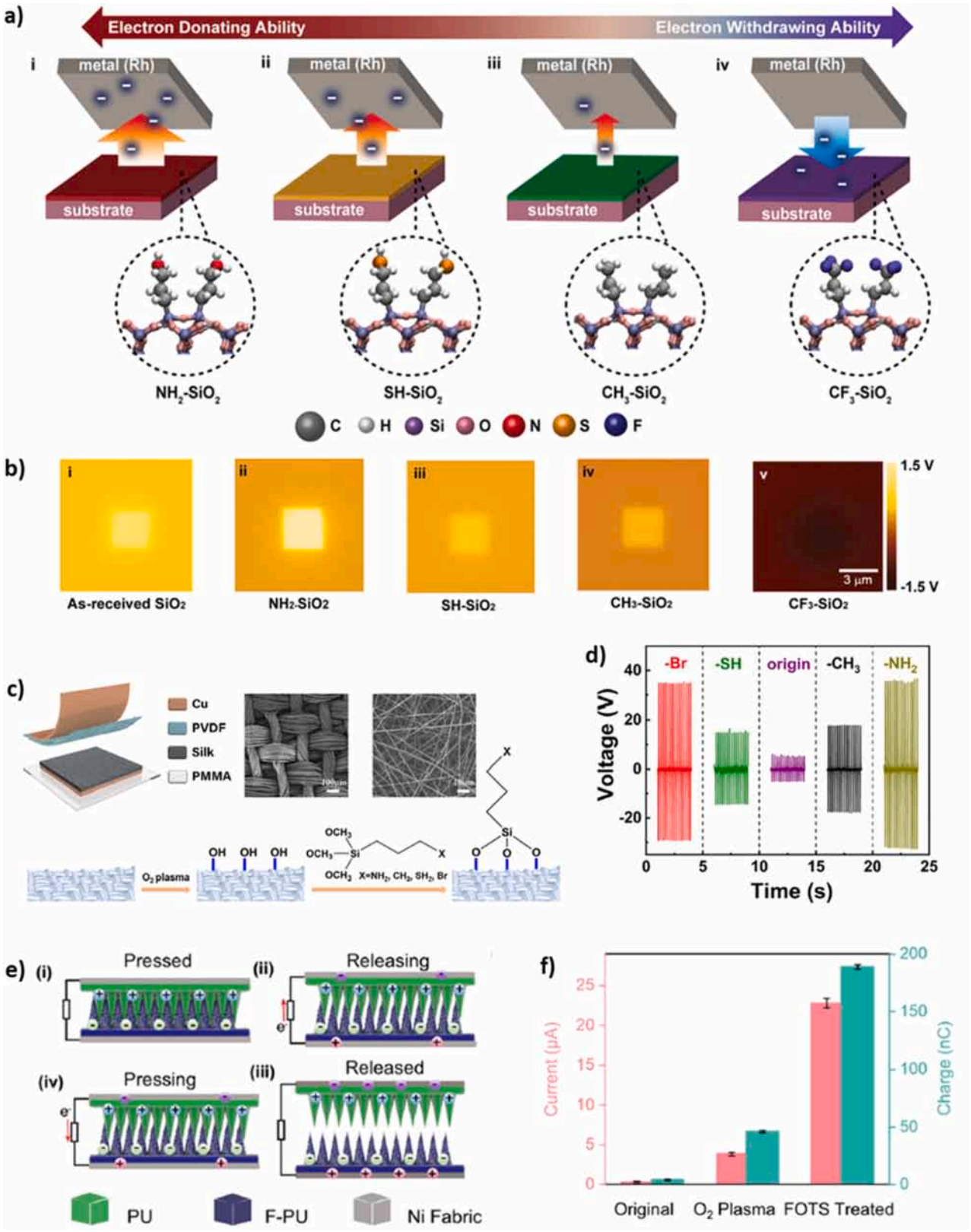

Fig. 12. Examples of the chemical modifications on the surface of triboelectric layers. a) Schematic of controlling surface dipoles via SAM and their tribo-electrification with electron-donating and withdrawing groups. b) Surface potentials of substrates after SAM coatings on SiO_2 surfaces. c) Schematic representation of the TENG device with functional-group-modified fabric, and the schematic representation of the modification process and the SEM images of modified silk and PVDF nanofibers. d) Output voltage of TENG devices with PVDF and modified silk triboelectric pair with different modification groups. e) Schematic representation of the mechanism of triboelectrification of fluorinated PU microcones and with nonfluorinated one. f) Graph shows current density and charge density difference of O_2 plasma treated and FOTS treated microns.

(a) and (b) Reproduce with permission from Ref. [102]. (c) and (d) Reproduce with permission from Ref. [103] Copyright 2022, Royal Society of Chemistry. Copyright 2016, American Chemistry Society. (e) and (f) Reproduce with permission from Ref. [104] Copyright 2022, Elsevier.

(3-aminopropyl) trimethoxysilane (APTMS), (3-bromopropyl) trimethoxysilane (BPTS), and (3-mercaptopropyl) trimethoyxsilane (MPTMS) [103]. Fabrics are treated with oxygen plasma to graft hydroxyl groups, then immersed into organo-siloxane containing ethanol solution for 12 h. Schematic representation of the final TENG structure and the grafting procedure is given in Fig. 12 **(c)**. Here, researchers again observed that the electronegativity variation of the whole TENG device can be regulated by the functional groups that are grafted onto silk

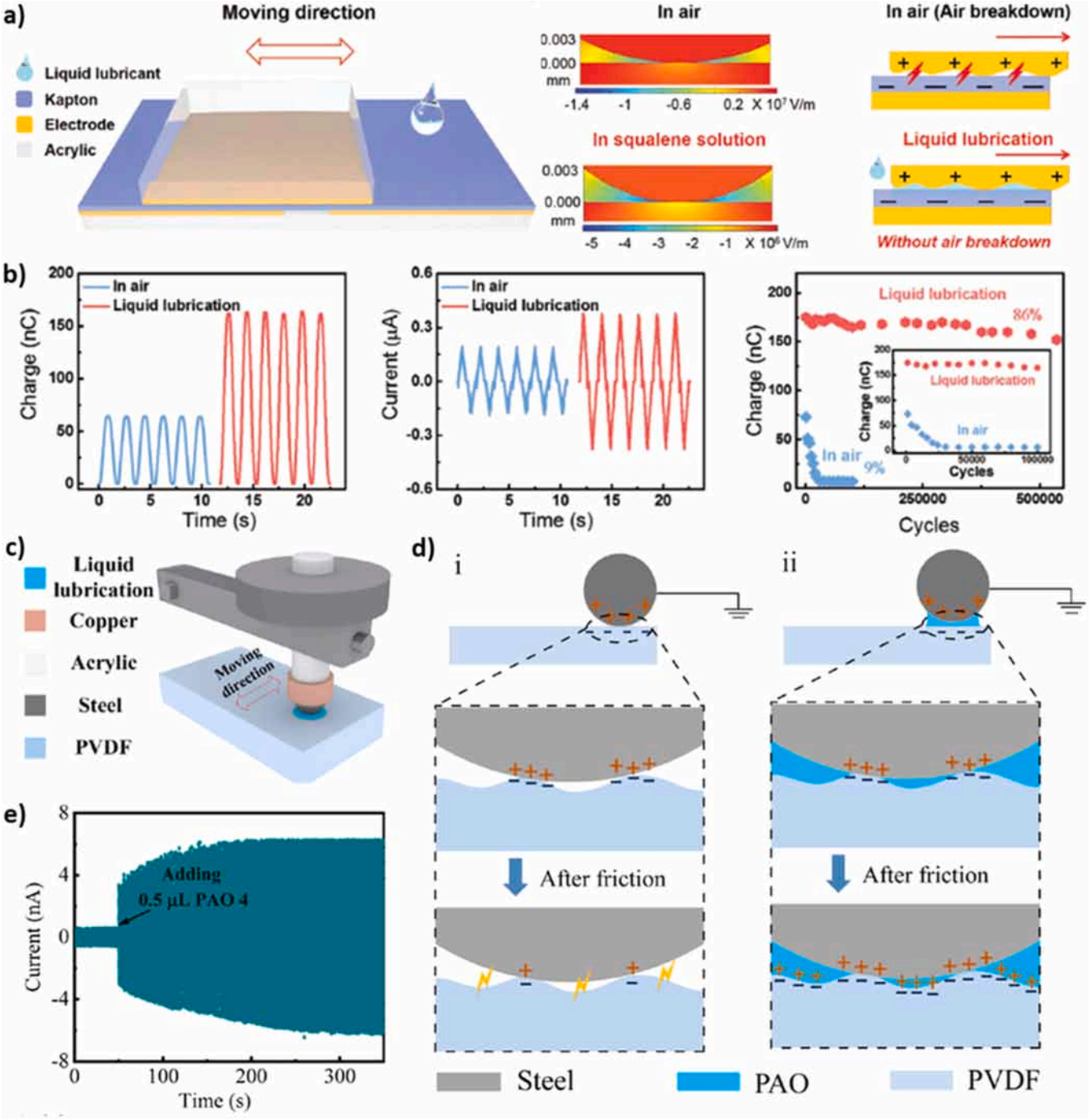

Fig. 13. Lubrication for improved TENG performance. a) Schematic representation of a sliding mode TENG with added lubrication with corresponding charge generation under different pressures. Images show breakdown between two electrodes with and without squalane solution with corresponding finite-element simulations and suggested mechanisms for improving the practicality of TENGs. b) Output metrics of the slide-mode TENG with and without lubrication. c) Schematic representation of friction testing machine using steel ball as a friction pair with PVDF. The suggested mechanism is also shared with air and PAO 4 lubrication. d) Mechanism of the friction pairs with and without lubrication is given. e) Comparison of triboelectric output of steel ball – PVDF friction pair before and after adding lubrication, and proposed mechanism for the improvement in TENG performance.
(a) and (b) Reproduce with permission from Ref. [113]. Copyright 2020, Wiley-VCH. (c)–(e) Reproduce with permission from Ref. [114]. Copyright 2012, Elsevier.

fabrics. This chemical grafting also changed the hydrophilicity of the fabric surfaces. In a simple combination of original silk/modified silk pair, the output voltage and the short-circuit current can be regulated from 5.38 V to 36.6 V (Fig. 12 **(d)**) and from 0.12 μA to 0.52 μA, respectively. This not only demonstrates that chemical functionalization of the surface can significantly improve output performance but also shows that surfaces can be tailored for a specific end-use [103].

Both physical and chemical modifications of the triboelectric layer can be utilized to improve the performance in a great manner. Feng et al., in 2022, used this idea to amplify the TENG performance compared to flat and un-modified surfaces [104]. They have used direct image lithography (DIL) method to fabricate PU layers with surface microcones, then chemically functionalized them with trichloro (1H, 1H, 2H, 2H-perfluorooctyl) silane (FOTS) vapor to obtain increased roughness with surface fluorine groups. TENG device is formed with microcones treated with FOTS and untreated one, which is schematically shown in Fig. 12 **(e)**. Having microcone structures resulted in a much higher current and charge output compared to the flat surfaces. Moreover, with respect to the original cone structure, PU treated with FOTS yielded much higher current and charge output (Fig. 12 **(f)**) – showing the promise of chemical functionalization combined with traditional physical modifications [104].

Ion implantation is another interesting technique used to improve the triboelectrification on the surface [105–107]. This technique puts an advance over the simple chemical grafting methods as the distribution of implanted ions in a varied thickness can be controlled precisely. In order to explore such a concept, Fan et al. used ion implantation to create polar bonds and found that they significantly improve the polarization [108]. N ions are chosen to be implanted into PTFE and FEP as it provides the highest electronegativity. With the ion implantation technique, they have observed a strong polar bonding formation (i.e. $C \equiv N$ or $C = N$ bonds). The best-performing ion-implanted PTFE and FEP exhibit a 7.8-fold and 4.6-fold increase in charge density, respectively, compared to their original structures. Additionally, ion implantation has transformed PTFE into a polar polymer with an increased dielectric constant. These changes are correlated with higher surface charge accumulation, which significantly impacts the output performance of the triboelectric layer [108]. Another study utilized recycled PS with smooth and rough surfaces to obtain a single-material TENG, where additional chemical modification with SAM is conducted to improve the overall charge density [109]. As discussed in the previous section; by obtaining rough and smooth-surfaced PS films, researchers were able to fabricate a single-material TENG, where the smooth one is charged negatively and rough surface positively. Vinyltrimethoxysilane (VTMS) modified smooth PS (most negatively charged) and APTES modified rough PS (most positively charged) films are then chosen to form the TENG. With the matching combination of surface morphology and the SAM modification, researchers were able to improve the overall charge density from 0.03 to 1.52 nC cm^{-2}.

3.1.1.3. Lubrication of triboelectric layer. One of the biggest unsolved issues of TENGs is the wear of triboelectric surfaces. Due to the triboelectrification mechanism, especially at solid-solid interfaces, being mechanically driven—through tapping, sliding, bending, etc.—physical degradation of triboelectric surfaces is a major issue that hinders the practical application of TENGs [110]. Lubrication, which is actually a very-well known solution to prevent wear in friction surfaces, is promising in this regard. As a fairly new introduction to TENGs, lubrication of triboelectric layers both reduce the wear, which extends the lifetime of TENGs, and increase the output performance [110–112].

Zhou et al. proposed a sliding-mode TENG with liquid lubrication at the interface to enhance stability and improve performance output (Fig. 13 **(a)**) [113]. By introducing squalane between the triboelectric layers, the air breakdown on the interface of triboelectric layers is suppressed. It is found that the liquid lubricant replacing the air and suppresses dielectric breakdown – which drastically reduces electrostatic charge loss. Due to this mechanism, output performance of the sliding mode TENG is highly increased (Fig. 13 **(b)**). Moreover, it increases the contact efficiency which is observed via an increase in capacitance of the TENG, which is another reason for the increased output performance. Simply, liquid lubrication is said to improve electric output by suppressing interfacial breakdown and also increases the lifetime of the TENG greatly [113]. In another case, Liu et al. formed different friction pairs with a steel ball, which are PVDF, polyoxymethylene (POM) and PTFE, and added PAO 4 lubricant to see the effect of lubrication on triboelectric performance [114]. Schematic representation of a friction testing machine using a steel ball as a friction pair with PVDF is provided in Fig. 13 **(c)**. Device schematic and suggested mechanism is provided in Fig. 13 **(d)**. By simply adding lubrication, they have seen an increase in triboelectric generation with a simple steel/-triboelectric layer interface. Authors clearly demonstrated the advantage of PAO 4 lubricant with the real-time data gathered by adding the lubricant in mid-experiment, which is given in Fig. 13 **(e)**. Lubricants with only carbon and hydrogen alkanes and alkenes such as PAO and squalene are observed to increase the triboelectric signal, and again it is stated that the improvement is due to improved breakdown field and suppression of the loss of triboelectric charges [114]. Both researches in recent years showed that lubrication not only improves the output performance of TENGs, but also improves their stability.

3.1.2. Modification of the chemical structure of triboelectric layers

Apart from the chemical modifications that are done as a post-process to functionalize, graft or implant ions onto the surface of the triboelectric layer, one can also start from scratch and modify chemical structure of the triboelectric layer. As the choice of material selection is crucial for TENGs for high performance output, it is also tailorable by the processing techniques [115]. As such, what is proposed for the modification of the chemical structure is to modify the widely known polymer materials such as PTFE, FEP, PVDF, nylon, PVA or cellulose to obtain better mechanical properties or lower impedance/higher electrical conductivities, and even change their polarity in terms of triboelectrification [116]. In this manner, the most common technique is to introduce ionic groups to the polymeric triboelectric layers or to increase the inherent conductivity of the polymers with doping [98,117].

3.1.2.1. Addition of ionic species. The main idea of introducing ionic groups (cations, anions or ionic liquids) is to induce Hofmeister effect and synergistically increase the electrostatic interaction at the same time. Mainly, specific ion effects (shortly SIE) are much more important than the number of ionic charges or concentrations as suggested by Debye-Hückel theory [118]. This Hofmeister effect, coupled with the electrostatic induction caused by the ionic species, is a very widely applied route to improve TENG performance. In a very simple manner, Ryu et al. explored the addition of ionic species to PVA to change its triboelectric properties, which is confirmed with KPFM and enhanced output (Fig. 14 **(a) and (b)**) [119]. With the addition of calcium chloride ($CaCl_2$) and phosphoric acid (H_3PO_4), they have been able to obtain the most positive and most negative triboelectric materials, respectively (Fig. 14 **(c)**). The output performance increase in these were attributed to asymmetric ion pairing [119]. To build on that, Cheong et al. introduced different ionic species to see both anion and cation effect [120]. They have explored the molarity, the effect of cation species while the anion is fixed, and vice versa to find the best performing combination. Interestingly, the best performing ones, which are PVA-$CaCl_2$ and PVA-$NaNO_3$, have the highest dielectric constant and dielectric losses, which they attributed to the increase in ionic polarization due to migration of ionic species. Moreover, they systematically explored the triboelectric performance metrics with fixed electrolyte concentration, fixed anion concentration, and fixed cation concentration. Although significant achievements have been made by simply adding ionic species

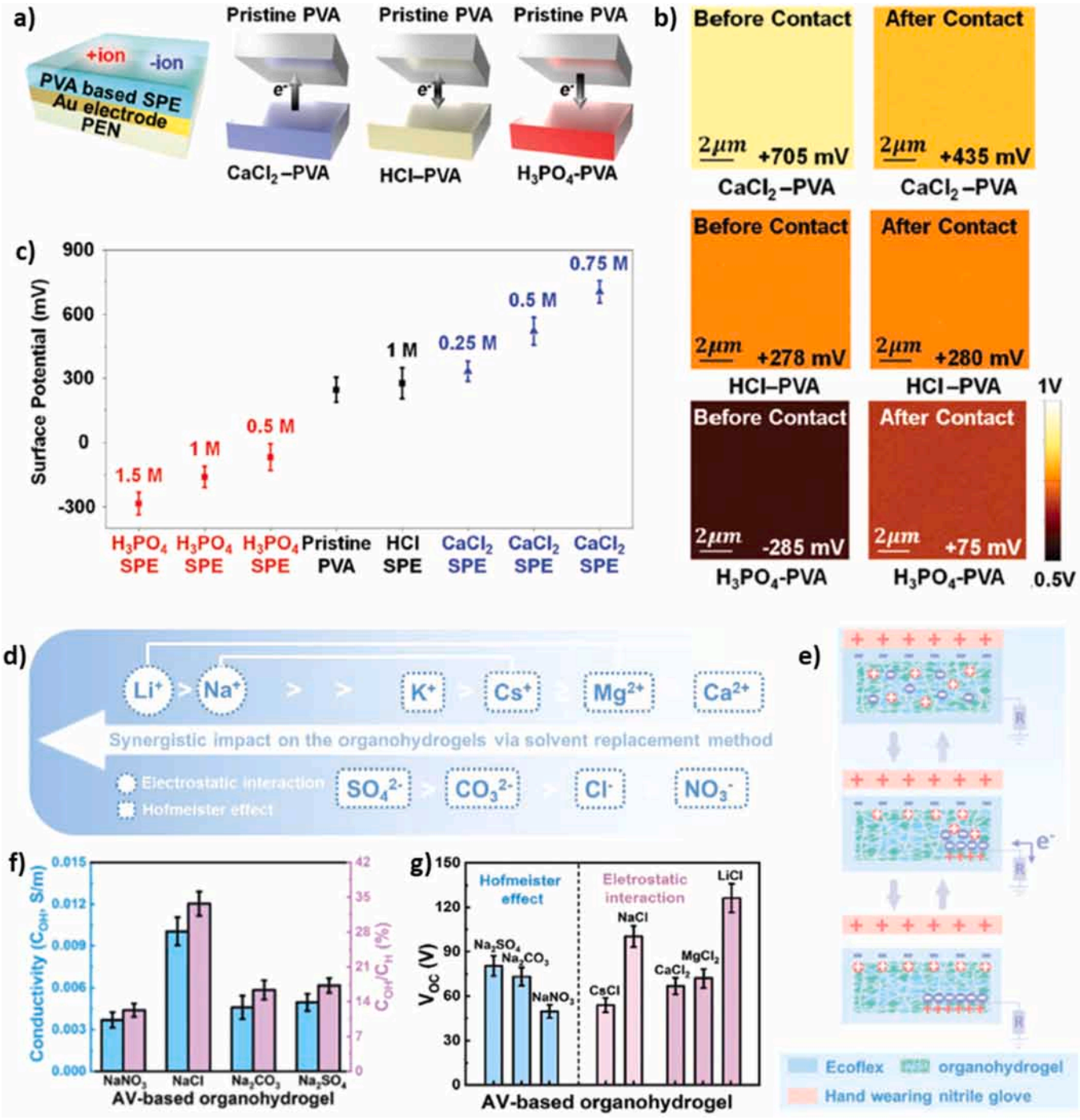

Fig. 14. Modification of the chemical structure of triboelectric layers. a) Schematic representation of ionically modified PVA triboelectric layers assembled as TENGs b) Corresponding surface potentials of modified layers. c) Surface potential graph of PVA layers with different ionic additions. d) Schematic representation of Hofmeister effect on the conductivity of organohydrogels based on polyacrylamide/PVA. e) Schematic illustration of the working principle of organoyhydrogels covered with Ecoflex. Comparisons of f) conductivity, g) Hofmeister effect, and electrostatic interaction with various ionic additions.
(a)–(c) Reproduce with permission from Ref. [119]. Copyright 2017, Wiley-VCH. (d)–(g) Reproduce with permission from Ref. [121]. Copyright 2021, Wiley-VCH.

to the PVA matrix, no relation was made with the Hofmeister effect. Wu et al. explored this effect to understand the mechanism behind the ionic additions on triboelectrification. Polyacrylamide/PVA organohydrogels were prepared with the Na^+ based salts using a glycerol immersion process [121]. Schematic summary of the findings on the synergistic effects on the conductivity of Polyacrylamide/PVA organohydrogels is given in Fig. 14 **(d)–(g)**. It is seen that the Hofmeister effect influences ionic conductivity, and although the cations are generally disregarded in Hofmeister in terms of conductivity, anions such as lithium and sodium are very important due to their electrostatic interactions. They have seen the "salting-out" phenomenon positively affect the output performance of the organohydrogels (Fig. 14 **(d)**), which is due to the formation of lithium or sodium bonds by electrostatic interactions and provides stable charge channels and higher conductivity than other pairs. When covered with Ecoflex, the organohydrogels can be utilized as single-electrode triboelectric nanogenerators (Fig. 14 **(e)**). Ultimately, in Fig. 14 **(f)** and **(g)**, it is observed that the electrostatic interaction plays a much significant role in output performance, as LiCl or NaCl

performs much better than the Na_2SO_4 or $NaNO_3$ [121].

Based on the studies explored, providing a definitive explanation for the improved triboelectrification caused by the addition of ionic species is difficult. The best explanation is the Ion Transfer Model (Section 2.1.2), where the ions migrate from one surface to another, leading to enhanced triboelectrification with the presence of ionic species. In addition to migration, improved ionic conductivity with enhanced EDLC is also proposed as a means to enhance triboelectric performance [122, 123]. Herein, capacitive induction occurs due to the polarization originating from triboelectricity [123]. Moreover, a recent study has shown that anions have more impact than the cations for PVA-based hydrogels [124]. It is also known that adding ionic species significantly affects the mechanical properties, which can indeed affect both mass transfer and ion transfer models [125]. Studies must continue to investigate the origin of enhanced triboelectrification caused by ionic species, yet providing a comprehensive answer remains challenging.

3.1.2.2. Other structural modifications. Various bottom-up modifications, aside from ionic integration, are also applied to polymeric triboelectric layers, aiming not only to enhance performance but also to maintain transparency. Park et al. used adipate-based plasticizer on

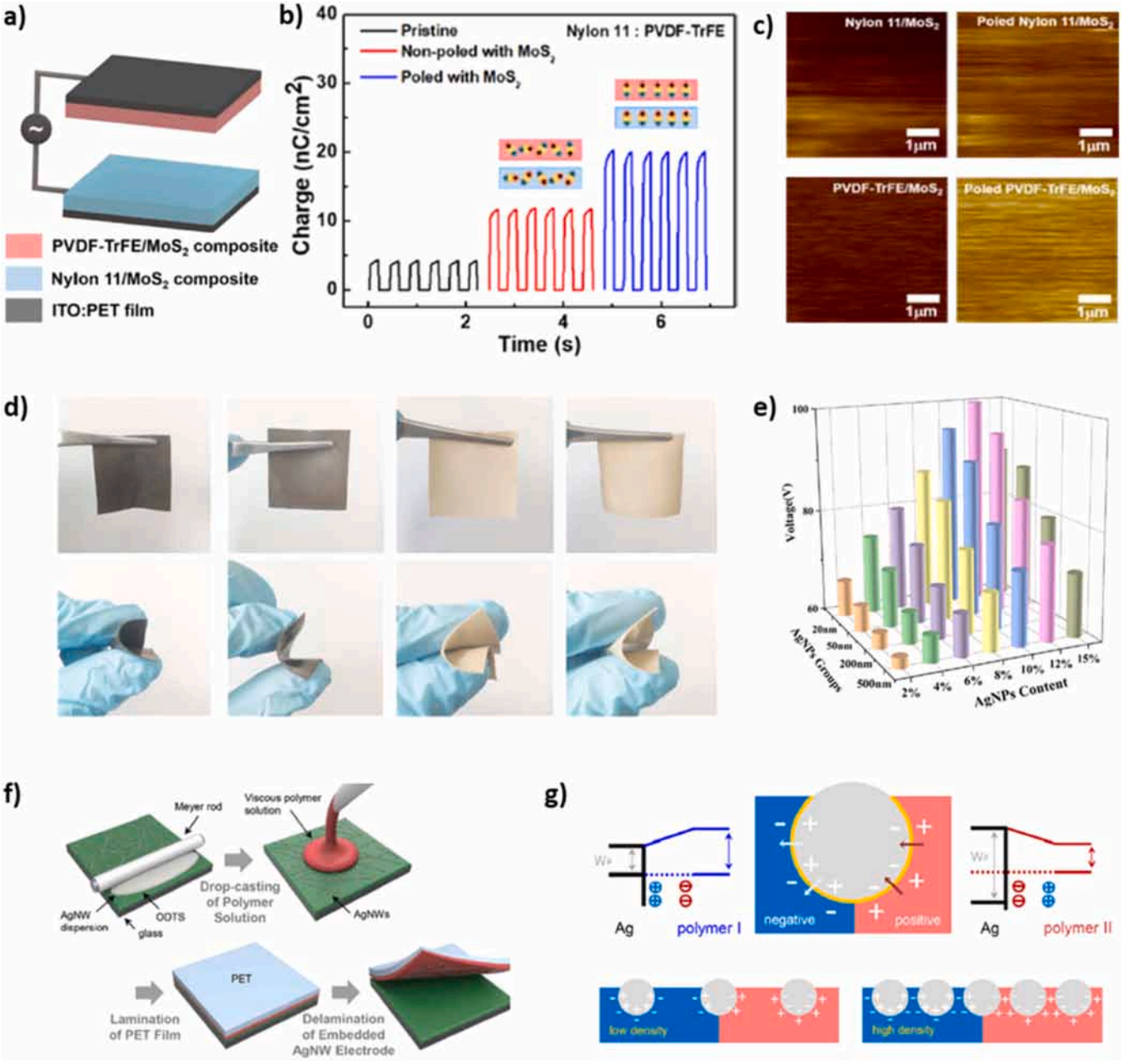

Fig. 15. Examples of composite structures for TENGs. a) MoS_2 as a microadditive for PVDF-TrFE and Nylon 11, which is paired for TENG. b) Output charge densities and c) respective KPFM images of PVDF-Nylon11, PVDF/MoS_2-Nylon 11/MoS_2 (Non-poled), PVDF/MoS_2-Nylon 11/MoS_2 (poled) TENG pairs, where poled composites have increased charge generation due to modified surface polarization. d) Introduction of Ag NPs with different sizes into silica gel and their effect on the triboelectric performance. (e) Voltage outputs depending on the size and content of Ag NPs. f) Schematic representation of the fabrication steps of Ag NW embedded polymer TENG dielectric layers. g) Schematic representation of charge transfer between PVC and PMMA facilitated by the Ag NWs, where blue region is tribonegative and red region is tribopositive.
(a)–(c) Reproduce with permission from Ref. [137]. Copyright 2019, American Chemical Society. (d) and (e) Reproduce with permission from Ref. [154]. Copyright 2022, IOP Science. (f) and (g) Reproduce with permission from Ref. [158]. Copyright 2019, Elsevier.

polyvinyl chloride (PVC) to obtain transparent and stretchable TENGs. As the plasticizer is added, both transparency and dielectric constant are heightened as well as the tribonegativity of the PVC [126]. They obtained nearly a 20-fold increase in output performance compared to the native PVC [126]. In a similar manner, Wu et al. controlled the cross-linking density and ionic conductivity to find an optimum point for the highest TENG performance [127]. They have used 1-butyl-3-metyhyimidazoium hexafluorophosphate ([BMIM]PF_6) as the ionic liquid and polyethylene glycol dimethacrylate (PEGDMA) as the monomer for polymerization to obtain polyethylene glycol (PEG) with different molecular weights. They have seen that increase in molecular weights after some point decreased the conductivity, while the increase in the ratio of ionic liquid increased both the ionic conductivity and transmittance [127]. Both works indicate that controlling the structure of the polymers enables transparent and possibly stretchable triboelectric layers with improved triboelectrification.

Bottom-up fabrications combined with top-down processes to modify the triboelectric layer are named as nanoarchitectronics [128]. In addition to offering the advantages of rapid production and application to large areas, it is also possible to produce nanoporous structures quickly and in a single step. Park et al. demonstrated this one-step fabrication via ternary polymer solution blend with supramolecular assembly [129]. Sulfonic-acid-terminated poly(styrene) (SPS), poly (2-vinylpyridine) (P2VP), and amine terminated poly(ethylene oxide) (APEO) are used to obtain the triboelectric layer. Competition between APEO-SPS and P2VP-SPS interaction causes the formation of spontaneous nanopores with a diameter average of 33 nm, which leads to formation of surface-conformal triboelectric nanoporous films with power density of almost 2 times higher than that of planar surfaces [129].

3.1.3. Composite triboelectric layers

Another common way to improve the overall TENG performance is the fabrication of composite structures. The incorporation of materials ranging from micron to nano sizes, and from inorganic to polymeric materials, has shown to be an effective way to improve output performance [116,130,131]. Ulterior motive of the fabrication of composite structures are modulation of the dielectric constant, providing new charge generating surfaces, improving the conductivity/lowering the impedance of the dielectric layer or even improving the mechanical or frictional properties of the dielectric layer, such as hardness, elastic modulus, and wear resistance [131,132]. Moreover, the composite structure can be a hierarchical assembly or simply an addition of another layer for the purpose of improved charge generation or charge trapping [133–135]. Herein, the focus is placed not on the type of materials, but on the composite structure and its ultimate purpose.

3.1.3.1. Microadditives. As mentioned before, one of the simplest ways to improve the overall performance is the incorporation of nanomaterials into the dielectric matrix. Mostly, the aim is to modify the dielectric constant, with the side benefits of increasing surface-charge density and reduction of the triboelectric loss [136]. Yet, incorporation of micron-sized particles has also shown great improvement on the output performance of TENGs. Kim et al. used bulk molybdenum sulfide (MoS_2) to form composites with triboelectrically positive ferroelectric Nylon-11 and triboelectrically negative ferroelectric PVDF-TrFE (Fig. 15 **(a)**) [137]. By dipolar polarization, and adding MoS_2 structures, they have obtained 500 % increase in current density and 220 % increase in output voltage, which is attributed to the change in surface polarization as analysed by KPFM (Fig. 15 **(b) and (c)**) [137]. Similarly, Kim et al. used high permittivity $CaCu_3Ti_4O_{12}$ dielectric particles and formed a composite with butylated melamine formaldehyde (BMF) [138]. Compared with the typical aluminum oxide (Al_2O_3) and TiO_2, they have seen that high permittivity $CaCu_3Ti_4O_{12}$ material also enhances triboelectric output voltage and current density. Compared with the pure BMF, even 1 wt% addition of $CaCu_3Ti_4O_{12}$ increased both the voltage and current output at least two times [138].

3.1.3.2. Nanoadditives. Nanomaterials are used commonly to obtain highly performing triboelectric layers for TENGs. The effect of nanomaterials can vary depending on their material properties. The main focus is to improve the dielectric constant to improve the electrostatic induction, change or improve the charge affinity, and increase the surface charge density with the possible side benefits of increasing mechanical stability or resistance to wear [132]. To achieve all of these, various nanostructures such as nanoparticles, nanowires, and nanosheets are employed to fabricate nanocomposite structures [139–146].

As an example, for nanoparticle additives, barium titanate ($BaTiO_3$) is one of the most common materials that is used to form composites for TENGs [147–149]. Its inherent piezoelectric properties have shown to enhance triboelectric performance, especially when the piezoelectric polarization is aligned with the triboelectric charges [150]. For instance, Wang et al. formed a PVDF/ $BaTiO_3$ nanocomposite to observe the effect of the permittivity of the film on TENG performance [151]. They fabricated a self-polarized TENG with a floating metal in the middle of two $BaTiO_3$ filled PVDF composites. Through the addition of $BaTiO_3$, researchers increased the dielectric permittivity of the nanocomposite layer, which resulted in an increased output performance [151]. In a different study, nano-sized $BaTiO_3$ is introduced to PDMS, EVA, PVAc, and PMMA to induce ferroelectricity to the polymer films. Researchers have seen no difference in the sign of triboelectric charges, as PDMS, PVAc, and EVA obtained a negative charge, while PMMA obtained a positive one. The piezoelectric contribution of PDMS is maximized with poling, as its lower elastic modulus allows for greater deformability. Researchers also shown that by inversely polarizing the ferroelectric dipoles to match the triboelectric charges formed after contact-separation, TENG performance can be increased substantially. PDMS/$BaTiO_3$ and PMMA/$BaTiO_3$ are selected as the triboelectric pairs because PDMS acquires a positive charge, while PMMA acquires a negative charge. PMMA / $BaTiO_3$ is poled in such a way that the negative pole of the ferroelectric dipole faces away from the substrate, while the PDMS / $BaTiO_3$ is poled so that the positive pole faces away from its substrate. By using a matched dipole configuration with the triboelectric charges, researchers obtained a V_{OC} and power density of 460 V and 143.2 mW m^{-2}, respectively. When compared with the mismatched version, 300 V and 91.6 mW m^{-2} is obtained, demonstrating that aligning ferroelectric dipoles with triboelectric charges is just as crucial as selecting the appropriate additives [152].

Metal nanoparticles, such as Au or Ag NPs, are also used to facilitate higher performance in TENGs [140,141,153]. In a particular example, Zhang et al. introduced Ag NPs with varying sizes to silica gel in order to observe its effect on triboelectric performance. (Fig. 15 **(d)**) [154]. They have seen that the particle size directly affects the output performance of the silica gels, with the smallest being 20 nm in size giving the best results (Fig. 15 **(e)**). These results are again attributed to improved dielectric constant on top of increased contact area between the Ag NPs and silica gel, which resulted in increased charge generation [154].

1D nanostructures, such as nanowires are also used to form nanocomposites [142,155]. Moreover, composite nanofibers are also formed by various techniques to yield better performance for TENGs [156,157]. For example, Doganay et al. used silver nanowires (Ag NWs) to obtain conducting textiles, then used a TPU lamination to obtain TPU/Ag NW fabrics in 2021. Composite fabrics obtained from higher density TPUs performed much better without sacrificing the electronic conductivity, which is also resistant to mechanical bending and washing [143]. Compared with PDMS, PI, Ecoflex and PLA, the best triboelectric pair is formed with PLA, in which composite fabrics with higher loading of TPU performed much better than the lighter one. Kang et al. also used Ag NWs to form an Ag NW/Polymer hybrid system with PMMA and PVC spin coated onto Ag NW deposited substrates (Fig. 15 **(f)**) [158]. Mesh

structure formed by Ag NWs on the top of PMMA or PVC polymer changes the surface potential, making PMMA more tribonegative and PVC more tribopositive. Mechanisms for different triboelectric pairs such as nylon and PFA is given in Fig. 15 **(g)**, where AgNW-polymer hybrids can be paired with both tribopositive and tribonegative materials and still perform very good due to the interface created by Ag NWs. Another example of 1D nanostructure is carbon nanotubes (CNTs). Kim et al fabricated a PDMS/CNT composite triboelectrification layer, with improved mechanical and electrical properties due to the addition of CNTs [159]. With the additional fluorocarbon plasma etching applied to reveal CNT structures on top of the PDMS layer, the triboelectrification is further improved [159]. Last but not least, Pu et al. introduced aligned zinc oxide (ZnO) NWs into electrospun PVDF and Nylon-11 nanofibers to obtain TENGs. ZnO NW addition to polymeric nanofibers again increased the output performance, on top of increasing mechanical and thermal stability [160].

Another interesting study involved addition of goethite nanowires (α-FeOOH) to a polymeric matrix of polyether block amide (PEBA), which is conducted by Blums et al. in 2022 [161]. Herein, with a small addition (0.5 vol%) of α-FeOOH nanowires, surface charge density is improved from 0.069 to 0.93 nC cm^{-2}. Researchers extensively investigated the reason behind this triboelectrification enhancement, which is explained by the hydrogen bonding between α-FeOOH and carbonyl (-C═O) groups in PA blocks or polyether (PE) blocks of elastomeric PEBA matrix. Surface hardness measurements using nanoindentation are also employed, where an improved hardness and elastic modulus are observed particularly with 0.2 and 0.5 vol% α-FeOOH addition. This is attributed to the previously mentioned hydrogen bonding, which

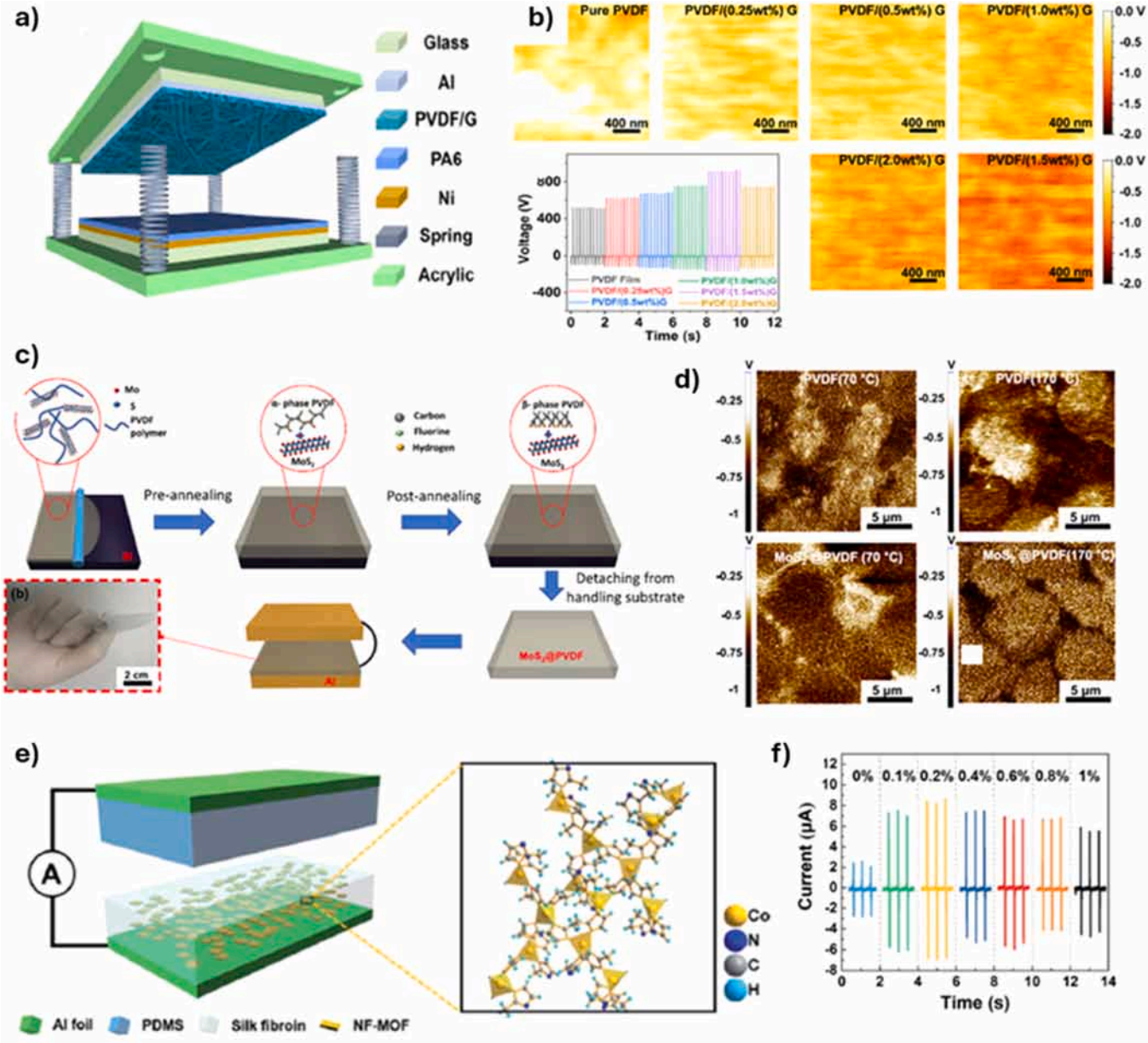

Fig. 16. Examples of 2D additives for TENGs. a) Graphene as a 2D additive for electrospun PVDF fibers. b) KPFM images of electrospun PVDF fibers with different graphene addition and their respective Voc outputs. c) Liquid exfoliated 2D-MoS2 addition to PVDF films. d) KPFM images show different polarization due to formation of β-crystal phase of PVDF due to 2D-MoS_2 addition. e) Addition of cobalt based-MOF nanoflakes to silk-fibroin. f) Output currents of MOF/Silk fibroin composites showing maximum output performance at 0.2 wt% of MOF addition.
(a) and (b) Reproduce with permission from Ref. [145]. Copyright 2021, Elsevier. (c) and (d) Reproduce with permission from Ref. [165]. Copyright 2022, American Chemical Society. (e) and (f) Reproduce with permission from Ref. [168]. Copyright 2022, Royal Society of Chemistry.

induces macromolecular order within the PEBA matrix. This is evident in the heterogeneous hardness maps of α-FeOOH/PEBA, attributed to α-FeOOH addition, which is reported to enhance the material transfer mechanism.

Recently, the use of 2D nanomaterials to modify TENG layers has also been on the rise [132]. These include graphene, transition metal dichalcogenides (TMDs), titanium carbides, or MXenes [145,162–167]. For example, Shi et al. introduced graphene nanosheets into electrospun PVDF fibers to improve triboelectrification (Fig. 16 **(a)**) [145]. Authors found out that graphene nanosheets improve the triboelectric performance due to enhancement of surface potentials shown by KPFM (Fig. 16 **(b)**). According to the graphene content, they have optimized the surface potential and obtained PVDF fibers loaded with graphene nanosheets for the best output performance at a graphene content of 1.5 wt%. Similarly, Hedau et al. used liquid-phase exfoliated MoS_2 to enhance the surface potential of PVDF (Fig. 16 **(c)**) [165]. They have seen that the incorporation of MoS_2 sheets promoted the β-phase of PVDF, which has nonzero dipole moments. These newly formed β-phase of PVDF is said to increase potential difference between positive and negative charges, resulting in a repressed recombination of these two charges after triboelectrification. This "self-poled" structure was observed via KPFM, which had shown a unique distribution of surface charges (Fig. 16 **(d)**). According to the loading content and the heat treatment, best performance was achieved which has also shown the most negative surface polarization according to KPFM imaging. This is attributed to the formation of the β-crystal phase of PVDF due to the addition of MoS_2, which has the highest degree of polarization per unit cell [165]. Apart from these general examples, Chen et al. introduced metal-organic framework (MOF) nanoflakes into silk fibroin for enhanced triboelectrification (Fig. 16 **(e)**) [168]. It is noted that the MOF nanoflakes increase the capacitive performance of the composite film due to their high aspect ratio which is possibly forming nanoscale capacitors across the composite that yielded 9 times better output performance than its bare counterpart (Fig. 16 **(f)**) [168]

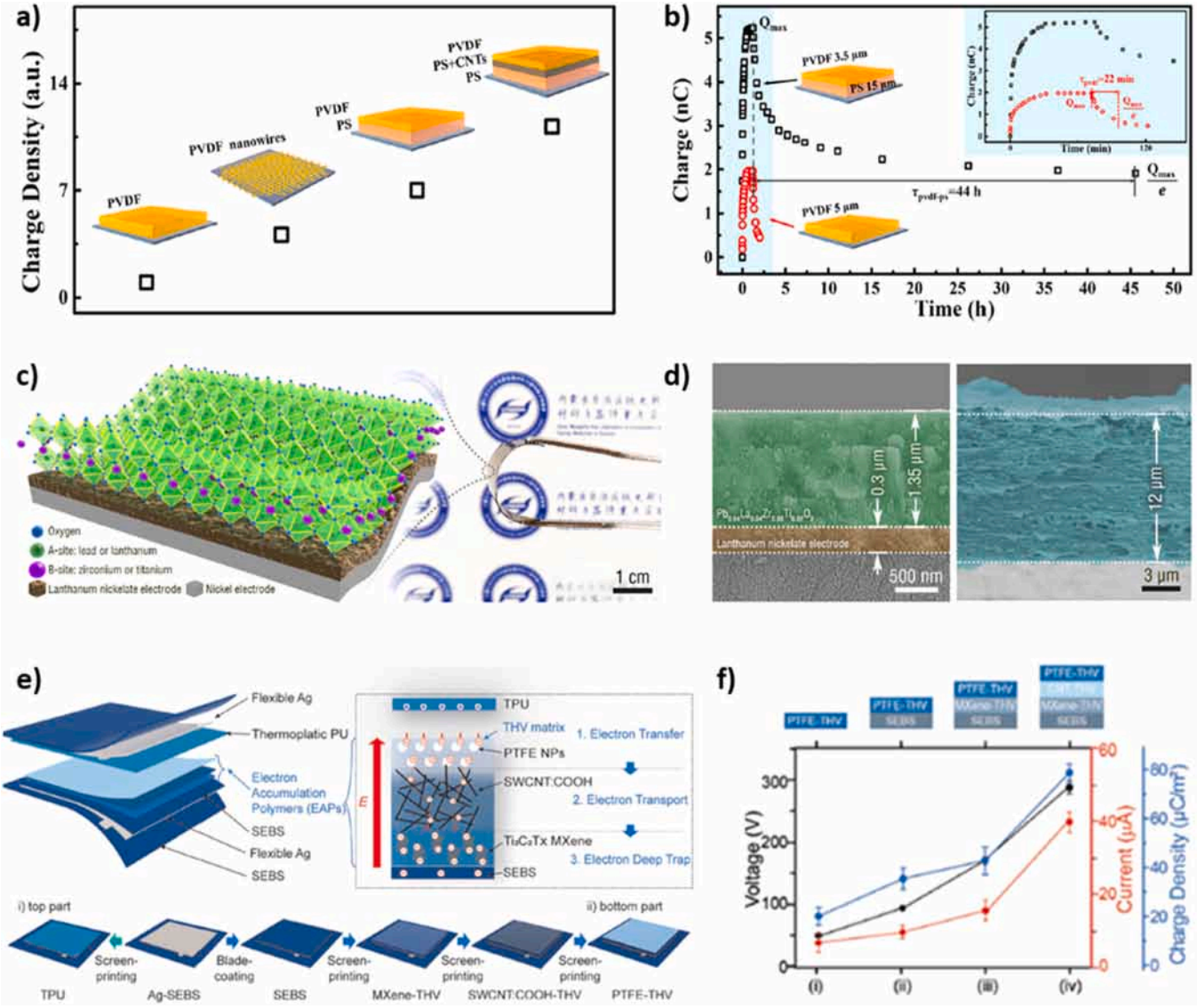

Fig. 17. Examples of composite structures for TENGs. a) Transport process of triboelectrified electrons on a tribonegative layer. Improvement in the charge density per added layer, ultimately forming PVDF/PS+CNT/PS structure. b) Charge accumulation and decays for bare PVDF and hierarchical structure. c) Schematic structure of TENG and detailed schematic of inorganic PLZT antiferroelectric ceramic structure on flexible nickel electrode. d) Cross-sectional and top-view SEM images. e) Schematic design of TENG device with electron accumulation polymers as a layer for improved performance, and its mechanism of charge accumulation. The fabrication process is also given. f) Resulting performance of TENGs with each added triboelectric layer.
(a) and (b) Reproduce with permission from Ref. [170]. Copyright 2016, American Chemical Society. (c) and (d) Reproduce with permission from Ref. [171]. Copyright 2021, Elsevier. (e) and (f) Reproduce with permission from Ref. [172]. Copyright 2022, Wiley-VCH.

3.1.3.3. Intermediate layers. In the case of the TENGs without intermediate layers, upon triboelectrification, there is a chance that the electrons gathered on the surface may drift back to the dielectric layer, resulting in the recombination with the opposite charges. This, ultimately, reduces the effective surface charge density and thus, the output performance of TENGs [169]. First reported hierarchical design is done by Cui et al. exploring the addition of interlayers as a means to improve the efficiency of PVDF friction layer (Fig. 17 **(a)**) [170]. Addition of PS and PS-CNT layers under the PVDF friction layer improved the charge density up to 11.2 times (Fig. 17 **(a)**). Herein, PS-CNT layer works as a transport layer, while PS underneath it increases the dielectric of the composite structure. The performance increase is also explained with the charge decay process, where multilayer structure had much longer decay times (Fig. 17 **(b)**) [170].

In recent years, several new studies have adopted a similar approach, but with significantly different choices in layer composition and material selection. Jiang et al. used a simple Ag NP/rGO hybrid interlayer between the PVDF and current collector and improved the output performance by 500 % [133]. rGO is said to increase triboelectrification due to its high permittivity originating from its oxygen-containing groups and defects, and its ability to trap charges [133]. Zhang et al., on the other hand, used a novel inorganic antiferroelectric ceramic between PVDF and current collector [171]. The schematic structure of the TENG device and unique structure of the antiferroelectric material, $Pb_{0.94}La_{0.04}Zr_{0.98}Ti_{0.02}O_3$ (PLZT), is provided in Fig. 17 **(c)**. The formation of the PLZT structure was observed by SEM and given in Fig. 17 **(d)**. By using the antiferroelectric material PLZT instead of a ferroelectric one, the authors reduced charge losses associated with large remnant polarization. This way, they exploited the dielectric polarization which enabled the use of large polarization difference effects. They compared this interlayer with the ferroelectric one, seeing a large improvement in both open circuit voltage and short circuit current, although achieving smaller surface polarization [171]. Kim et al. fabricated all-printed TENGs containing 3 layers which contribute to the triboelectrification [172]. PTFE introduced terpolymer of tetrafluoroethylene, hexafluoropropylene, and vinylidene fluoride (THV) works as the primary triboelectrification layer, while SWNT incorporated THV and MXene incorporated THV layers work as electron transport and electron deep trap layers (Fig. 17 **(e)**), respectively. Here, SWNT filler is reported to enhance the transfer rate of the polarized electrons to the electrode, while MXene filler helps to store them due to the formation of trapping states. Electron trapping ability is also measured with a metal-insulator-semiconductor device. The improved electron trapping ability is observed with MXene loaded layers by the hole accumulation in the stretchable substrate/p-Si interfaces. This is attributed to trapping sites generated from MXene. With each added layer, the authors improved the overall output performance, demonstrating that engineering each layer of the TENGs for specific tasks is highly feasible (Fig. 17 **(f)**)[172]. In general, by controlling the electronic/ionic conductivities, dielectrics, and inherent capacitances and piecing different layers in order, one can greatly improve the output performance of TENGs.

3.1.3.4. Multilayered and 3D architectures. Apart from modifying the layers with physical/chemical alterations or additives, the overall structure of the TENGs is also important for their overall performance metrics. Designing various architectures to increase the number of simultaneously triboelectrified layers or laminating multiple triboelectric layers can significantly enhance performance. One of the first examples comes from the group of Prof. Zhong Lin Wang, where a multilayered TENG with five layers of units are constructed [173]. Kapton films are prepared in a zig-zag shape, and for each layer, Al-coated PTFE thin films and Al foils with nanoporous surfaces are used. These parallel-connected five-layer TENGs can generate Isc and Voc of 0.66 mA and 215 V, respectively. A similar multi-layer stacked structure is used in a much recent study from the same research group, where a rotation-to-translation mechanism is demonstrated [174]. Schematics of the multi-layer stacked (MLS) TENG and its motion conversion mechanism are provided in Fig. 18(a). Herein, sliders and stators are directly stacked, while the sliders are connected to rods. Sliders utilized acrylic as the substrate and nylon as the friction material, while stators used PTFE as the friction material and Cu as the current collector. The substrate of the stator, on the other hand, is fabricated from paper, foam, and acrylic. With the rotation of the cylindrical cam shown in Fig. 18(a), the rotational power is converted to a linear reciprocating motion. Each added layer considerably increases the output performance of the MLS-TENG, where a Voc increase from 860 V to 2410 V for 5 stacked layers is reported. The unique rotation-to-translation conversion mechanism, on top of the stacked design of the TENG architecture, allowed researchers to obtain an energy level of 2 mJ min^{-1} in an actual river.

Complete 3D architectures are also explored for TENGs for improved output performance or for niche applications. An earlier example of such architecture utilized layer-by-layer stacked PVC and Al as friction materials, where an in-plane sliding mode is devised. This 3D multi-layered structure allows the friction of multiple layers at the same time, greatly enhancing the areal energy output, although no mention on the volumetric output is made. With as many as 40 layers, Voc of 800 V and Jsc of 5.5 mA m^{-2} are obtained, proving that a 3D structure can surely improve the output performance per unit area [175].

One unique 3D architecture is demonstrated by again Prof. Wang's group, where the researchers utilized a hybrid UV 3D printing method to obtain a 3D-TENG [176]. Different from the general working mechanism of TENGs, this 3D architecture uses printed composite resin parts and ionic hydrogel for triboelectrification layer and current collector. The schematic structure is provided in Fig. 18(c), whereas the photographs show the printed ultra-flexible skeleton of the 3D-TENG. With newly developed hybrid 3D printing, researchers are able to produce ultra-flexible parts by a single-step manufacturing process, in which the liquid photopolymer resins and support materials are directly printed within an integrated platform. This method allowed the fabrication of different shapes with a precision of 1.0 μm thickness. Fig. 18(d) shows the important parameters that are used to fabricate these structures. By controlling dimensions, the output performance of the 3D-TENGs is optimized, which is provided in Fig. 18(e). The most important aspect of this research is the unique architecture that allows the triboelectrification by only compressing/flexing the 3D-TENG, showcasing its promise for wearable devices.

One different example is demonstrated by Šutka et al., in which stacked polymer layers with different triboelectric properties separated by a mesh are utilized. Adding meshes in-between the polymer bilayers allowed the microscopic dipole formation due to the triboelectrification, which is aligned due to the different triboelectric properties of the layers. With the utilization of the triboelectric layers and unique way to separate bilayers, a piezoelectric coefficient comparable to that of piezoelectric polymer materials is reported without the need for poling. Creating a 3D structure by incorporating PP meshes of varying thicknesses yielded a Voc of 29 V and an Isc of 15 nA [177].

Laminating the triboelectric layers for scaling the power/energy output for volumetric electric output is the most important aspect of having 3D structures [178]. A great example of a volumetric TENG device to scale the output is demonstrated again by Šutka et al. in 2023. 30 bilayers of triboelectric laminates are fabricated using electrospinning [179]. Similar to their previous work, volumetric dipoles are introduced to TENGs with the help of sequential electrospinning of polymer fibers with large and small diameters. When fibers with larger diameters are electrospun onto smaller ones, the layers at the interface slide over each other, leading to internal contact electrification. Conversely, when smaller diameter fibers are electrospun onto larger fibers, they create an interconnected network with strong adhesion, leading to a nonslip interface. This arrangement of well-defined interfaces results in parallel

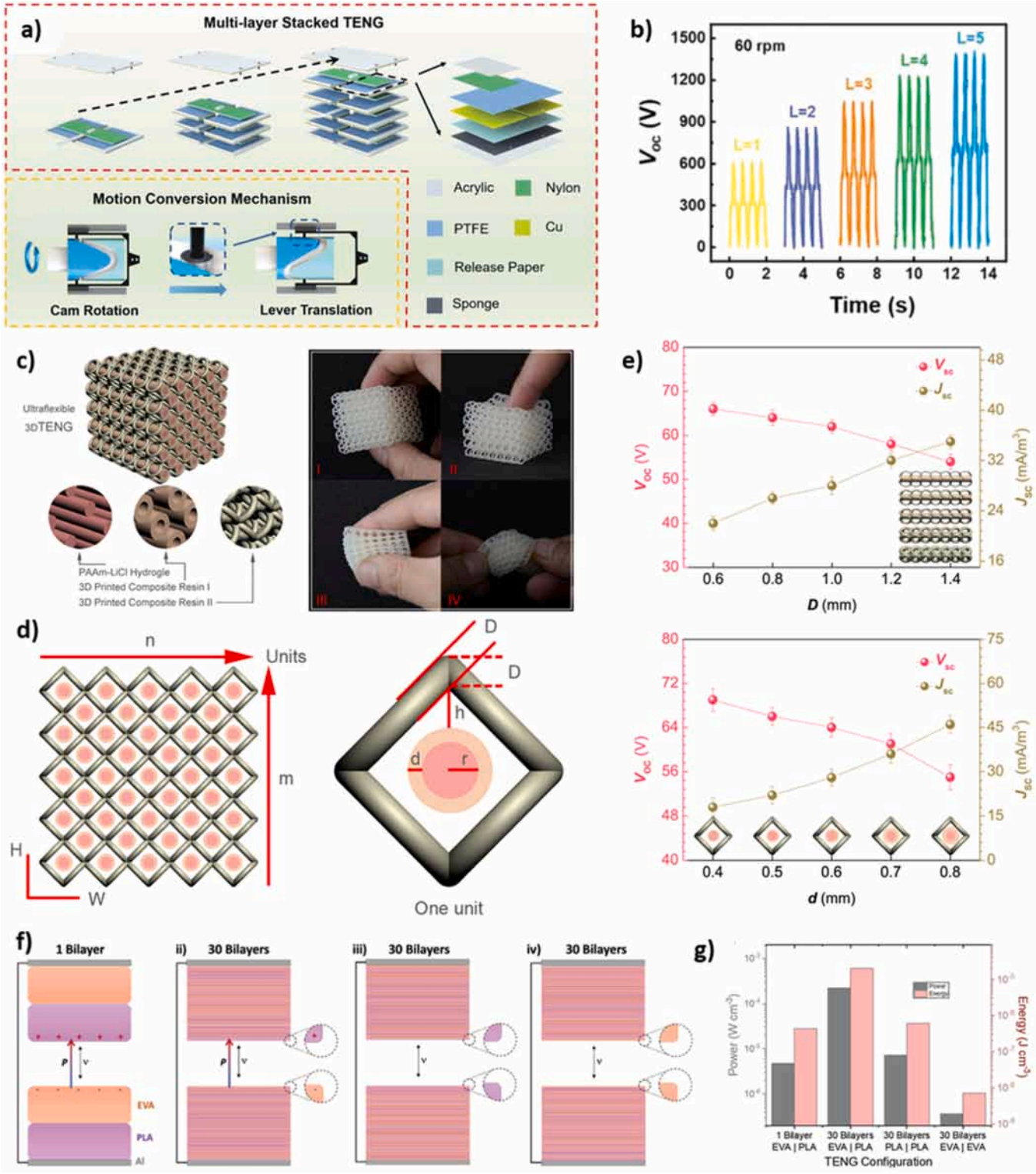

Fig. 18. 3D TENG architectures to improve output performance. a) Schematics of the multi-layered (MLS) TENG and its energy conversion mechanism. b) Voc of the MLS-TENG based on the number of stacked layers. c) Schematic diagram and the images of the 3D-printed ultra flexible TENGs. d) Diagram showing the important parameters of the 3D-TENG. e) Voc and Jsc of 3D-TENGs based on different dimensions. f) Diagram showing contact between two individual bilayers of EVA and PLA, and contact between 30 bilayer laminates of EVA/PVA, PLA/PLA, and EVA/EVA. g) Volumetric energy and power outputs of laminated TENGs.
(a) and (b) Reproduce with permission from [174]. Copyright 2022, Wiley-VCH. (c,d,e) Reproduced with permission from [176]. Copyright, 2018, Elsevier. (f) and (g) Reproduce under Creative Commons CC BY 4.0 from [179].

dipole moments forming within the bulk of the laminate. EVA (diameter of 2.3 μm) and PLA (diameter of 0.14 μm) are chosen to produce these alternating layers for obtaining a volumetric dipole formation. Smaller PLA fibers are integrated into the larger EVA networks with the help of sequential deposition. Overall schematics and charging mechanisms of 1 bilayer of EVA/PLA and 30 bilayers with a separation layer of EVA/PLA, PLA/PLA, and EVA/EVA, respectively, are provided in Fig. 18(f). In the case of 30 bilayers of EVA/PLA, the dipoles generated at the major contact separation interface align with the internal dipoles due to the dipole-dipole induction. In other cases, these dipoles are not aligned, reducing the overall performance of the TENGs. This is demonstrated by the volumetric power and energy output of 30 bilayers of EVA/PLA, reaching up to 221 $\mu W\ cm^{-3}$ and 19.98 $\mu J\ cm^{-3}$.

Overall, optimizing the architecture to form multilayered or 3D TENGs has been shown to significantly enhance their output performance. Although this topic is not the main focus of this section, it is worth noting that stacked or 3D structures enable innovative applications, ranging from blue energy harvesting to wearable devices for IoT applications. It is also important to recognize that the strength of TENGs lies in their electrical output on 2D surfaces. Therefore, the fabrication of volumetric devices should ensure significant volumetric power and/or energy output to be considered viable for further research.

3.2. Strategies for enhanced energy transfer and storage efficiency

Today most electronic circuits have strict power requirements. Commonly their input voltages are limited to between 0–12V DC. For using the pulsed, high-voltage AC output of TENGs as a power unit, specialized power regulating circuits are essential. These circuits modify the TENG-generated signals, making TENGs viable as power units in various applications [180]. TENG specialized power regulating circuits mainly include charge boosting, power conversion, and energy storage units.

3.2.1. Charge boosting strategies

TENGs inherently have low capacitance, which results in high impedance. This characteristic leads to the generation of high voltage, yet the current output remains comparatively low. Consequently, integrating TENGs directly into a low impedance system such as commercial appliances yields a diminished power output [181]. For overcoming this problem circuit design plays a crucial role not only in converting the output but also in enhancing the overall efficiency of the system [182]. These improvements in efficiency may include augmenting the energy output of TENG cycles or increasing the charge delivered to the system by integrating additional TENG units.

3.2.1.1. Cycle for maximized energy output. A TENG cycle consists of contact and subsequent separation of the material surfaces. At the beginning of each cycle, opposite charges accumulate on surfaces due to contact electrification. When the surfaces are separated, potential differences across the electrodes vary with the degree of displacement which balanced with electrostatic induction. This continuous movement induced electrons to shift between electrodes to maintain equilibrium. By considering the charge transfer between electrodes as Q and the potential difference across them as V, a TENG cycle can be effectively illustrated using a V-Q plot [183]. To obtain such data, two simultaneous measurements must be done. One to measure potential difference between electrodes and another to measure the transferred charge between electrodes. Any TENG cycle is represented as a curve enclosing an area in the V-Q plot. The area of the enclosed space represents the energy output of that cycle, also called the cycle of energy output (CEO). Fig. 19 **(a)** presents a V-Q curve for a free-standing TENG system. At the initial neutral state, both the potential difference and the charge are zero. With the first contact and ensuing contact electrification, charges begin to transfer between the electrodes upon separation, a process that repeats with each subsequent cycle. After several cycles, the system attains a steady state, consistently generating a constant energy output.

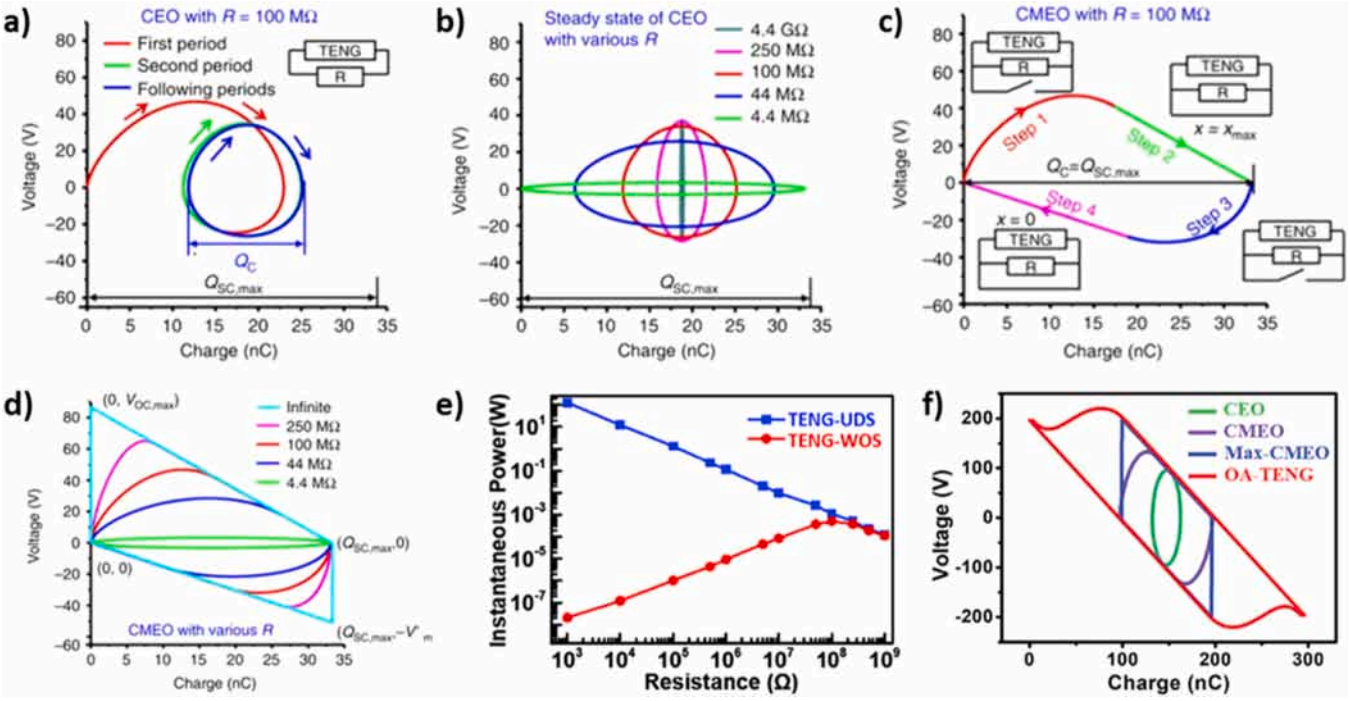

Fig. 19. Energy output and performance metrics of TENGs. (a) CEO plot of a free-standing TENG system with an external load resistance of 100 MΩ. (b) Steady state CEO plots of various external load resistances. (c) Voltage – charge plot and operation of CMEO condition with external load resistance of 100 MΩ. (d) The CMEO plot for a variety of external load resistances. (e) Comparison of conventional and CMEO TENG conditions for peak power at different external resistances. (f) Voltage-charge plot comparison of CEO, CMEO with finite resistance, CMEO with infinite resistance, and OA-TENG.
(a)–(d) Reproduce with permission from Ref. [183]. Copyright 2015, Nature Publishing Group. (e) Reproduce with permission from Ref. [184]. Copyright 2018, Wiley-VCH. (f) Reproduce with permission from Ref. [190]. Copyright 2019, Wiley-VCH.

As illustrated in Fig. 19 **(b)**, the shape of the enclosed area in the V-Q curve of a TENG system varies depending on the external load connected to it. With a larger load, there is an increase in voltage but a decrease in charge, while the reverse is true for smaller loads. In fact, the area of the CEO is reducing as the impedance of the system deviates from the matched impedance. Comparing the enclosed area of the CEO, the electric performance of different systems and conditions can be compared [183].

To enhance the CEO of a TENG cycle, a circuit incorporating a mechanical switch is utilized. This switch short-circuits the system at its maximum and minimum displacement points, forming what is known as Cycles for Maximized Energy Output (CMEO). The working principle of CMEO, as illustrated in Fig. 19 **(c)**, involves the instantaneous short-circuiting of the system at its maximum or minimum displacement. This action allows charges to rapidly flow from one electrode to another, neutralizing the potential difference and generating a high current instantaneously. Moreover, Fig. 19 **(d)** demonstrates that increasing the resistance significantly enhances the energy of each cycle. Therefore, operating the CMEO under open-circuit conditions during the cycles results in the highest energy output. As depicted in Fig. 19 **(e)**, when compared to conventional TENG systems referred to as TENG-UDS in the figure, CMEO denoted as TENG-WOS in the figure exhibit enhanced efficiency, particularly at lower external impedances [184]. These findings indicate that the high-power output of CMEO at lower impedance levels makes it well-suited for integration into commercial electronic circuits. The promising potential of CMEO has led to the exploration of various designs and applications. A key focus among these is the incorporation of a mechanical switch that activates at the system's maximum and minimum displacements. Cheng et al. successfully applied CMEO to both contact separation and sliding mode TENG system using mechanical switches and achieved instantaneous power of 142 W at 500 Ω while regular TENG configuration had only 18.8 nW output power [185]. Recently, Shang et al. integrated mechanical switches for CMEO configuration to free-standing mode TENG boosting the output energy from 11.1 to 49.5 μJ at 333 MΩ [186]. Additionally, Yang et al. recently applied CMEO mechanical switch to the DC-TENG system. This integration allows the enhancement of the output power while operating at lower impedance levels [187].

Beyond mechanical switches, CMEO technology can be leveraged through automatic switching systems. These systems operate by harnessing the electrostatic force produced by the TENG couple throughout its cycle. The functioning of the switch is entirely dependent on the varying charge levels between the TENG materials and their specific position in the cycle. Qin et al. implemented an electrostatic vibration switch that automatically shorts-circuits depending on the electrostatic force generated by TENG electrodes. The actuation of the switch occurs at maximum displacement, automatically bringing the system into the CMEO condition [188]. In a similar context, Cheng et al. used the air discharge as a technique to activate an automatic CMEO system [189]. Furthermore, while CMEO is often seen as the maximum of a TENG system's efficiency, recent findings of Xu et al. suggest that this upper limit can be surpassed. By integrating an LC oscillating circuit referred to as OA-TENG, the efficiency of TENG systems can be further enhanced, as evidenced by the V-Q plot comparison presented in Fig. 19 **(f)** [190]. This highlights the critical role of power management circuits in surpassing the current performance limits of TENG systems.

3.2.1.2. Charge pump. Charge pumping represents an additional approach to enhance the electrical performance of a TENG system. This method involves integrating either multiple or a single 'pumping' TENG couples alongside the primary TENG couple [191]. The charge generated by these pumping TENGs is directed through a rectifier before being connected to the main TENG. This setup facilitates the storage of excess charge within a structure known as a plane-parallel capacitor. This setup enables the storage of excess charge within a plane-parallel capacitor, allowing the system to accumulate charge while maintaining its normal operation. The main TENG adopts the characteristics of both a classical TENG and a capacitor increasing its charge density. Charge pumping is a technique employed to attain high charge densities in TENG devices without the risk of losing charges due to air breakdown.

The operational principle of charge pumping in TENG systems is graphically shown in Fig. 20 **(a-i)** [192]. Initially, both TENG couples get to contact state from their neutral state (Fig. 20 **(a-ii)**). While the main TENG stays stationary, pump TENG generates AC output with each cycle. Output of pump TENG is passed through a rectifier, accumulating charges on the electrodes of the main TENG as depicted as a cycle in Fig. 20 **(a-iii and iv)**. In this configuration the main TENG has a similar structure to a capacitor. To optimize capacitance and increase stored charge density, the main TENG is maintained at a minimum displacement. This charging process can continue until the dielectric breakdown

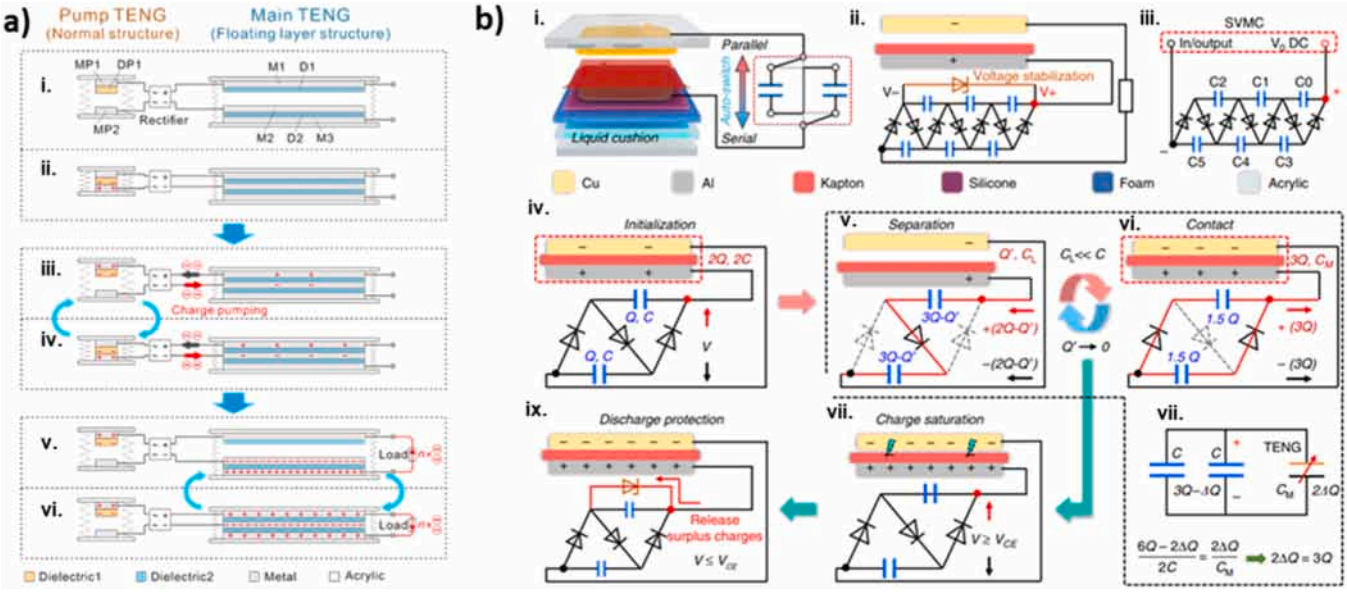

Fig. 20. Operational principles of charge pumping in TENG system. (a) Operational flow of a main TENG integrated external charge pump. (b) Operational flow of a simplified self-charging circuit integrated TENG.
(a) Reproduce with permission from Ref. [192]. Copyright 2018, Elsevier. (b) Reproduce with permission from Ref. [195]. Copyright 2019, Nature Publishing Group.

voltage of the dielectric layer is reached. Once a sufficient charge accumulates on the floating electrodes, the main TENG initiates its own contact-separation cycle depicted in Fig. 20 **(a-v and vi)**. The charges present on the floating layer of the main TENG induce charges on the TENG electrodes through electrostatic induction increasing the charge density. This approach not only enhances the efficiency of charge accumulation but also broadens the operational dynamics of the TENG system. Naturally, TENGs have an inherent limitation on their maximum charge density, constrained by the breakdown conditions of their surrounding environment. However, incorporating a charge pump into TENG devices offers a solution to this challenge. By using a charge pump, it becomes possible to exceed these inherent limits and achieve higher charge densities. This allows for the achievement of higher charge densities without being hindered by the constraints of environmental breakdown, thereby enhancing the overall efficiency and effectiveness of TENG systems. Compared with other methods aiming to increase charge density, such as corona charging or the creation of a high vacuum to prevent air breakdown, charge pumping stands out as a more facile and feasible process [191]. Xu et al. demonstrated its potential by achieving an impressive surface charge density of 1020 μC m^{-2}, surpassing the results previously attained with corona charging and vacuum methods [192]. Moreover, Bai et al. demonstrated that the application of charge pumping is not confined to contact-separation mode TENGs; it is equally effective in sliding-type TENGs boosting average power more than 15 times compared to conventional TENG systems [193]. Additionally, Yang et al. showed that the efficiency of sliding TENG-based energy harvesters is further enhanced through the implementation of power management circuits obtaining remarkable charge density of 1328 μC m^{-2} [194]. This versatility broadens the scope of charge pumping, making it a valuable and adaptable approach in the field of TENG technology.

A TENG system's own output can be employed for self-charge pumping instead of utilizing an external TENG couple [195]. This is achieved by incorporating a voltage multiplying circuit, which consists of multiple capacitors. The circuit shifts the connection between capacitors from serial to parallel configuration and vice versa, as illustrated in Fig. 20 **(b-i)**. The actual circuit used for charge-pumping involves a series of capacitors, rectifier diodes, and a single Zener diode, connected as shown in Fig. 20 **(b-ii and iii)**. The rectifier diodes serve to alter the capacitor configuration based on the current direction. The capacitors are used for storing and pumping charges to the TENG. The Zener diode maintains the voltage at a threshold level to prevent air breakdown. As depicted in Fig. 20 **(b-iv)** TENG cycle starts in a neutral state and is activated through contact electrification of the dielectric surfaces. As the electric field forms, electrodes acquire opposite charges. The TENG's capacitance is high due to minimal displacement. During separation, charges transfer between the electrodes to maintain equilibrium, reducing capacitance as shown in Fig. 20 **(b-v)**. In this phase, the diodes allow current in one direction, setting the capacitors in serial configuration. At maximum displacement, the charges on TENG electrodes are at their lowest, but the capacitor charges are at their peak. When the movement reverses, the capacitors shift from serial to parallel configuration due to the change in current direction. As the electrodes come closer together, the capacitors transfer charge to the TENG as depicted in Fig. 20 **(b-vi)**. However, the shift from serial to parallel configuration results in a higher charge being supplied to the TENG compared to what it initially gave to the capacitors. The simplified version of the equivalent circuit and charge transfer mechanics are provided in Fig. 20 **(b-vii)**. Consequently, with each cycle, the charges on both TENG electrodes and capacitors incrementally increase until air breakdown occurs as illustrated on Fig. 20 **(b-viii)**. To manage this issue, a Zener diode is placed between the positive and negative terminals as shown in Fig. 20 **(b-ix)**. The Zener diode permits reverse current flow once a certain potential difference is reached, thus regulating the voltage, and preventing air breakdown [195]. Similar to external charge pumping, Long et al. implemented self-charge exciting to sliding mode TENG achieving a charge density of 71.53 μC m^{-2}, 5.46-fold increase compared to a conventional sliding TENG [196]. This approach further broadens the versatility and utility of TENG technology, demonstrating its adaptability across different modes of operation. Additionally, Liang et al. demonstrated the strategy of connecting an array of TENGs in series. By serially connecting multiple blue energy harvesting spheres through voltage-multiplying circuit, 208 times boosted current of 25.1 mA obtained [197].

3.2.2. *Power management circuits and strategies*

In modern electrical systems, which predominantly consist of low impedance units requiring direct current, a relatively low and stable voltage, and high current, the outputs of TENG devices require conversion before they can be utilized as power supplies [198]. To adapt the output of TENG devices for these requirements, several modifications must be made: the AC output needs to be converted to DC, the high voltage output should be reduced, and the low current output must be increased. There are various methods to achieve these objectives. AC-DC rectification is used to convert the AC output of TENGs to DC, except for DC-TENGs which inherently produce DC, thus eliminating the need for this conversion. For adjusting voltage levels, AC-AC conversion can be done using inductive transformers, which alter the voltage while maintaining the current form as AC. Alternatively, DC-DC conversion, often executed through capacitive transformers, is used to adjust the voltage levels of DC currents. Additionally, various other electronic components are employed to ensure a stable power output. Each of these methods plays a crucial role in tailoring the unique output characteristics of TENG devices to meet the specific demands of modern electrical systems.

3.2.2.1. *Current regulation circuits*

3.2.2.1.1. Rectifier circuits. For an AC current to be converted into DC current, rectifier circuits are necessary. Rectifiers utilize the unidirectional property of diodes creating distinct paths for forward and reverse current to pass through. The most common types of rectification circuits used in TENG systems include the full-wave rectifier, half-wave rectifier, and Bennett's Doubler voltage rectifier, with their circuit diagrams presented in Fig. 21 **(a)**. The operation of these circuits relies on the fundamental principles of a closed circuit for current flow [199]. Considering a TENG system that generates forward current upon contact and reverse current during separation, it's evident that each type of current will follow a different path in the rectification circuits. The full-wave rectifier utilizes two sets of diodes, totaling four, ensuring that both forward and reverse currents are directed to the capacitor from the same direction, thereby generating DC. The half-wave rectifier operates on a similar principle, where during the forward current, a diode blocks the alternate path, forcing the current through the capacitor during the reverse current, it creates a closed circuit that bypasses the capacitor, linking directly back to the TENG system, passing only the half of the waves. Bennett's Doubler rectifier circuit differs from previous methods by incorporating two capacitors. It has the same working mechanism as the self-charge pumping method discussed earlier. During forward current, the capacitors are connected in series; during reverse current they shift to a parallel configuration. The output voltage of this circuit is influenced by the capacitance ratio of these two capacitors, offering a unique method of voltage doubling and rectification tailored for TENG systems [199].

Contrary to what might be anticipated, comparisons between full-wave and half-wave rectifiers have revealed that the half-wave rectifier is more efficient, despite utilizing only half of the generated current [200]. This unexpected efficiency of the half-wave rectifier over the full-wave variant is attributed to its charge supplement channel. This channel effectively shortens the circuit during the reverse current, transferring charges directly from one electrode to another. This mechanism helps to maintain a specific charge density on the electrodes,

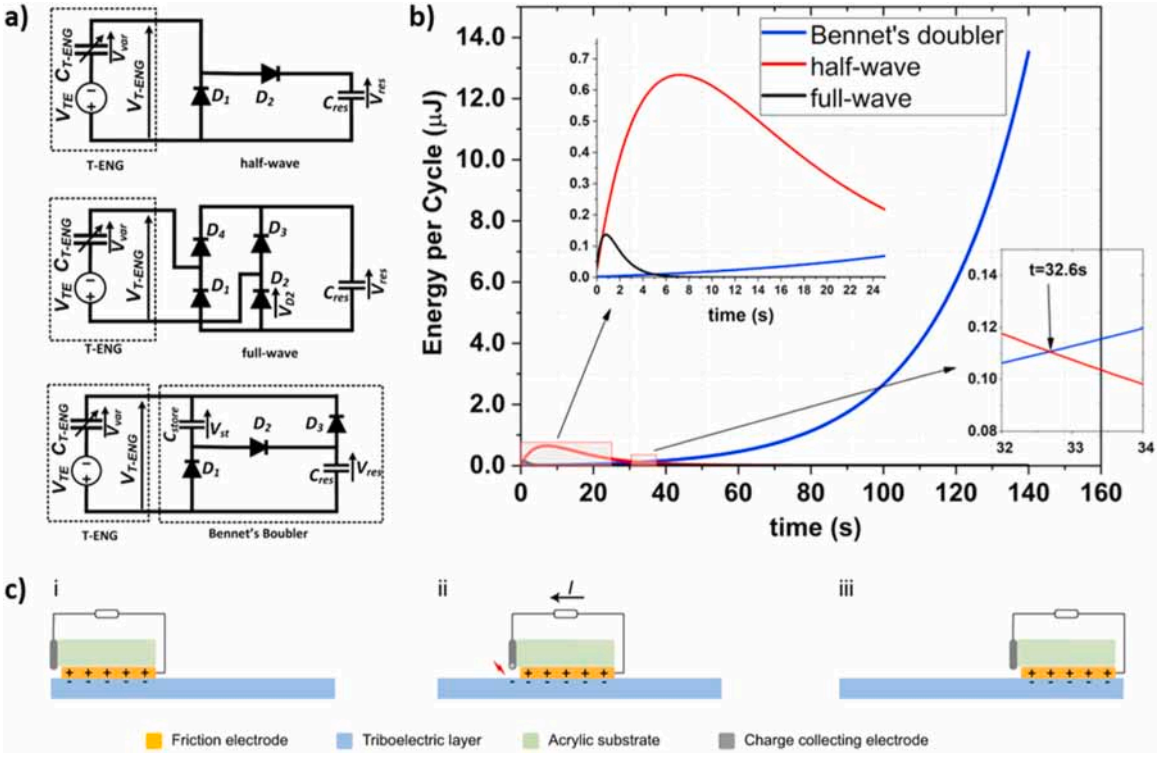

Fig. 21. Comparison of rectifier circuit configurations for TENG applications (a) Circuit diagram of the half-wave rectifier, full-wave rectifier, and Bennett's Doubler voltage rectifier circuits flow. (b) Energy generated per cycle comparison of full-wave rectifier, half-wave rectifier, and Bennett's Doubler voltage rectifier circuits flow. (c) Working mechanism of a DC-TENG.
(a) and (b) Reproduce with permission from Ref. [199]. (c) Reproduce with permission from Ref. [206]. Copyright 2021, Nature Publishing Group.

amplifying overall DC output. Furthermore, the half-wave rectifier surpasses the full-wave rectifier in terms of energy production per cycle, showing its superiority for efficient rectification in TENG systems [201].

In a comparative analysis of the energy output per cycle among all three rectification circuits, including Bennet's Doubler voltage rectifier, Ghaffarinejad et al. observed that Bennett's Doubler exhibits an exponentially increasing energy output over time, as depicted in Fig. 21 **(b)** [202]. Initially, it generates less energy compared to the other rectification methods, but it gradually compensates for this initial shortfall as the charges stored in capacitors build up, eventually surpassing the alternatives as it reaches saturation. This unique characteristic of the Bennett's Doubler voltage rectifier enables it to outperform both half-wave and full-wave rectifiers over time. For the same TENG system, while the capacitors in the half-wave and full-wave rectifier circuits reach saturation at voltages of 165 V and 26 V, respectively, the capacitor in the Bennett's Doubler voltage rectifier circuit achieves a remarkable 835 V at 140 s. Notably, the Bennett's Doubler takes approximately 5 s to exceed the voltage of the full-wave rectifier's capacitor and 32.6 s to surpass that of the half-wave rectifier. This data highlights the Bennett's Doubler rectifier's capacity for significantly higher voltage output over time, marking it as a potential solution for maximizing energy harvest from TENG systems [202].

Aside from rectification with diodes, Qiao et al. demonstrated that mechanical rectification can also be employed for a rotary TENG system without a rectification component [203]. This design offers an alternative to traditional electrical rectification, also demonstrating the versatility of TENG technology. This method involves separating forward and reverse currents using electric brushes by altering electrode connection with rotary motion similar to those in electric motors. This approach has yielded results comparable to electrical approaches being able to light 210 LEDs simultaneously [203].

3.2.2.1.2. DC-TENG. In many instances, the pulsed AC output of a TENG is converted to a pulsed DC during the rectification process. However, DC-TENGs stand out as they naturally produce DC output, eliminating the need for this conversion [204]. This conversion can be conducted with different approaches based on triboelectric materials (dielectric, semiconductor or iontronic) used in the TENGs. The operating mechanisms of each approach have been thoroughly reviewed elsewhere [205]. The most common approach relies on the exploiting air breakdown between an electrode and a triboelectric layer, as illustrated in Fig. 21 **(c)** [206]. In this schematic two electrodes are mounted on a slider crafted from acrylic, which acts as an insulating material. Each electrode serves a different function: one is used as a friction and triboelectric layer, while the other is tasked for inducing air breakdown and charge collection. Accordingly, these electrodes are labeled based on their specific functions, with one being referred to as the friction electrode (FE) and the other as the charge collecting electrode (CCE). At the initial state (Fig. 21 **(c.i)**), contact electrification occurs between the triboelectric surface and the FE, resulting in triboelectric layer being negatively charged and the FE positively. The CCE is positioned on a slider with a relatively small distance from the triboelectric layer. By selecting a material with high triboelectric series ranking, a strong negative charge on the surface can be obtained. This property, combined with the movement of the slider generates a significant electrostatic difference between the CCE and the triboelectric layer. When this difference reaches the air breakdown voltage, charges are transferred from the triboelectric layer to the CCE as illustrated in Fig. 20(c-ii). These collected charges on the CCE are then moved to the FE through an external circuit, aiming to balance the charge between the triboelectric surface and the FE as illustrated in Fig. 20 (c-iii). Consequently, through contact electrification between the triboelectric surface and the FE, electrons move from the FE to the triboelectric layer These electrons are then drawn to the CCE due to air breakdown, subsequently transferred back to the FE, completing the cycle. Contrary to traditional TENG setups, in a DC-TENG, electron flow during the cycle is unidirectional, resulting in the generation of DC output. Similar to traditional TENGs,

DC-TENGs have shown enhanced efficiency following the optimization of material surfaces and the addition of lubricants [207], [208]. Moreover, Gao et al. showed that the design of DC-TENG systems can be further refined by incorporating rolling elements instead of sliding mechanisms, which reduces the minimum force required for mechanical motion, thereby increasing stability [209]. Additionally, Chen et al. adapted DC-TENGs for wearable energy harvesting devices through the development of conductive and non-conductive yarns. The yarns are sewed together on PTFE base for generating DC with friction. The small 1.5 cm x 3.5 cm sewn patch manages to light 416 serially connected LEDs [210]. DC-TENG technology emphasizes the significance of TENG setup, circuit design, and electrode displacement, which collectively contribute to its unique properties and solutions to common TENG challenges. Notably, DC-TENGs offer the advantage of generating high-power DC output directly, eliminating the need for a rectifier circuit. This not only saves electronic space but also avoids the slight voltage drop typically associated with rectification, presenting a streamlined and efficient approach to energy harvesting.

3.2.2.2. *Voltage regulation circuits*

3.2.2.2.1. Inductive transformer. Inductive transformers are commonly utilized in traditional electronics for voltage regulation. These devices are composed of two coils wound around a shared magnetic core. The passage of current through one coil generates a magnetic field within the core, and as the current fluctuates, so does the magnetic field, thereby inducing a current in the second coil in response to the changing magnetic flux. The second coil has no direct connection with the primary coil making them independent and provide insulation. This insulation creates a barrier that protects the primary circuit from disturbances occurring on output wires of the transformer. The transformation of the input voltage, whether it is stepped up or down, depends on the ratio of turns between the coils. Given the typically high voltage output of TENG systems, step-down transformer circuits are often employed. Inductive transformers operate most efficiently at a specific internal frequency, which is generally higher than the frequency produced by contact-separation TENG devices. This makes them more suitable for use with rotary TENG systems, including lateral sliding and free-standing modes, which can more closely match the transformers' optimal frequency range [211]. Consequently, the selection of transformer circuits for power conversion in TENG systems should be made with consideration of their operational frequency to ensure optimal efficiency and compatibility.

Inductive transformers have been instrumental in addressing the high impedance characteristic of TENG systems. These transformers not only reduce the voltage and increase the current but also facilitate easier integration with electronic components due to their ability to lower TENG system impedance [212]. As mentioned, their application is particularly advantageous with rotating TENGs, which produce a high and stable frequency. A prime example of this is designed by Zhu et al. combining a rotating TENG with a power management circuit, composed of capacitors, a full-wave rectifier, and an inductive transformer, as shown in Fig. 22 **(a)** [213]. This assembly successfully generates a steady 5 V DC output, a common charging voltage for numerous devices, highlighting its practical application potential. Pu et al. found that efficiency of a power management circuit incorporating inductive transformers is significantly influenced by the coil ratio [214]. For a transformer with an n:1 coil ratio, the impedance, voltage, and current output of the system vary according to the value of n. This ratio plays a crucial role in determining the circuit's impedance, voltage, and current output. In the context of charging an ideal battery via a TENG, an equivalent circuit might consist of an n:1 inductive transformer coupled with a full-bridge rectifier, as illustrated in Fig. 22 **(b)**. The impedance of this charging circuit can be tailored through the coil ratio, providing optimal impedance matching between the TENG system and the battery. This adjustment is key to enhancing the power utilization efficiency of the system. As depicted in Fig. 22 **(c)**, an increase in the coil ratio not

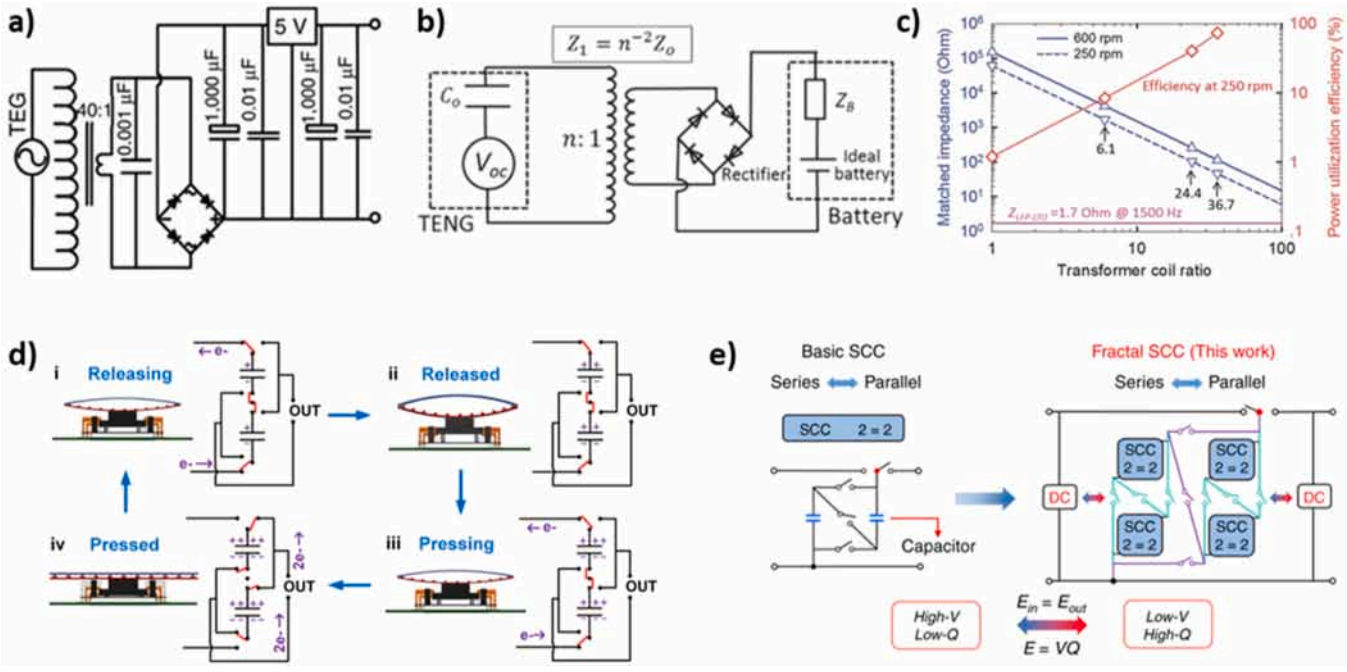

Fig. 22. Voltage regulation techniques for TENG systems using transformers. (a) Circuit diagram of a power management circuit with TENG, inductive transformer, rectifier and energy storage units. (b) Circuit diagram of a TENG charging ideal battery through inductive transformer and rectifier. (c) Effect of transformer coil ratio on matched impedance and power utilization efficiency of the TENG circuit. (d) Operational flow of a TENG system with capacitive transformer circuit. (e) Comparison of a fractal SCC and a basic SCC circuit diagram.
(a) Reproduce with permission from Ref. [213]. Copyright 2014, Nature Publishing Group. (b) and (c) Reproduce with permission from Ref. [214]. Copyright 2015, Wiley-VCH. (d) Reproduce with permission from Ref. [215]. Copyright 2014, IOP Science. (e) Reproduce with permission from Ref. [217]. Copyright 2020, Nature Publishing Group.

only improves power utilization efficiency but also decreases the matched impedance of the circuit, leading to enhanced overall performance. This relationship displays the critical importance of carefully selecting the coil ratio to ensure maximum efficiency in TENG systems that incorporate inductive transformers for energy conversion and battery charging applications [214].

3.2.2.2.2. Capacitive transformer. Capacitive transformers offer an alternative to inductive transformers, distinguished by their independence from frequency requirements. They employ a mechanism similar to voltage multiplying circuits, where voltage regulation is achieved by alternately connecting a set of capacitors in series during charging and in parallel during discharge [215]. This process allows for the regulation of voltage based on the number and capacitance of the capacitors involved. The operational principle of the capacitive transformer system is depicted in Fig. 22 **(d)**. In this setup, after the current generated by a TENG cycle is rectified, it is fed into the capacitive transformer circuit. During the TENG's pressing and releasing phases, the capacitors are connected in series while charging. Shown in Fig. 22 **(d- i–iii)** Upon contact, switches in the circuit are toggled to reconfigure the capacitors into a parallel arrangement and connect them to an external circuit depicted in Fig. 22 **(d-iv)**. This action enhances the charge transferred to the external circuit with each cycle. Transitioning from series to parallel configuration results in a quadrupling of the total capacitance, which in turn halves the voltage while doubling the charge supplied. Given that the capacitors are identical, they maintain equal voltage levels, which are half that of a single capacitor in series. When reconfigured into parallel, the voltage across each remains at this halved level. The voltage output of the transformer entirely depends on the capacitance and the number of capacitors included. Increasing the number of capacitors further decreases the voltage output increasing the charge. This method efficiently boosts the charge delivery per cycle without a corresponding increase in voltage, displaying a distinct advantage of capacitive transformers in power management and voltage regulation within TENG systems [215].

Capacitive transformers are uniquely versatile due to their lack of dependence on the frequency of the generated signal, making them applicable to a wide range of TENG systems. Zi et al. demonstrated this advantage by applying a capacitive transformer setup to a sliding freestanding mode TENG, successfully regulating voltage with high efficiency through adjustments to the system's total capacitance and obtaining energy transfer efficiency of 25 % [216]. The integration of a power management circuit with the freestanding TENG increases the supercapacitor's charging rate by a factor of five [216]. The capacitance values of the capacitors within the transformer circuit play a crucial role in determining both the voltage and charge output of the system. An increase in the capacitance of all capacitors within the circuit results in a proportional decrease in voltage, while simultaneously increasing the charge output.

Unlike traditional step-down inductive transformers, which reduce voltage while increasing current through magnetism, capacitive transformers achieve voltage reduction by increasing the system's charge capacity, independent of magnetic principles. Liu et al. found that this unique characteristic of capacitive transformers is amplified when configured into a fractal design based switched-capacitor converter (FSCC) [217]. A comparison between an FSCC and a basic switched-capacitor converter (SCC) setup is provided in Fig. 22 **(e)**, The

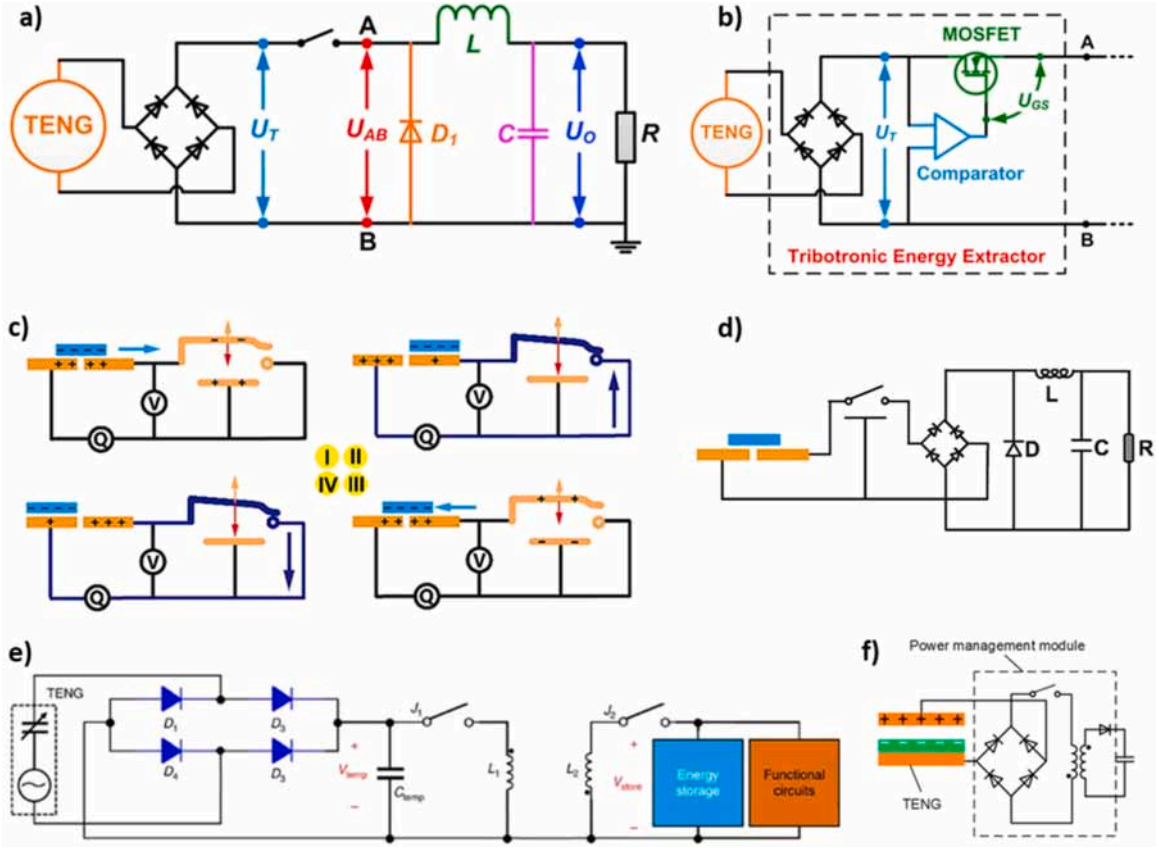

Fig. 23. Enhanced power management circuits using buck and flyback converters. (a) TENG circuit with a buck converter combined with a rectifier. (b) Circuit diagram of a triboelectric energy extractor. (c) Operational flow of autonomous cantilever switch. (d) Circuit diagram of a TENG system with autonomous cantilever switch, rectifier and buck converter circuit. (e) Schematic circuit diagram of a TENG power management circuit with a flyback converter. (f) Schematic circuit diagram of a TENG power management circuit like generic flyback converter.
(a) and (b) Reproduce with permission from Ref. [218]. Copyright 2017, Elsevier. (c) and (d) Reproduce with permission from Ref. [221]. Copyright 2024, Elsevier. (e) Reproduce with permission from Ref. [211]. Copyright 2015, Nature Publishing Group. (f) Reproduce with permission from Ref. [223]. Copyright 2017, Elsevier.

output characteristics of an FSCC can be significantly modified based on the connection type, or the order, in which the capacitors are arranged within the circuit. This provides a highly versatile approach to voltage regulation, allowing for adjustments to meet specific energy output requirements. The optimized transformer circuit for maximum energy efficiency managed to get an energy transfer efficiency of 94 % in constant mode and power density of 954 W m^{-2} surpassing a basic SCC by 67 times in pulsed mode [217]. These improvements signify the potential of capacitive transformers being used in power management circuits of low frequency TENGs offering a promising solution for improving the performance of TENG systems and other energy harvesting technologies.

3.2.2.2.3. Buck converter. Buck converters serve as a pivotal component in power management circuits, particularly for applications involving TENGs. Unlike inductive transformers that require AC to operate, buck converters are designed to work with DC, leveraging the inductive properties to store and release energy through a magnetic field. This characteristic makes them especially suitable for applications where a reduction in voltage while maintaining continuous current is needed, ensuring stable and efficient power conversion. The fundamental operation of a buck converter involves a cycle where an inductor stores energy in its magnetic field when DC flows through it. This energy is subsequently released to the load when the current is interrupted. This cycle is facilitated by a switch that toggles on and off, allowing the converter to adjust the voltage to a lower, desired level efficiently. Constant switching is crucial for the buck converter's operation, as it enables the storage and release of energy, maintaining a steady flow of current to the load.

In TENG applications, the integration of buck converters can be particularly effective due to their ability to exploit the CMEO conditions, thereby enhancing the energy generated per cycle. Various mechanisms can be employed to control the switching action, including direct control by the power supply, mechanical switches linked to the TENG's motion, or switches that operate automatically based on the potential difference generated by the TENG. Xi et al. designed a TENG power management circuit featuring a buck converter as illustrated in Fig. 23 **(a)** [218]. The switch in the circuit is autonomously controlled by the voltage output of the TENG. The switching mechanism also ensures the establishment of CMEO conditions, which amplifies the power output. When the switch is engaged, the TENG's generated energy is temporarily stored in both the inductor and a capacitor. This energy is then transferred to an external load when the switch is disengaged, facilitated by a diode D_1 that completes the circuit, allowing for a controlled release of energy. A key component in this system is the autonomous switch control mechanism, triboelectric energy extractor, depicted in the provided Fig. 23 **(b)** schematic. This control mechanism involves a comparator and a MOSFET as the switching element. The comparator's function is to continuously compare the voltage generated by the TENG with a preset reference voltage. This comparison dictates the state of the MOSFET and, consequently, the operational mode of the buck converter. When the TENG's voltage is below the reference level, the MOSFET remains off, preventing current flow and keeping the main circuit switch in the off position. This state corresponds to the energy accumulation phase. Conversely, once the TENG's output exceeds the reference voltage, the comparator triggers the MOSFET to turn on, allowing current flow and activating the switch in the main circuit. This transition initiates the energy release phase to the external load, effectively utilizing the generated energy. The triboelectric energy extractor manages to transfer 84.6 % of produced energy to external circuit. The autonomous control strategy ensures that the energy harvested by the TENG is optimally managed, allowing for the efficient conversion and utilization of the electrical output without the use of an external power supply. Xi et al. applied this power management circuit to a mechanical cycle with the frequency of 1 Hz, the matched impedance of the system is reduced from 35 MΩ to 1 MΩ with a slight decrease in average power retaining an 80.4 % efficiency. When compared to an unmanaged TENG charging capacitor of 1 mF, managed results improved by 128 times [218]. Additionally, Xi et al. modified the same circuit with the addition of a voltage stabilizer circuit using a second voltage-controlled switch and a Zener diode. This adjustment ensures that the output to the load is stable and within the desired specifications. The resulting circuit is used in a buoy system for blue energy harvesting, self-powered sensing, and transmission [219]. A notable advancement in self-powered systems including buck converter with automatic switch is the development of a self-powered smart bracelet done by Song et al. [220]. This innovative device integrates a free-standing TENG, a power management circuit with a buck converter, and double-sided micro-supercapacitors, all designed to harness biomechanical energy efficiently. The core of the bracelet's power management lies in its circuit, which comprises a full bridge rectifier, a buck converter, and a comparator. The comparator plays a crucial role, toggling the buck converter on and off in response to the voltage levels produced by the TENG. The electricity generated through this process is then harnessed to charge the bracelet's integrated micro-supercapacitors with 69.3 % energy transfer efficiency. These charged capacitors are then used as supply power to the device's electronics, ensuring a continuous energy source for its operation. This innovative self-powered bracelet design exhibits the potential of incorporating buck converters in wearable technology for the creation of self-sustaining devices with integrated energy storage solutions [220].

Moving beyond traditional electronic components for voltage regulation, it is also possible to implement an electrostatic force-derived mechanical switch activated by the TENG generated voltage. This technique is implemented with the strategic connection of a cantilever switch to the electrodes of a free-standing TENG by Zhou et al. [221]. The operation of the switch, toggling between its on and off states, is directly influenced by the potential difference observed across the TENG's electrodes throughout its operational cycle as depicted in Fig. 23 **(c)**. When the potential difference reaches a sufficient level, the resulting electrostatic force causes the cantilever to bend, completing the circuit. The design is made to prevent the risk of short circuits by ensuring the two terminals do not have direct contact. The electricity generated is then directed through a full bridge rectifier, followed by a buck converter circuit, before ultimately being delivered to an external load, as the full circuit illustrated in Fig. 23 **(d)**. This switch implemented power management strategy has demonstrated its effectiveness by significantly reducing the matched impedance from 60 MΩ to 470 kΩ. Simultaneously enhancing the average power output by a factor of 1.554 compared to a circuit without a switch. Overall circuit consisting of buck converter along with a switching mechanism increases average power output by 47.5 times compared to a circuit without any power management. This advancement demonstrates the potential of integrating mechanical switches powered by the TENG cycle in the efficient regulation and utilization of harvested energy [221].

Instead of employing an autonomous switch, integrating a mechanical switch into TENG systems for buck converting is also beneficial for certain applications. As the mechanical switches are tailored to the cycle itself, they provide significant potential in energy harvesting technology. Xiao et al. recently demonstrated an innovative method combining charge pumping and buck converter power management circuit. With this combination self-charge pumping circuits, which traditionally rely on switches, can now be efficiently synchronized with a buck converter using a single mechanical switch [222]. This synchronization enhances the overall system efficiency by successfully implementing both methods while simplifying the circuit design. Xiao et al. implemented this approach to a sliding TENG with a contact switch that concurrently manages a self-charge pumping circuit and a buck converter. When the electrodes are displaced, and the contact switch is off the capacitors are being charged in series. When the electrode's contact area gets to its maximum the internal capacitance of the TENG system reaches its maximum corresponding to maximum charge stored in the capacitors. Meanwhile, the contact switch is shorted, and configuration of the capacitors becomes parallel instantaneously due to diodes. Each capacitor

releases an equal amount of charge with some remaining stored and increases with each subsequent cycle. The power management circuit within this configuration employs a half-wave rectifier for effective AC to DC conversion, coupled with a storage capacitor for energy retention. This setup not only boosts the energy conversion process but also significantly improves the system's capacity for energy storage and utilization. Inclusion of the buck converter to charge pumping circuit increases the stored energy by 17.09 times. The integration of both buck converter and charge pumping circuit increases stored energy 848 times compared to a setup without power management. The combined circuit is able amplify the charge output per cycle by 40 times, achieving an energy transfer efficiency of over 88 % [222].

For a converter circuit option, it is also possible to utilize a flyback converter circuit, distinguished by their employment of coupled inductors rather than a singular inductor. Flyback converters operate similarly to step-down transformers, effectively reducing voltage while simultaneously increasing current, making them an attractive choice for TENG power management circuits. A defining feature of the flyback converter is its ability to isolate the input from the output thanks to the use of coupled inductors with independent terminals, enhancing the safety and applicability of the system. Niu et al. demonstrated an example of a TENG power management circuit incorporating a flyback converter as illustrated in Fig. 23 **(e)** [211]. In this configuration, the control of switches J1 and J2 is managed by logic control units, following a strategic operation pattern. Initially, both switches remain open, directing the focus solely on charging the temporary capacitor (CTemp). This phase continues until CTemp accumulates charge to a predetermined level, optimized for impedance matching within the circuit. Upon reaching this threshold, switch J1 is actuated, creating a pathway for current to flow from the capacitor to inductor L1. This action initiates the conversion of electrical energy into a magnetic field by L1, leading to a decrease in the capacitor's voltage. This decrease prompts the opening of switch J1 and the closure of switch J2. Given that J1 and J2 are coupled inductors sharing a magnetic core, the severance of the connection between J1 and the capacitor results in the dissipation of L1's magnetic field. This dissipation triggers a change in magnetic flux in inductor L2, thereby inducing current generation. The current produced through this process is then directed towards charging an energy storage device, ultimately serving to power external circuits. The resulting converter circuit has an energy transfer efficiency of 60 %- and 1096-times improved supercapacitor charging current. Another circuit utilizing flyback converter is designed by Cheng et al. for conversion of the low-frequency pulsed AC output from contact-separation TENGs into DC as provided in Fig. 23 **(f)** comprising a full bridge rectifier, a switch and coupled inductors [223]. Different from the previous circuit, the J2 switch is replaced by a diode similar to a generic flyback circuit. The control of the switch is once again done by a logic control unit dictated by the position of the TENG electrodes leveraging CMEO conditions. This method has significantly enhanced the energy output up to 2640 times for capacitors with increasing capacitance resulting in 72 % energy transfer efficiency. This innovative setup provides an effective solution for harnessing the energy from contact-separation TENGs, demonstrating a substantial improvement in energy conversion efficiency [223].

TENGs present a promising approach to sustainable energy harvesting, with significant progress made in enhancing their performance and efficiency. However, several challenges persist, limiting their full potential. A key issue is their inherently high impedance and low current

Table 2
Summary of various energy management strategies for TENGs [183,191,195,201,202,206,209,212,215,218,221].

	Method Strategy	Description	Improvement on Efficiency	Advantages	Disadvantages
Charge Boosting	CMEO	Short-circuiting at maximum and minimum displacement points to enhance energy output.	Increases instantaneous power at lower resistances	Enhances energy output and is compatible with low-impedance systems.	Requires precise mechanical switching for optimal results.
	External Charge Pump	Using external TENG systems to pump charges to the main TENG, enhancing charge density.	Increases surface charge density, boosts power output	Boosts charge density significantly; effective in enhancing power output.	Depends on additional TENG units; higher system complexity.
	Self-charge Pump	Using internal voltage multiplying circuits to enhance charge density autonomously.	Increases surface charge density, boosts power output	Autonomous operation; avoids external dependency for charge enhancement.	Limited by internal circuit components and air breakdown limits.
Current Regulation Circuits	Full Bridge Rectifier	AC to DC conversion using four diodes, ensuring both forward and reverse currents contribute to DC output.	Enhanced DC conversion but limited by diode voltage drop	Ensures both current directions contribute to DC; simple and robust.	Voltage drop across diodes; efficiency loss in high-frequency systems.
	Half Bridge Rectifier	AC to DC conversion using two diodes, utilizing only half of the wave but with higher efficiency per cycle.	Surpassed full-wave rectifier efficiency by maintaining charge density during half of the cycle	Higher efficiency per cycle; simpler design than full-wave rectifier.	Utilizes only half the wave; limited to specific applications.
	Bennet's Doubler Rectifier	Incorporating two capacitors for exponential voltage doubling over time.	Exponentially increases energy output with each cycle surpassing full and half wave rectification	Exponential increase in voltage output; ideal for long-term use.	Takes time to achieve optimal efficiency; initial low performance.
	DC-TENG	Direct DC output generation using air breakdown between electrode and triboelectric layer.	Directly generates DC output without the need for rectification, eliminating diode losses and achieving enhanced efficiency.	Simplifies circuit design by eliminating rectifiers; reduces energy loss associated with AC-DC conversion.	Dependent on air breakdown conditions; limits system design.
Voltage Regulation Circuits	Inductive Transformer	Step-down voltage while increasing current for stable energy delivery, optimal for high-frequency systems.	Reduces voltage and matched impedance while increasing current	Provides stable output voltage; reduces TENG impedance effectively.	Dependent on optimal coil ratios; best suited for high-frequency TENGs.
	Capacitive Transformer	Voltage regulation by alternating capacitors between series and parallel configurations.	Reduces voltage while increasing transferred charge	Versatile application across TENG modes; no frequency dependence.	Needs careful capacitor selection; complex circuit design.
	Electronic Switch Buck Converting	Electrically activated switches are triggered by potential differences or system voltage for seamless energy regulation.	Improves average power output	Automates energy regulation; improves system compatibility.	Sensitive to voltage fluctuations; requires precise control mechanisms.
	Mechanical Switch Buck Converting	Manually or electrostatically activated switches tailored to TENG cycles for energy optimization.	Improves average power output	Tailored to TENG cycles; no additional power source required.	Potential mechanical wear; requires accurate synchronization.

output, which restricts compatibility with conventional electronic devices. To mitigate these limitations, the development of effective energy management strategies is crucial. Table 2 provides a comprehensive overview of current energy management strategies for TENG systems, summarizing their improvements, advantages, and drawbacks in addressing these challenges. For example, buck converters efficiently reduce post-rectification voltage, enhancing compatibility with low-impedance devices. Charge pumping significantly increases charge density by overcoming environmental dielectric breakdown constraints. Inductive and capacitive transformers optimize voltage regulation and impedance matching for high- and low-frequency systems, respectively. Additionally, rectifiers play a fundamental role in converting AC outputs into usable DC. Collectively, these strategies form a robust framework for overcoming TENG limitations, enhancing their practicality across diverse applications.

4. Applications of TENGs

TENGs have high potential for many application areas because they have different operating modes that can operate efficiently at low frequency and can be developed with a wide range of materials. For this reason, it has been used in a wide range of applications in the literature. In order to make the review easy to follow, these applications have been grouped under two main headings: energy harvesting and self-powered sensors. Energy harvesting applications focus on converting mechanical energy into electrical energy. On the other hand, TENGs are also used as self-powered sensors that can operate without using an external energy source except mechanical energy. The sources of energy harvested for both purposes are basically the same and are generally wave, wind and biomechanical energies. In the following sections, current examples of these application areas are explained and discussed.

4.1. Energy harvesting

4.1.1. Blue energy

The marine environment is one of the most substantial application areas for TENGs toward energy harvesting. 70 % of the Earth's surface is covered by water. The great potential of water waves for free motion makes the marine environment a major candidate for blue energy harvesting by TENGs [224]. Most advantageously, there are virtually no

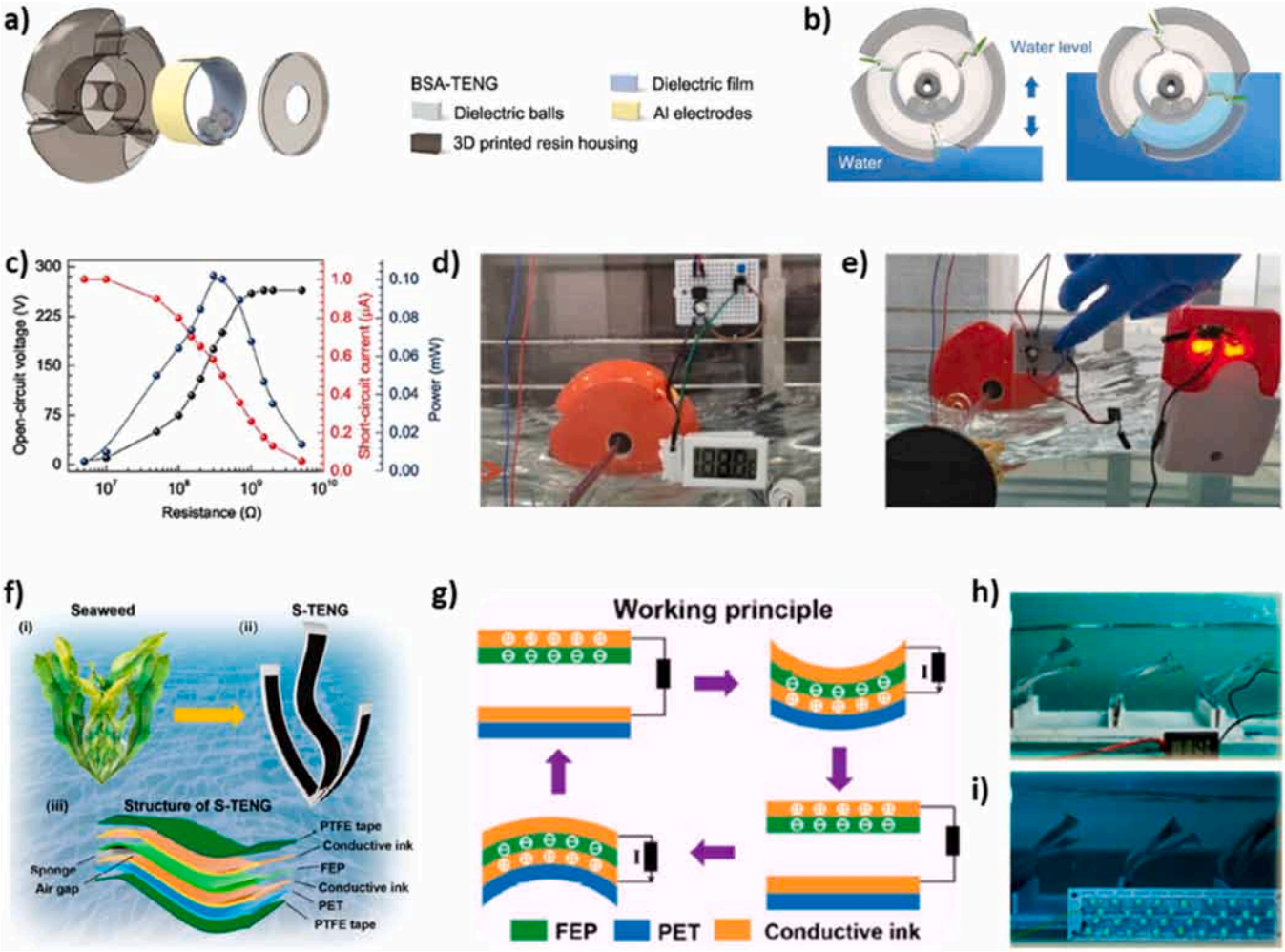

Fig. 24. TENGs for energy harvesting from water waves. (a) The exploded view of the barycenter self-adapting triboelectric nanogenerator (BSA-TENG). (b) Representation of the unidirectional rotation of the BSA-TENG system embedded in a housing under fluctuating water waves. (c) Open circuit voltage (Voc), short circuit current (Isc) and peak power demonstrations against resistance graph of the BSA-TENG. Demonstration of the BSA-TENG powering (d) a temperature sensor and (e) wireless transmitter. (f) Schematic representation of the design of the seaweed-like triboelectric nanogenerator (S-TENG), comprising conductive ink-coated fluorinated ethylene propylene (FEP), polyethylene terephthalate (PET), and polytetrafluoroethylene (PTFE) layers for protection against water contact. (g) Demonstration of the contact electrification process between FEP and PET films in the S-TENG under wave excitations. (h) Utilization of the S-TENG to charge a 100 μF capacitor and power a thermometer. (i) Demonstration of the S-TENG lighting up 30 LEDs.
(a)–(e) Reproduce with permission from Ref. [231]. Copyright 2022, Wiley-VCH. (f)–(i) Reproduce with permission from Ref. [232]. Copyright 2021, American Chemical Society.

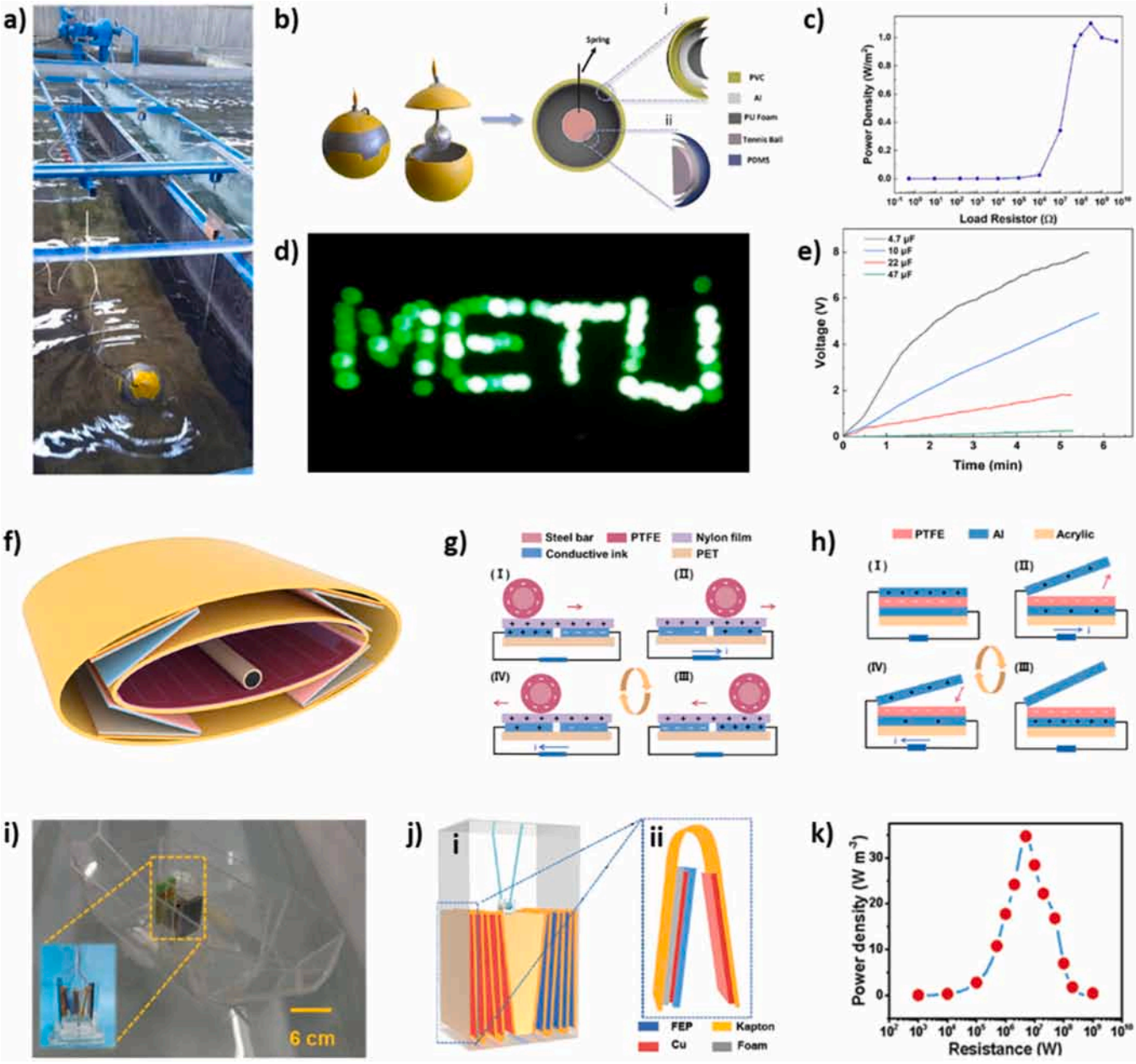

Fig. 25. TENGs for energy harvesting from water waves. (a) Real image of MBB-TENG tested in a wave basin under simulated wave conditions, (b) schematic representation of the structure of MBB-TENG and (c) the calculated power density of the MBB-TENG against different load resistors. (d) 86 serially connected LEDs arranged in "METU" letters and (e) charged conventional capacitors for the demonstration of the energy harvesting ability of MBB-TENG. (f) Design of the elliptical cylindrical triboelectric nanogenerator (EC-TENG) featuring an internal elliptical unit and four externally located triboelectric units. (g) Representation of the contact electrification process of the internal elliptical unit in the EC-TENG, and (h) representation of the contact electrification process of the external triboelectric units in the EC-TENG. (i) Schematic representation of the bifilar-pendulum-assisted multilayer-structured triboelectric nanogenerator (BM-TENG). (j) General structure of the (i) pendulum-based TENG unit, and the (ii) representation of a single unit in BM-TENG (k) Peak power density against resistance graph achieved by the BM-TENG. (a)–(e) Reproduce with permission from Ref. [229]. Copyright 2023, Elsevier. (f)–(h) Reproduce with permission from Ref. [233]. Copyright 2022, Springer Nature. (f)–(h) Reproduce with permission from Ref. [234]. Copyright 2018, Wiley-VCH.

constraints for TENGs to operate from a design standpoint as long as contact electrification is met. In the literature this freedom appears as a wide range of prototype designs. Among the studies, the most proposed TENG devices are the ones floating on water [225–228]. Other than these, integration of TENG mechanism into systems that are already in use in marine environment is another commonly used method in blue energy harvesting applications [229,230]. Unlike the trend Yang et al. suggested a barycenter self-adapting triboelectric nanogenerator (BSA-TENG) where the vibrational water wave high entropy energy is converted first into mechanical energy, and then into electric energy. BSA-TENG consists of dielectric balls inside of a dielectric chamber where the charge collecting electrodes are attached in two half circles as represented in Fig. 24 **(a)**. The whole system is then embedded into a housing which unidirectionally rotates under fluctuating water as shown in Fig. 24 **(b)**. For BSA-TENG the peak power of 0.1 mW was reported, and a self-powered temperature sensor and wireless transmitter were also shown to be powered up as given in Fig. 24 **(c)–(e)** [231]. In another study Wang et al. proposed the seaweed-like triboelectric nanogenerator (S-TENG) for blue energy harvesting. The S-TENG consists of layers of conductive ink-coated fluorinated ethylene

propylene (FEP), a conductive ink-coated polyethylene terephthalate (PET) sealed between two PTFE membranes to protect from water contact as provided in Fig. 24 **(f)**. The triboelectrification is provided by the contact electrification between FEP and PET films under the wave excitations as represented in Fig. 24 **(g)**. The S-TENG was reported to be able to charge a 100 μF capacitor to 3 V in 100 s, to power a thermometer, and light up 30 LEDs, as shown in Fig. 24 **(h)** and **(i)** [232].

In a different study Demircioglu et al. proposed a modified buoy-based TENG (MBB-TENG) [229]. The real image of the MBB-TENG tested in a wave basin under simulated wave conditions is provided in Fig. 25 **(a)**. The MBB-TENG is converted from a commercial spherical buoy by a coating of polyurethane (PU) foam on its inner surface as represented in Fig. 25 **(b-i)**. The counter triboelectric material of polydimethylsiloxane (PDMS) coated onto a tennis ball (Fig. 25 **(b-ii)**) attached to a spring is affixed at the top of the buoy as it swings inside. The schematic representation of the MBB-TENG is shown in Fig. 25. The triboelectrification is provided by the contact-separation process occurring between PU foam and PDMS layers as MBB-TENG encounters with the waves. The calculated power density output is reported as 1.1 W/m^2 when a load resistor of 300 MΩ is connected to the circuit as provided in Fig. 25 **(c)**. For the demonstration of the energy harvesting ability of the MBB-TENG, 86 serially connected LEDs arranged in "METU" letters are lit and conventional capacitors are charged for around 5.5 mins as represented in Fig. 25 **(d)** and **(e)**. For the energy

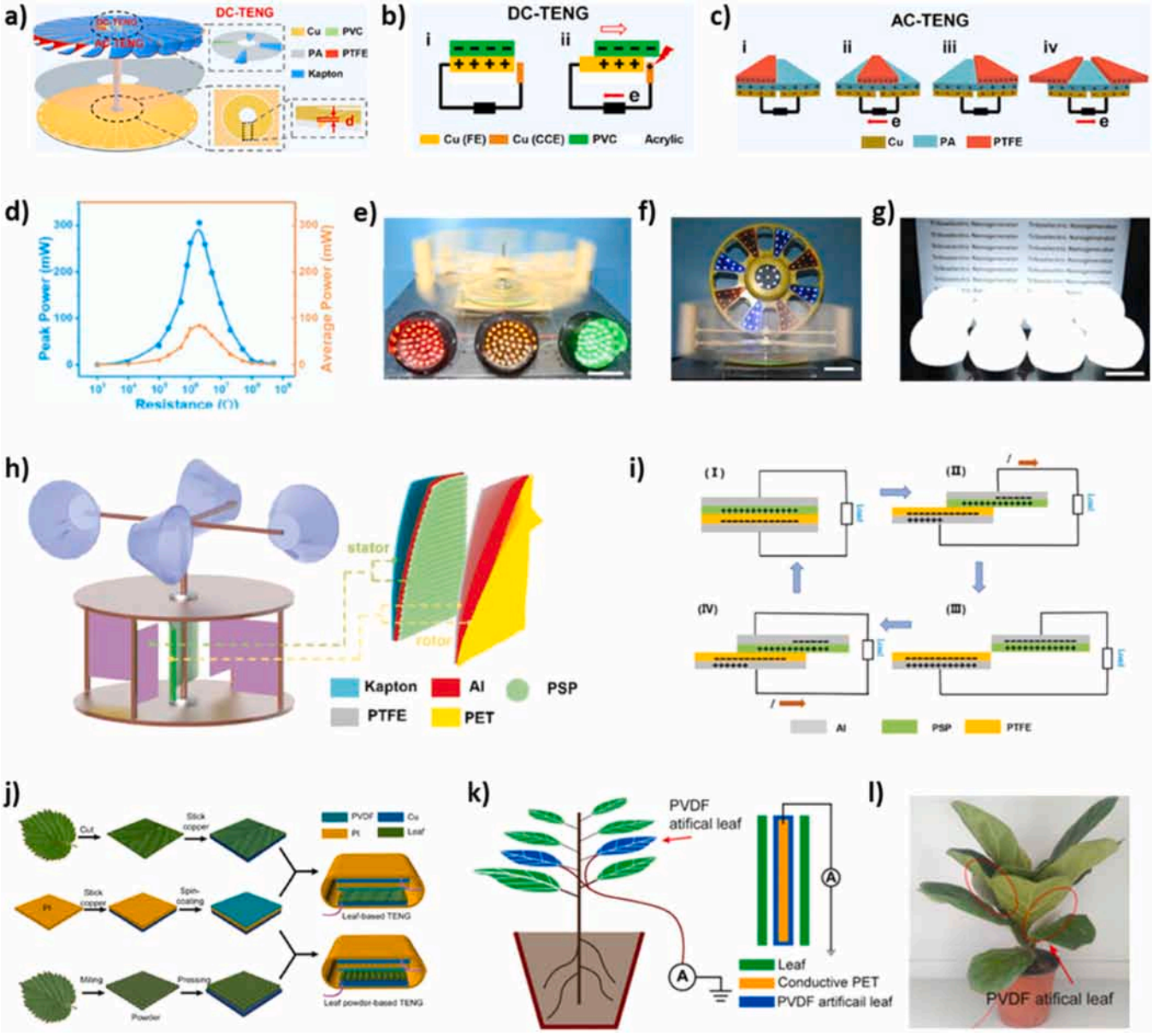

Fig. 26. TENGs for energy harvesting from wind. (a) Schematic representation of the high-performance dual-mode TENG, (b) representation of the charging mechanism of the direct-current (DC) TENG segment, (c) representation of the charging mechanism of the alternating current (AC) TENG segment of the high-performance dual mode TENG, and (d) peak and average power outputs of the AC-TENG segment. Demonstration of the high-performance dual-mode TENG powering (e) traffic lights, (f) warning lights, and (g) commercial LED bulbs. (h) Schematic representation of the peanut shell powder triboelectric nanogenerator (PSP-TENG), (i) representation of the working mechanism of the PSP-TENG utilizing peanut shell powder (PSP), PTFE, and rotational movement for contact electrification. (j) Schematic representation of the leaf-based triboelectric nanogenerator with both fresh and powdered forms used, (k) device structure of the leaf-based TENG (l) real image of leaf-based TENGs as a real-case application.
(a)–(g) Reproduce with permission from Ref. [241]. Copyright 2020, American Chemical Society. (h) and (i) Reproduce with permission from Ref. [242]. Copyright 2018, Wiley-VCH. (j)–(l) Reproduce with permission from Ref. [243]. Copyright 2019, Elsevier.

generation under the harsh oscillations of rough seas the elliptical cylindrical triboelectric nanogenerator (EC-TENG) with a symmetrical design is suggested by Tan et al. as shown in Fig. 25 **(f)**. EC-TENG is designed in two parts. The first part is the internal elliptical unit which utilizes the oscillation of a PTFE coated steel bar against nylon coated conductive ink electrode. Contact electrification sequence of the internal part is represented in Fig. 25 **(g)**. The second part is the externally located four triboelectric units which are operated by the stimulations coming from the internal unit. For the external TENG units PTFE is used as a dielectric layer against aluminum (Al) electrodes. Contact electrification process of the external part is shown in Fig. 25 **(h)**. The whole unit is enclosed in an elliptical PLA cover. The EC-TENG is reported to generate an optimal output power of 12 mW. Additionally, the system successfully powered 400 green LEDs connected in series [233]. To benefit from the free motion of the units floating on water, Zhang et al. proposed the bifilar-pendulum-assisted multilayer-structured triboelectric nanogenerator (BM-TENG) as shown in Fig. 25 **(i)**. The TENG in pendulum structure is composed of FEP as dielectric material against Cu electrode as shown in Fig. 25 **(j-i)** and **(j-ii)**. Contact electrification is achieved through a pendulum mechanism by the seesaw-like motion of the vessel on its encounter with water waves. The peak power density of the BM-TENG is reported to be 34.7 W m^{-3} as provided in Fig. 25 **(k)** [234].

With increasing awareness of the ease of construction and implementation of TENGs for many applications, the use of them is also focused more on blue energy harvesting. However, the dielectric

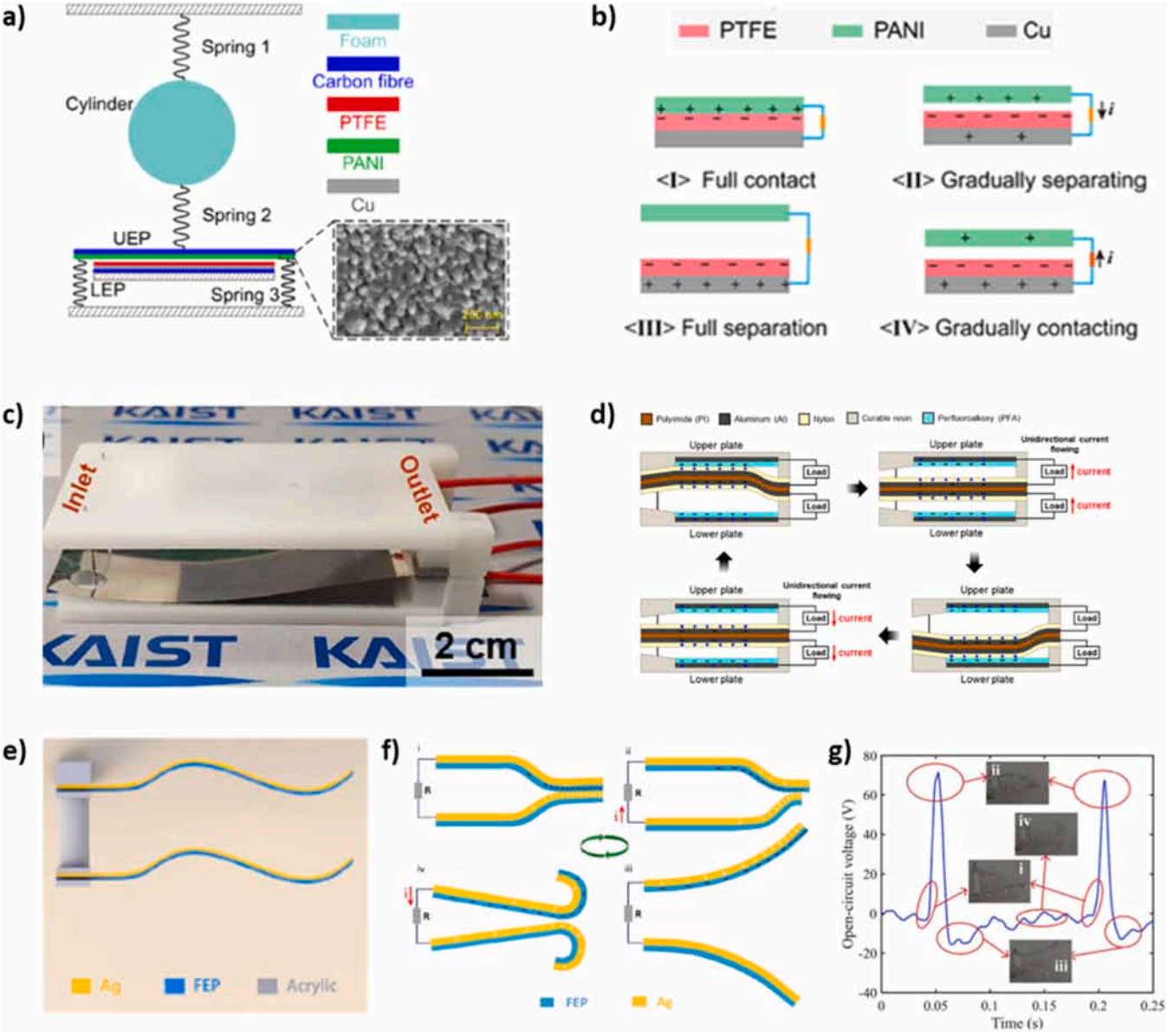

Fig. 27. TENGs for energy harvesting from wind. (a) Configuration of the vortex-induced vibration triboelectric nanogenerator (VIV-TENG), employing cylindrical foam and springs to harness wind-induced oscillation. (b) Illustration of the triboelectrification process in the VIV-TENG as the cylindrical foam interacts with wind-induced oscillation. (c) Schematic representation of the rear-fixed film triboelectric nanogenerator (RFW-TENG) utilizing fluttering mechanism. (d) Representation of the contact electrification process in the RFW-TENG facilitated by the fluttering motion. (e) Design of the fluttering double-flag type triboelectric nanogenerator (FD-TENG) (f) Illustration of the contact-separation mode operation in the FD-TENG driven by continuous fluttering of the triboelectric surfaces. (g) Peak positions of open circuit voltage at different stages of the FD-TENG operation.
(a) and (b) Reproduce with permission from Ref. [244]. Copyright 2022, Elsevier. (c)–(d) Reproduce with permission from Ref. [245]. Copyright 2022, Elsevier. (e)–(g) Reproduce with permission from Ref. [246]. Copyright 2020, Elsevier.

materials used in such applications are mostly polymers, which often lack strong resistance to environments with high humidity and fluctuating ambient temperatures. Although stability has been demonstrated in most studies, the materials are not well-suited for long-term use. Nevertheless, the necessitation of infrastructural basis, complex operational mechanisms and challenges regarding the maintenance of conventional wave energy converters (WECs) makes the utilization of TENG devices appropriate candidates for energy harvesters [235,236]. On the other hand, the power generated is a prominent measure for an energy harvesting device. However, there is not a certain consensus on this topic in literature for TENGs. The reported power density units can vary across different studies. For a mechanism heavily influenced by surface area, reporting power density as the power obtained per unit surface area would make the results more comparable within the community.

4.1.2. Wind energy

Wind is another highly abundant source of waste motion for TENGs to harvest and convert into electricity For most of the studies, TENG devices for wind energy harvesting are built based on rotating mechanisms. There are two frequently used methods in most wind energy harvesting applications for contact electrification. These are simply based on either direct contact of the dielectric materials with each other by coating them onto current collector electrodes or a flap configuration for sequential contact and separation motions [237–240]. Correlatively, He et al. proposed a high-performance dual-mode TENG based on a rotational structure as shown in Fig. 26 **(a)**. The dual mode TENG allows the output in both DC and AC signals at the same time owing to the coaxially placed DC and AC TENG units. For the DC-TENG part, polyvinyl chloride (PVC) is used against a frictional electrode of Cu in the inner circle. However, to obtain DC output, another charge-collecting electrode of Cu is used, and electrostatic breakdown is assisted for DC output as provided Fig. 26 **(b)**. DC-TENG is utilized mostly for sensing operations of wind speed. For the AC-TENG part of the dual-mode TENG, PTFE and nylon (PA) are used as counter dielectric materials in a conventional flap configuration, and Cu is preferred as current collector electrode in the outer circle as represented in Fig. 26 **(c)**. The AC-TENG is designed to operate for energy harvesting applications, and it was reported that it was able to generate 300 mW of peak and 85 mW of average power outputs, respectively as shown in Fig. 26 **(d)**, without any circuit management systems. Additionally, it was proved that high-performance dual-mode TENG can power up traffic lights, warning lights and eight commercial LED bulbs as shown in Fig. 26 **(e)**–**(g)** [241]. In another study Zhang et al. proposed a peanut shell powder triboelectric nanogenerator (PSP-TENG) with a similar rotational design as provided in Fig. 26 **(h)**. As counter dielectric materials PSP and PTFE are used in a flap configuration, and the contact electrification is met by the sequential contact and separation of the dielectric materials by their rotational movement as represented in Fig. 26 **(i).** The use of PSP is justified by its high specific surface area and strong surface charge properties. The maximum output power density of PSP-TENG is reported as 365 mWm^{-2}, and 228 commercial LEDs are shown to be lit [242]. Similarly, being influenced by nature, Feng et al. suggested a leaf based TENG for wind energy harvesting. The schematic representation of leaf based TENG, working based on simple contact separation mode, is provided in Fig. 26 **(j)**. Leaves in different forms against polyvinylidene fluoride (PVDF) are preferred as dielectric materials with Cu as current collector electrodes. For the leaf based TENG, fresh, dry, powder and Poly-L-Lysine (PLL) modified powder leaves are used. The maximum electrical outputs are obtained from leaf-powder-PLL TENG (LP-PLL-TENG) because of its increased surface area, and the removal of the water in the leaves. A sketch and a photo of leaf based TENG device are provided in Fig. 26 **(k)** and **(l)**, respectively. The maximum power output of leaf based TENG is reported as 17.9 mW, and 868 LEDs are shown to be lit [243].

For the energy harvesting of low-speed winds Zhang et al. proposed the vortex-induced vibration triboelectric nanogenerator (VIV-TENG). In this configuration, a cylindrical foam is connected to a contact separation mode TENG by springs, as shown in Fig. 27 **(a)**. Polyaniline (PANI) and PTFE are used as the dielectric materials. As cylindrical foam encounters wind, the oscillation caused by it drives the contact separation TENG to work, thus the triboelectrification is fulfilled as shown in Fig. 27 **(b)**. By placing two VIV-TENGs in tandem (T-VIV-TENG), more than 90 serially connected LEDs are reported to be lit under a wind velocity of 3 m/s [244]. From a different point of view Tcho et al. suggested a rear-fixed film triboelectric nanogenerator (RFW-TENG). Based on a fluttering mechanism the dielectric materials of perfluoroalkoxyl (PFA) and nylon are placed between a resin plate as shown in Fig. 27 **(c)**. Contact electrification is met by the fluttering of one-end-fixed nylon coated Al electrode against PFA as provided in Fig. 27 **(d)**. The maximum average power of 77 μW was reported for RFW-TENG at a wind velocity of 4 m/s. Additionally, serially connected 30 LEDs are reported to be lit [245]. In another study benefiting from fluttering mechanism Sun et al. proposed the fluttering double-flag type triboelectric nanogenerator (FD-TENG) as shown in Fig. 27 **(e)**. The FD-TENG is composed of two triboelectric surfaces located in parallel to each other. FEP is used as one of the triboelectric materials and Ag as both counter triboelectric material and current collector electrode. The contact electrification is caused by the continuous fluttering of the triboelectric surfaces by the incident wind based on contact-separation mode as shown in Fig. 27 **(f)**. The peak positions of open circuit voltage at different stages of FD-TENG are also shown in Fig. 27 **(g)**. It is reported that the FD-TENG can reach up to 600 mW m^{-2} peak-to-peak power density, and it is shown that serially connected 205 green LEDs can be lit [246].

Wind energy harvesting with TENGs is another promising method that utilizes environmental stimuli, alongside blue energy harvesting. Especially, the ability of TENG devices to convert waste mechanical energy into electricity provides important fields to utilize such as energy harvesting and sensor applications. Additionally, easy to build designs and simple manufacturing and maintenance of such devices makes them potential candidates for daily applications. However, similar to blue energy harvesting, the environmental resistance of the materials used remains a challenge that must be addressed for wind energy applications. Additionally, severe frictional damage to the dielectric materials, often resulting from rotational units, can degrade device performance over time. These critical factors must be carefully considered in studies on wind energy harvesting.

4.1.3. Biomechanical energy

Integrating TENGs into everyday motion of humans can bring about several Watts of wasted power back into usefulness. For instance, an average man weighing 80 kg generates 66.8 W power from the motion of the knees, while 2–20 W can be gained by heel striking in every two steps during walking [247]. Therefore, TENGs are portrayed as a strong tool to harvest the energy released from biomechanical actions. Several, simple yet effective ways to incorporate TENGs into daily life have been reported in smart textiles [143,248–251], shoes [252–256], and some handheld/wearable devices [257–262].

A 3D double electrode TENG is developed by Li et al. using an Ag-cotton yarn conductive core coated with PDMS or TPU [248]. TENG layout is provided in Fig. 28 **(a)**. The two triboelectric materials served as the electrodes, and various knitting styles are investigated. The crisscross knitted structure provided better outputs and hence is chosen to be the most suitable. For the output performance of the TENG, at 6 Hz frequency, the peak output values are 76 V and 3 μA, while the maximum power density reached 200.93 mW m^{-2} at a resistance of 80 MΩ. The fabric remained stable under 50,000 cycles. Output performance on a sweaty arm is decreased to an extent but is regained upon evaporation of the sweat. Gentle hand tapping powered 100 series-connected LEDs. Additionally, a calculator and a watch are powered by the TENG. A human motion monitoring system is integrated with the TENG, enabling Bluetooth signals to monitor movements of the

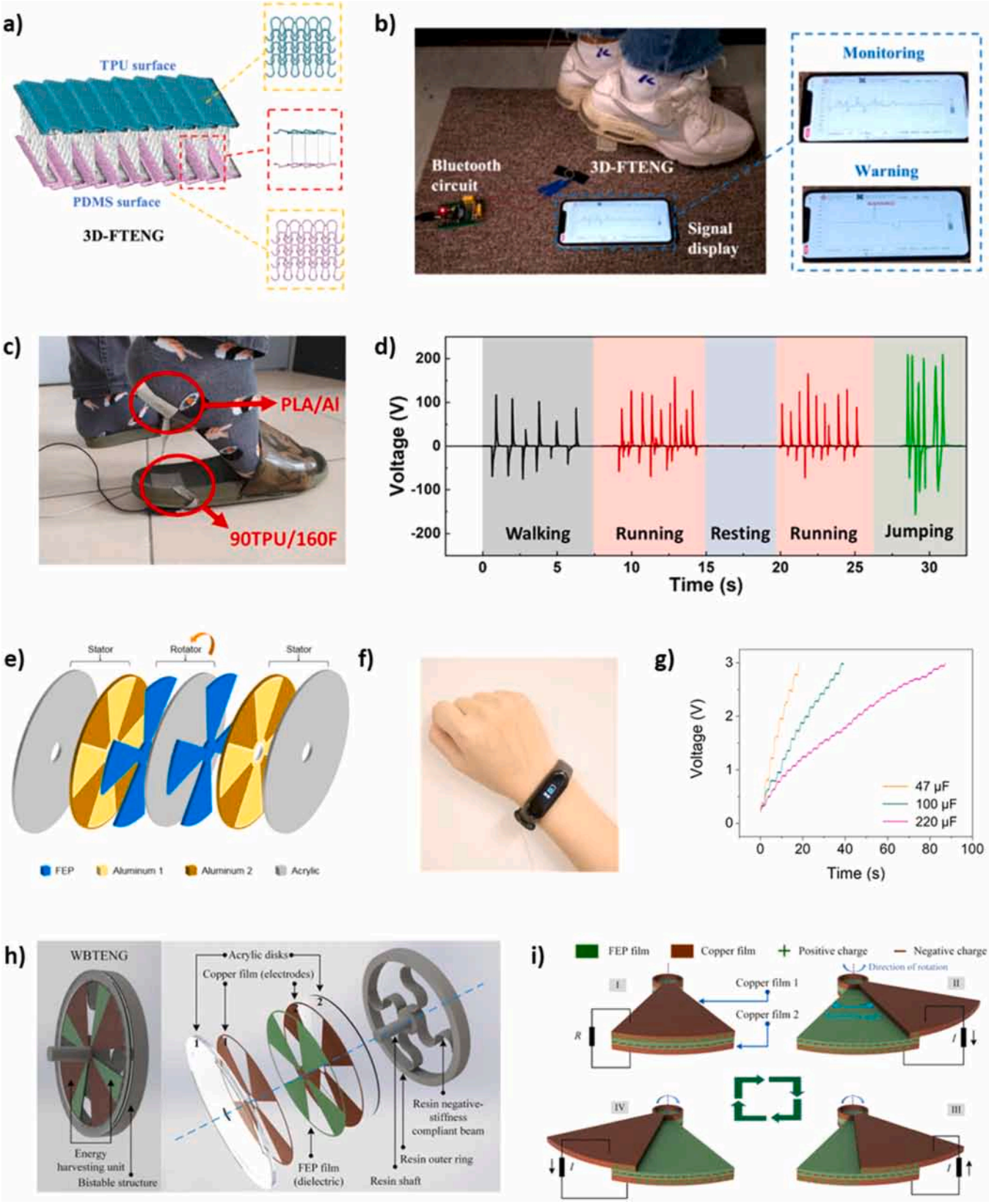

Fig. 28. Wearable and portable TENGs for biomechanical energy harvesting. (a) A schematic of the Ag-cotton yarn core/TPU and PDMS shell energy harvester and (b) its application as a human motion monitoring system. (c) The measurement setup of TPU/Ag NW TENG and (d) its capability of analyzing walking, running, resting and jumping. (e) A drawing of the handheld whirligig TENG, (f) its performance in charging a smart watch and (g) its capability of charging various capacitors rapidly. (h) The setup of the bistable TENG generating power from human elbow motion and (i) its working mechanism.
(a) and (b) Reproduce with permission from Ref. [248]. Copyright 2022, Elsevier. (c) and (d) Reproduce with permission from Ref. [143]. Copyright 2021, Elsevier. (e)–(g) Reproduce. Copyright 2021, Elsevier. (h) and (i) Reproduce with permission from Ref. [258]. Copyright 2023, Elsevier.

elbow, finger, waist, and heel, as shown in Fig. 28 **(b)**.

Electrospun fibers are utilized in the work of Xia et al., where PVDF/PMMA blend films are used to fabricate durable TENG devices [249]. The two polymers are blended and electrospun onto Al films adhered to PET. As a counter electrode, glass fiber fabric is attached to the same Al-PET substrate. Contact separation between the two allowed for a high-performance TENG to be fabricated. The open circuit voltage is observed to be 810 V and the short circuit current is 70 μA. The instantaneous peak power density is reported as 13.8 W/m^2 with a load resistance of 5 MΩ. The device shows mechanical stability for over 10,000 cycles, with little change in performance and microstructure. The TENG is used in zebra crossing lighting, instantly notifying pedestrians if they attempt to cross during a red light.

In another study Yun et al. proposed a bidirectional gearbox for harvesting stepping motion via an external device connected to the shoe [252]. The bidirectional gearbox consisted of two gearboxes and a lever. The contact layer made from Al is connected to the rotor whereas flexible FEP films formed the stator. A one-way clutch design allows only one-directional rotation movement to occur. Therefore, when the lever is compressed and released, the rotor spins only in one way. Through a single stepping motion, the specific power generated by the TENG is reported as 13 μW/g along with 600 V open-circuit voltage and 20 μA short-circuit current. A single step can power 300 LEDs, and the device can also charge a smartwatch.

Doganay et al. displayed the importance of durability in wearable TENG technologies in their work [143]. Silver nanowire (Ag NW) modified fabrics are laminated with thermoplastic polyurethane (TPU) layers as the dielectric component, forming the TENG electrode by simple solution-based means. The electrodes are found to be stable after 15 washing cycles, persistently showing high electrical output. An output voltage of − 162 V, short-circuit current of − 42 μA, and a maximum power output of 1.25 W/m^2 is obtained when used in conjunction with a PLA/Al foil counter electrode. 185 serially connected LEDs, and a chronometer could be charged up using this power output. Utilizing this setup, gait analysis of a person is done, as shown in Fig. 28 **(c)**. The output of the device, given in Fig. 28 **(d)**, clearly shows when a person is walking, running, resting and jumping. Finally, a self-powered wristband is developed for IoT applications, which is used to control basic computer applications.

A handheld whirligig-inspired TENG is designed by Zou et al, the schematic of which can be seen in Fig. 28 **(e)** [257]. The winding and unwinding of a closed-loop string passing through the parts allowed for speeds as high as 10,000 rpm to be reached upon pulling 300 mm. Subsequently, the movement of the FEP rotor part between the Al electrode stators generated power. Fig. 28 **(f).** The maximum power density is measured to be 0.85 W/m^2 and the TENG could charge a commercial 220 μF capacitor from 0 to 3 V in about 80 s, as shown in Fig. 28 **(g)**.

Exploiting the elbow motion, Tan et al., proposed an externally attached system consisting of Cu tape electrodes and a thin FEP film [258]. Acrylic disks and a shaft, an outer ring, and 4 beams made from resin completed and held the structure, as displayed in Fig. 28 **(h)**. The working mechanism of the device is shown in Fig. 28 **(i)**. The bistable TENG allowed harvesting low-frequency torsional vibration from human motion. The output voltage values ranged from 40 V to 220 V depending on the amplitude of the elbow motion. For maximum power output, 3.39 mW at a load resistance of 90 MΩ could be achieved with the system. Minimal performance loss is observed after 14,400 cycles. As a portable energy source, the device can power 100 LEDs and a temperature sensor.

Wearability of the energy harvesting units is of utmost importance. Among other wearable energy harvesters, while it is possible to achieve quite high-power densities utilizing EMGs, their weight poses challenges for researchers and end users [263]. The weight of TENGs and PEGs are substantially lower, with wearable photovoltaics following close by. While efficient and powerful, wearable photovoltaics still need some significant issues to be addressed such as: flexibility, washability, toxicity and safety, and wearing comfort [264,265]. The storage of the produced energy also brings about a need for integrated mobile batteries that must be thin and flexible as well. Even then, wearable photovoltaics do not harvest any excess energy arising from human motion. TENGs work as energy scavengers, and harvesting this energy makes them strong in their area.

Biomechanical energy harvesting is a broad field with numerous design approaches. While some devices generate significant power, many lack practicality. For functional use, an energy-harvesting device must also be comfortable to wear. However, these devices often feature bulky structures, making them uncomfortable for prolonged use. It is an area of concern to make these devices more appealing in this regard. Another challenge is the stability of these devices during extended use. Clothing items like shoes or shirts may be worn for over 10 h, often exposed to high humidity and sweat. Additionally, changes in output performance after washing the items present another concern. Understanding how the device performs under prolonged use, including cyclic loading and exposure to sweat or humid environments, is essential. With the growth of Internet of Things (IoT), these devices could potentially enable fully self-powered sensors for monitoring gait, pulse, and respiration in the future.

4.2. *Self-powered sensors*

In addition to the excessive use of triboelectrification in energy harvesting, they have been used for various sensing applications including, acoustic sensing, vibration monitoring, pressure sensing, and so on. The electrical signal generated after pressing or sliding is also used for sensing applications. Their passive sensing nature and rapid electrical signal generation following physical contact make them highly promising candidates for next-generation sensors. In that point of view, triboelectric sensors have been reviewed extensively [9]. In this part of the review, we mainly focus on the recent advances in the TENG-based tactile sensors and their applicability on the field of human-machine interfacing (HMI) and the healthcare.

4.2.1. *Tactile perception*

One of the most important sensory functions of the human is the tactile perception of the surrounding environment. This tactile perception is originated from the different subcutaneous sensory nerve ends. Addition to the sensory information comes from these nerve ends, to recognize the texture, roughness and the object itself requires an analysis of these signals by brain. On this basis, combination of the electromagnetic signal generated from the TENG based tactile sensors and the machine learning algorithms, might be an important tool for robotic systems to get closer for obtaining human-like tactile perception. Especially differentiating different materials just by touching with a very simple structure might be the game changer for next generation robotic perception [266–275].

One of the first object recognition example for triboelectric sensors is demonstrated by Zhao et al. [267]. In this work, a washable and breathable smart glove composed of textile based triboelectric sensors for grip posture detection of different objects is demonstrated. Cu-PAN and parylene-Cu-PAN yarns are stitched on five different positions of the glove. When a pressure applied on a triboelectric sensor node, different voltage signals are generated due to change in the contact area. Posture detections are carried out on different objects including a pen, an egg, and a dumbbell and different voltage signals are recorded from each object as demonstrated in Fig. 29 **(a)**. This demonstration proves that triboelectric-based sensors can be effectively used for object recognition applications.

A more complicated object recognition application is demonstrated by the Jin et al. [268]. The authors reported a soft-robotic gripper system based on triboelectric sensors. The triboelectric sensors are monitoring the tactile information for the soft-robotic gripper. Two different

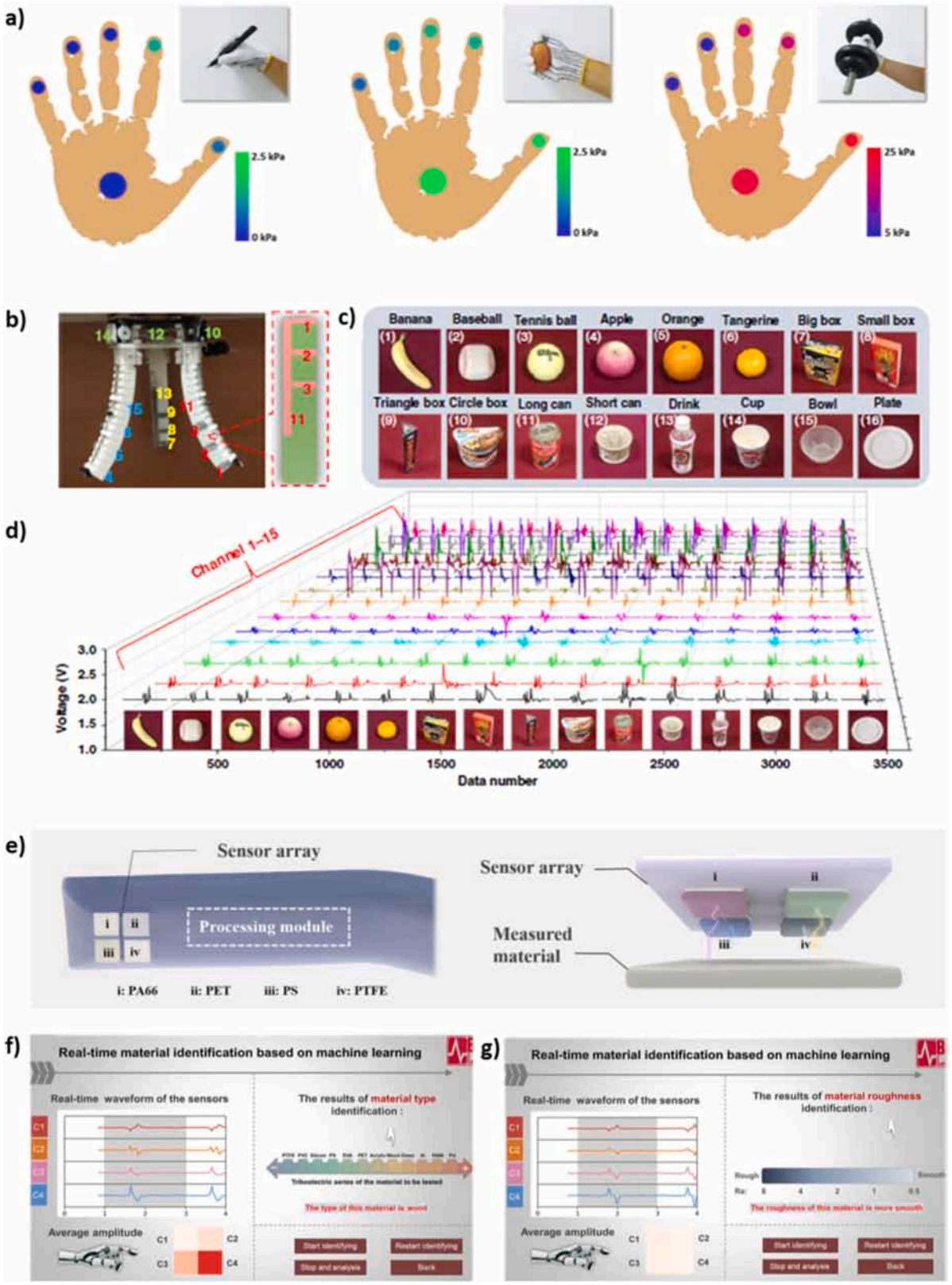

Fig. 29. Self-powered TENGs sensors for tactile perception. a) Hand posture detection during grasping a pen, an egg, and a dumbbell. b) Photograph of the three-fingers soft gripper (Inset figure shows placement of the integrated sensor nodes. c) Sixteen selected objects for gripping and recognition. d) Voltage output generated by each sensor node after gripping the objects. e) Schematic representation of the smart finger and distribution of the triboelectric sensor array on its structure. f) and g) Material type and surface roughness identification.
(a) Reproduce with permission from Ref. [267]. Copyright 2020, Elsevier. (b)–(d) Reproduce with permission from Ref. [268]. Copyright 2020, Nature Publishing Group. (e)–(g) Reproduce with permission from Ref. [271]. Copyright 2020, American Association for the Advancement of Science.

types of triboelectric sensors are mounted on the soft gripper. These two different types of sensors could sense the sliding, contact position, contact area and bending motion, respectively. For the object recognition 15 separate sensor nodes are placed on the 3-fingers soft gripper for data collection as shown in Fig. 29 **(b)**. Selected 16 different objects for recognition is demonstrated in Fig. 29 **(c)**. The triboelectric sensor nodes generated different signals for different selected objects (Fig. 29 **(d)**). Thanks to the machine learning model, which is trained based on the signals obtained, a classification accuracy of 98% has been achieved.

In addition to object recognition, triboelectric sensors are also used for texture and material type detection in the literature [269–275]. Qu et al. proposed a strategy based on triboelectric sensors for simulating tactile perception of human, quantify these parameters to be used in robotic systems or prosthesis as shown schematically in Fig. 29 **(e)** [271]. A smart finger consisting of an array of sensors has been fabricated. The triboelectric layers of each sensor node in the sensor array differed from each other according to their position in the triboelectric series. When the smart finger is placed on a contact object, different triboelectric signals are generated from the sensor nodes. Thanks to these differences, various types of materials (including, EVA, glass, PU, PVC, silicon, and wood) could be determined. Moreover, the sensor array is capable of measuring the roughness of the material by the generated voltage signal. Authors also claimed that change in the generated voltage signals would not cause erroneous identification of the materials type, thanks to the preserved relative ratio between different roughness values of the same material. The display interface of the material type and roughness identification is shown in Fig. 29 **(f)** and **(g)**, respectively.

4.2.2. *Histogram comparison, human-machine Interfaces*

With the recent advancements in computers, machines, and robotics HMI have become an important tool that enables connection between these devices and the human world. Therefore, HMI received significant attention from both industry and academy. The desire for highly sensitive and energy-efficient devices drives researchers to explore various sensing mechanisms. Triboelectric sensors could be an excellent solution for next-generation HMI, and several related studies have been published in the literature [143,276–282].

Zhang et al. fabricated a textured triboelectric nanogenerator-based smart pad for handwriting recognition of three different people [278, 279]. In this work non-arrayed contact separation mode TENGs are fabricated for handwriting recognition. Regardless of the characters, participants write their handwriting signals display significant variation in the time domain due to differences in writing pressure, velocity, acceleration, and other factors. The number and amplitude of pulses in the handwriting signals of the three writers of the same character are found to differ significantly. This is so that the TENG-based handwriting pad, which records sequential handwriting signals, can capture the essential details of each person's unique handwriting habits, such as x-y position, velocity, acceleration, pressure, and pen vibration. The designed structure allows them to obtain classification accuracies of 99.66 %, 93.63 %, 91.36 %, 99.05 % and 97.73 % for English words, Arabic numerals, Chinese characters, English sentences, and the corresponding Chinese sentences, respectively.

Another intriguing flexible touch pad-based HMI is realized by Pu et al. [279]. The design of the touch pad allows user to detect positions in 3D. The structure consisted of a multi-channel positioning layer and a single -channel pressure sensing layer which are based on TENGs. The structure of the touch pad is shown in Fig. 30 **(a)**. The structure is followed by the two-positioning layer and the below these positioning layer contains a pressure sensing layer. Both functional layers work as single electrode TENG. Therefore, an additional shielding layer is set between the positioning layer and the pressure sensing layer to avoid crosstalk between positioning layer and the pressure sensing layer. Finally, a fabricated 3D touch pad is used for anti-peek built-in code which is integrated by both position and pressure information. In this system, in addition to the code generated from the location, there is another code group determined by the pressing force applied to each code number. While the position of the pressed area determined by the voltage signal generated from positioning layer, applied pressure is resolved by the voltage amplitude generated by the pressure layer (Fig. 30 **(b)**).

Moreover, TENGs are also used for controlling "smart" devices. Doganay et al. fabricated core-shell TENG fibers via coaxial wet spinning for this purpose. While the core of the structure is conductive and composed of Ag NWs/carbon black/TPU, the shell is made of TPU, serving as both a dielectric and triboelectric layer [282]. The SEM image of the structure's cross-section can be seen in Fig. 30 **(c)** and **(d)**. The flexibility and stretchability of the core-shell TENG fibers allow them to be conformally integrated into different types of clothing. Therefore, this structure provides a promising platform for HMI devices for IoT applications. The authors fabricated an IoT wristband with the core-shell TENG fibers for remote control of smart devices. A photograph of the wristband and processing circuit can be seen in Fig. 30 **(e)**. The wristband offers a simple and user-friendly way to manage "smart" devices. The core-shell TENG fibers generate a signal when pressed. The generated signal is processed by a circuit and transmitted to a microcontroller unit (MCU). The signal is then sent via Wi-Fi to the "smart" device for further processing and actuation.

Sign-to-speech translation devices are important for HMI and construct a communication bridge between signers and non-signers. Zhou et al. proposed a wearable triboelectric nanogenerator based real-time sign-to-speech translation system [280,282]. The structure of the sensing unit can be observed in Fig. 30 **(f)**, which is composed of a stainless-steel conductive yarn coiled around a rubber microfiber and PDMS layer covering the overall structure. The sensing unit works as a single electrode triboelectric nanogenerator. During the applied axial strain, the contact area between PDMS layer and the coiled structure changes, leasing to the buildup of electrical potential. With using this stretchable sensing unit, authors fabricated a smart glove and placed these sensing units through the fingers in order to sense the finger bending (Fig. 30 **(g)**). Generated electrical signals following each hand gesture are acquisitioned, analyzed and used for training the machine learning model. Generated signals can be observed in Fig. 30 **(h)**. By analyzing 660 acquired hand gesture patterns, a classification accuracy of 98.63 % is obtained.

4.2.3. *Supportive systems for public health*

Sensor research primarily focuses on healthcare, motion monitoring, and biomedical devices. As life expectancy increases, the demand for flexible, energy-efficient, stable, and highly sensitive sensors has surged. Numerous sensor types have been developed in this field, with TENG-based sensors emerging as promising structures for further exploration [283–290]. The main reasons for this are low energy consumption and very fast dynamic response times.

Fang et al. designed a fabric-based triboelectric sensor for real-time arterial pulse monitoring [285]. The fabricated sensor converts skin deformation caused by the arterial pulsation to electricity thanks to triboelectrification. The structure of the sensor is shown in Fig. 30 **(f)**. The outer textile and inner PDMS layer act as sealant to protect the structure against the external water and moisture. Non-woven fluorinated ethylene propylene (FEP) textile and single walled CNTs act as triboelectric layers. A relative motion between CNTs and FEP can be started by the periodic pressure in order to complete the contact-separation process. As a result, during blood circulation, an alternating current of the textile triboelectric sensor will be produced with the periodically increased and decreased pulse pressure. The current response of the fabricated sensor in the stationary position is given in Fig. 30 **(g)** and authors claim that the measured systolic and diastolic pressures are comparable to those obtained from a commercial blood pressure cuff.

Real-time pulse monitoring is not the only focus of today's research.

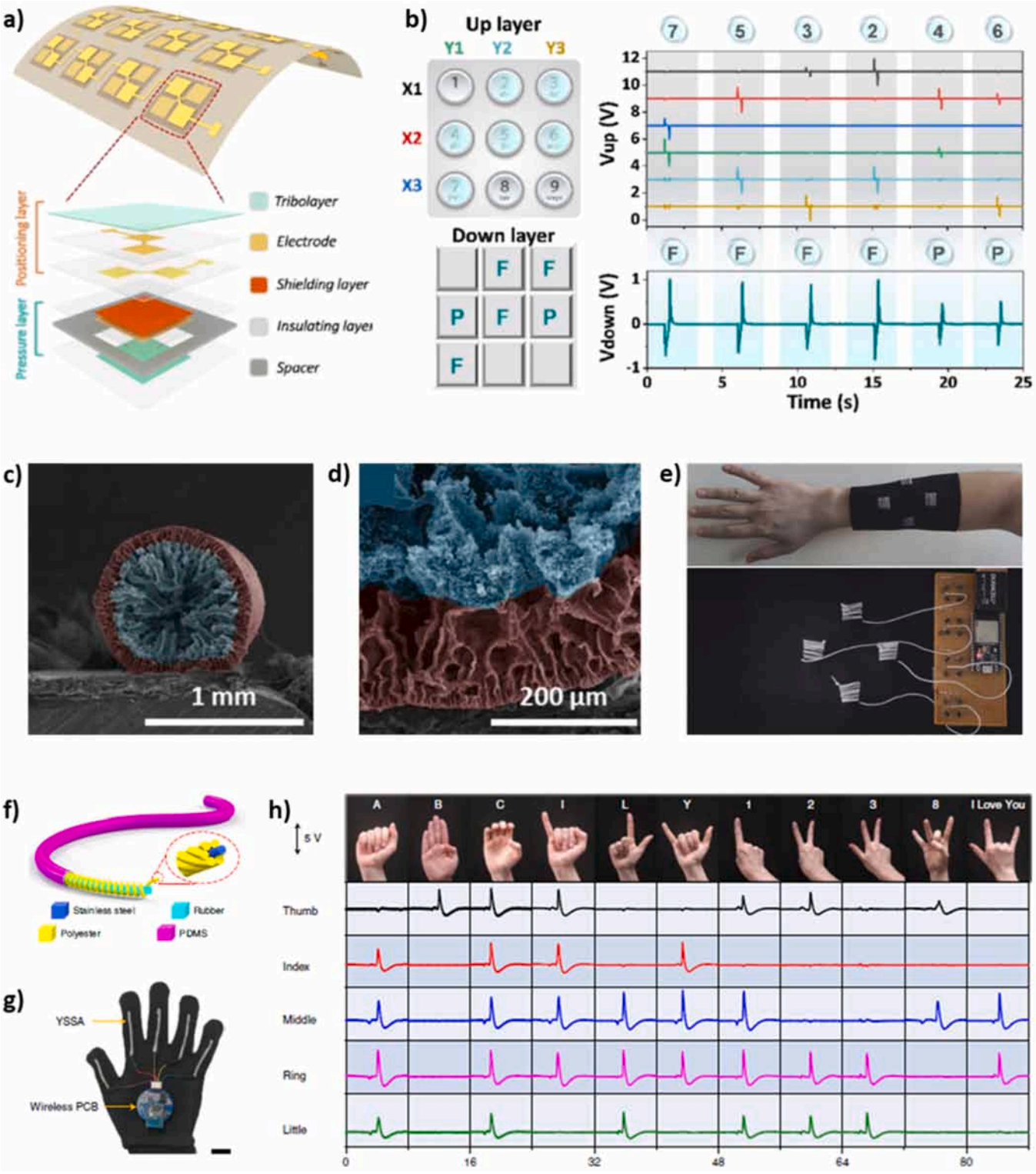

Fig. 30. Self-powered TENGs sensors for HMIs, healthcare and motion monitoring. (a) Schematic representation of the touchpad for detecting 3D touch positions. (b) Voltage output coming from the positioning layer and pressure sensing layer after pressing. (c) and (d). Colored cross-sectional SEM images of the wet spun core-shell TENG fibers. Scale bars were provided below. (e) Photograph of the IOT wrist band and processing circuit. (f) Structure of the stretchable sign-to-speech transition sensing unit. (g) Fabricated smart glove using the stretchable sensing units. (h) Hand gestures and corresponding voltage outputs from the stretchable sensing units located on the fingers.

(a) and (b) Reproduce with permission from Ref. [279]. Copyright 2020, Elsevier. (c)–(e) Reproduce with permission from Ref. [282]. Copyright 2023, Elsevier. (f)–(h) Reproduce with permission from Ref. [280]. Copyright 2020, Nature Publishing Group.

Monitoring the infant health and improving their quality of life form another important branch of sensor research. In this topic Guo et al. designed a triboelectric sensor for continuous measuring and monitoring of the biomechanical pressure exposed to infant body to prevent possible injuries and illnesses [284]. In addition, thanks to the data obtained from the sensors, a deep-learning algorithm recognition of the multiple motion patterns could be possible. The triboelectric sensor works in single electrode contact separation mode and triboelectrification occurred between outer gelatin layer and the skin. Real-time monitoring of the infant's motion is achieved by attaching 11 triboelectric sensors to the specific positions on the body, including the breast, hands, knees, feet, neck, back, wrist and hip. The signals from these sensors are collected separately and simultaneously, representing actions like turning over, holding the infant, backslapping and applauding.

In addition to the biomedical devices, supporting systems for patient rehabilitation are also of crucial importance. In this regard, Bhatia et al. demonstrated an origami triboelectric sensor integrated gravity support device for shoulder rehabilitation [289]. In this work, the triboelectric sensor worked in vertical contract separation mode, and they are employed for the exercise-gaming task which is one of the popular approaches in rehabilitation. Accordance with the arm motion, control of the game was achieved with the help of the triboelectric sensor's output. Also, a clinical study on stroke patients showed the effectiveness of the triboelectric sensor structure on shoulder rehabilitation.

4.2.4. Other self powered sensors

Recently, numerous topics have emerged in the development of TENG-based sensing [291–296]. Advances are being made in areas such as wind speed and direction sensing [241,297–301], inertia detection [302–306], and acoustic sensors [307–311]. This next part showcases the latest approaches in the application of the mentioned sensor types.

Valuable information can be inferred through monitoring wind behavior, namely for agriculture, maritime industry, and electrical power lines. The wind's characteristics have a great impact on these areas and must be monitored thoroughly. Mainly two design approaches can be found for wind sensing. The first method is a rotary structure with parts that cup the wind while the other utilizes a flutter design akin to flags. Furthermore, some of the sensors provided an energy output that allowed them to be self-powered.

In their work, Gu et al. propose a high altitude TENG energy harvester and wind direction sensor implemented in hot air balloons [301]. A picture and schematic of the device is given in Fig. 31 **(a)** and **(b)**, respectively. A wind scoop is utilized to collect the incident wind, which is then analyzed using the rotor passing through the copper electrodes in the DS-TENG for sensing the speed and direction of the wind. Fig. 31 **(c)** shows the obtained voltage from the different parts of the electrodes. The copper parts with the higher area shows a higher voltage output. Then, the incident winds' direction is determined by whether the peaks correspond to a clockwise or counterclockwise rotation, as shown in Fig. 31 **(d)** and **(e)**. A three peak pattern is observed which repeats as the rotor spins over the electrodes. The frequency of these peaks is used to correlate the incident wind speed. Fig. 31 **(f)** and **(g)** show the repeating Voc peaks with increasing wind speed, from which a correlation $R^2 = 0.9967$ is found.

A more intricate design is realized by Ko et al., where a circular TENG that could sense wind speed omnidirectionally is developed [297]. The device utilized the contact electrification between the triangular cut Al-coated PET flaps and the Cu tape-PTFE electrodes, making up a total of 12 such structures. A model of the curved flaps' oscillation is given in Fig. 31 **(h)**. The upward curve given to PET flaps allowed oscillation between PTFE-Cu electrodes possible even at low wind speeds such as 1.5 m/s. The layout of the device is given in Fig. 31 **(i)**. The sensor operated on the RMS of voltage outputs and could effectively monitor the wind speeds between 4 and 10 m/s. A 12-electrode voltage measurement setup is constructed for simultaneous wind speed and direction measurements with 30° intervals.

The same group also came up with a rather unorthodox, cylindrical TENG system that could be used for wind speed and direction sensing [298]. The sensor operated on an acrylic pipe base, lined with 8 Cu tape electrodes covered with PTFE. The counter electrode, prepared by coating a 25 μm thick PET film with Al, is then covered over the base. Stoppers are used at the top of the base to hinder the vertical movement of the PET film. The Karman vortex street formed with the wind passing over the films deforms the shape of the shell and allows for the contact separation between the Al-coated PET film and the PTFE to be exploited. Due to the fluctuations in the output voltages, the RMS of the output values are utilized in the sensing operations. The 8-electrode design allowed for 8-directional sensing using electrode mapping. Wind speed measurement is divided into two sensing regions: 0–3 m/s and 4–10 m/s. The sensor operated for 270 min at a wind speed of 8 m/s, demonstrating extended operation time.

Still, the stability of the materials or the maintenance of the sensing setup being subject to harsh conditions such as abrasion, humidity, rain, and daily temperature changes remain elusive. The interference of many electrodes also causes a challenge in the implementation of perfect omnidirectional sensing.

Inertial and vector sensors have been utilized to understand the relationship between output signals and displacement. Sliding mode and free-standing mode TENGs have been chief among the ones reported, along with DC-TENGs bringing flexibility in many measurement setups.

Li et al. have developed a dual DS-TENG, where the device exploits the principles of both AC and DC TENG mechanisms [302]. The system is integrated into a vehicle steering wheel. While the wheel turns clockwise, air breakdown occurs and DC signals are read, whereas counterclockwise movement of the wheel causes AC signals to be active, as given in Fig. 32 **(a)**. The counterclockwise and clockwise movement of the elbow can be discerned with different TENG responses. The displacement of the steering wheel and the angular rotation could be measured. The linear sensor had a precision of 500 μm and the angular sensor had a precision of 2°. The sensor is insensitive to humidity and temperature and can operate for 500,000 cycles. Additionally, it has been demonstrated for driving direction monitoring and robot movement tracking.

In terms of acceleration sensing, Dai et al. demonstrated a sensor for high-g impact sensing [303]. In the setup, the contact separation of a patterned PDMS layer and Al foil occurred when an impact occurred, causing a tiny air gap to be formed. Through this air gap, the acceleration of the impact could be measured. The device is quite small with dimensions of 14 × 14 × 8 cm. A machete hammer is used to test for impact, yielding a measurement range of up to 1.8×10^4 g and a sensitivity of 1.8 mV/g.

Using a DC-TENG setup, Yin et al., designed a motion vector sensor involving four electrodes [304]. On a square acrylic plate, four Cu electrodes are lined over the four sides. Air breakdown occurred when the plate moved over an FEP film on a xy plane, as can be seen in Fig. 32 **(b)** and **(c)**. Through the change in the voltages for the four electrodes, displacement vs voltage graphs could easily be drawn for all directions. The 1st and 2nd derivatives of these graphs also allowed for velocity and acceleration to be measured, given in Fig. 32 **(d)**. When a similar structure is implemented over a disk, the rotation of the FEP film over Cu electrodes allowed the angular velocity and the angle to be measured as well. A schematic for the disk system is given in Fig. 32 **(e)**, and the respective response is given in Fig. 32 **(f)**. Using these principles, an intelligent pen is developed realizing trajectory tracing, mapping, and writing on a curved surface.

Acoustic sensors represent a relatively new area of study in TENGs. These sensors typically operate through thin membranes that vibrate, mimicking the function of an eardrum. With the recent surge in IoT, the latest works in this field implemented ML (machine learning) and HRI (human-robot interface). From audio source recognition to user identification, acoustic sensing via TENGs is becoming increasingly functional.

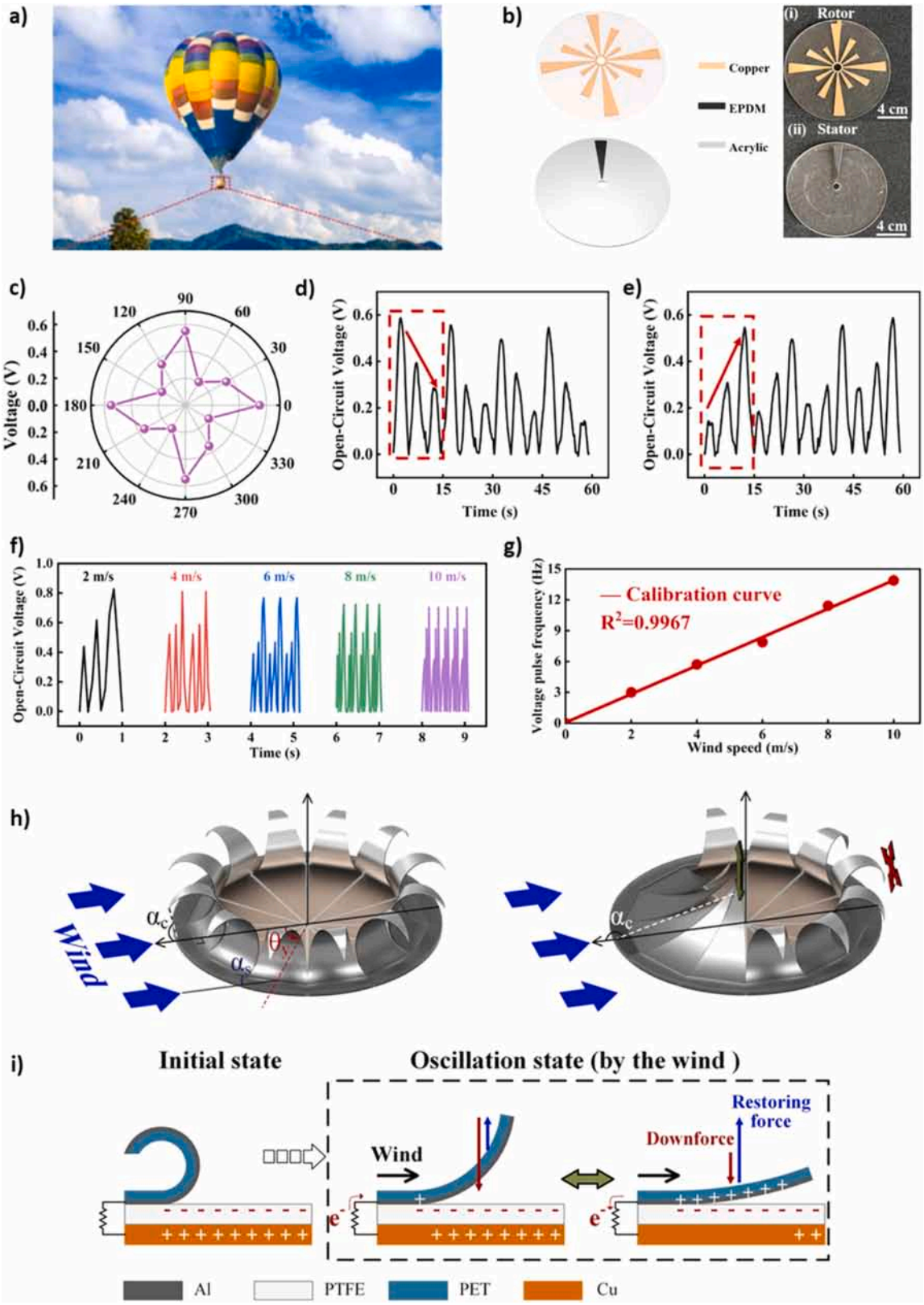

Fig. 31. Self-powered TENGs sensor for monitoring wind characteristics. (a) An image of the hot air balloon and (b) the TENG setup, (c) the radial Voc output from the sensor, Voc peaks from the (d) clockwise and (e) counter-clockwise rotation of the TENG, (f) the repeating Voc peaks with increasing wind peaks, (g) graph showing the correlation between the wind speed and repeating Voc peaks. (h) a model showing the behavior of the flaps upon oscillation (i) the materials used, and the working mechanism shown upon incident wind.
(a)–(g) Reproduce with permission from Ref. [301]. Copyright 2023, Elsevier. (h) and (i) Reproduce with permission from Ref. [297]. Copyright 2022, Elsevier.

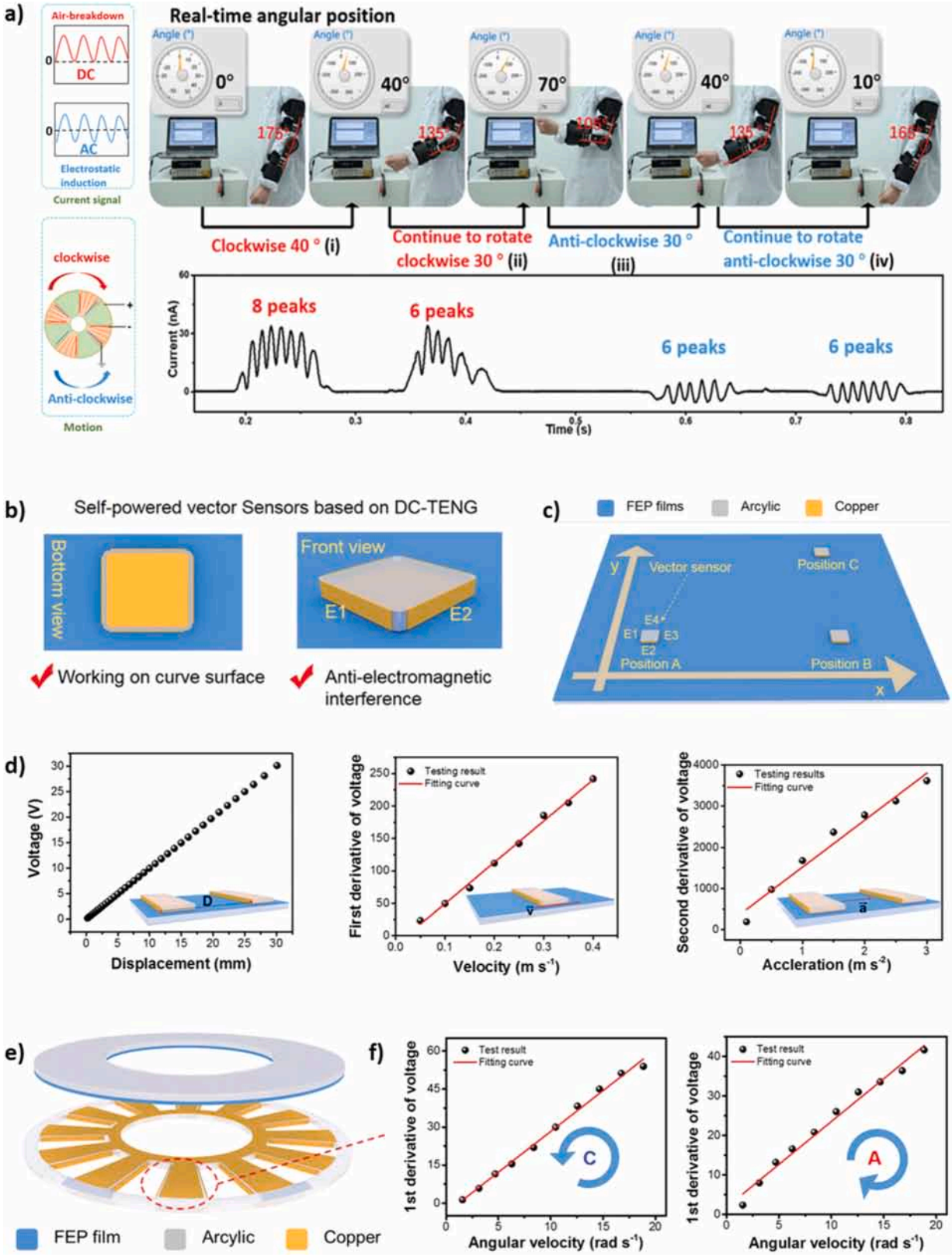

Fig. 32. Self-powered TENGs sensor for vector sensing. a) The self-powered dual vector sensor mechanism, with DC signals measuring clockwise rotation and AC signals measuring counterclockwise rotation, b) a drawing of the DC-TENG for motion vector sensing, c) the materials and linear trajectories used for sensing, d) the displacement, velocity, and acceleration sensing capability of the device, e) the disk layout for the DC-TENG and, f) the angular velocity sensing for both clockwise and counterclockwise rotation.

(a) Reproduce with permission from Ref. [302]. Copyright 2022, Wiley-VCH. (b)–(f) Reproduce with permission from Ref. [304]. Copyright 2020, Wiley-VCH.

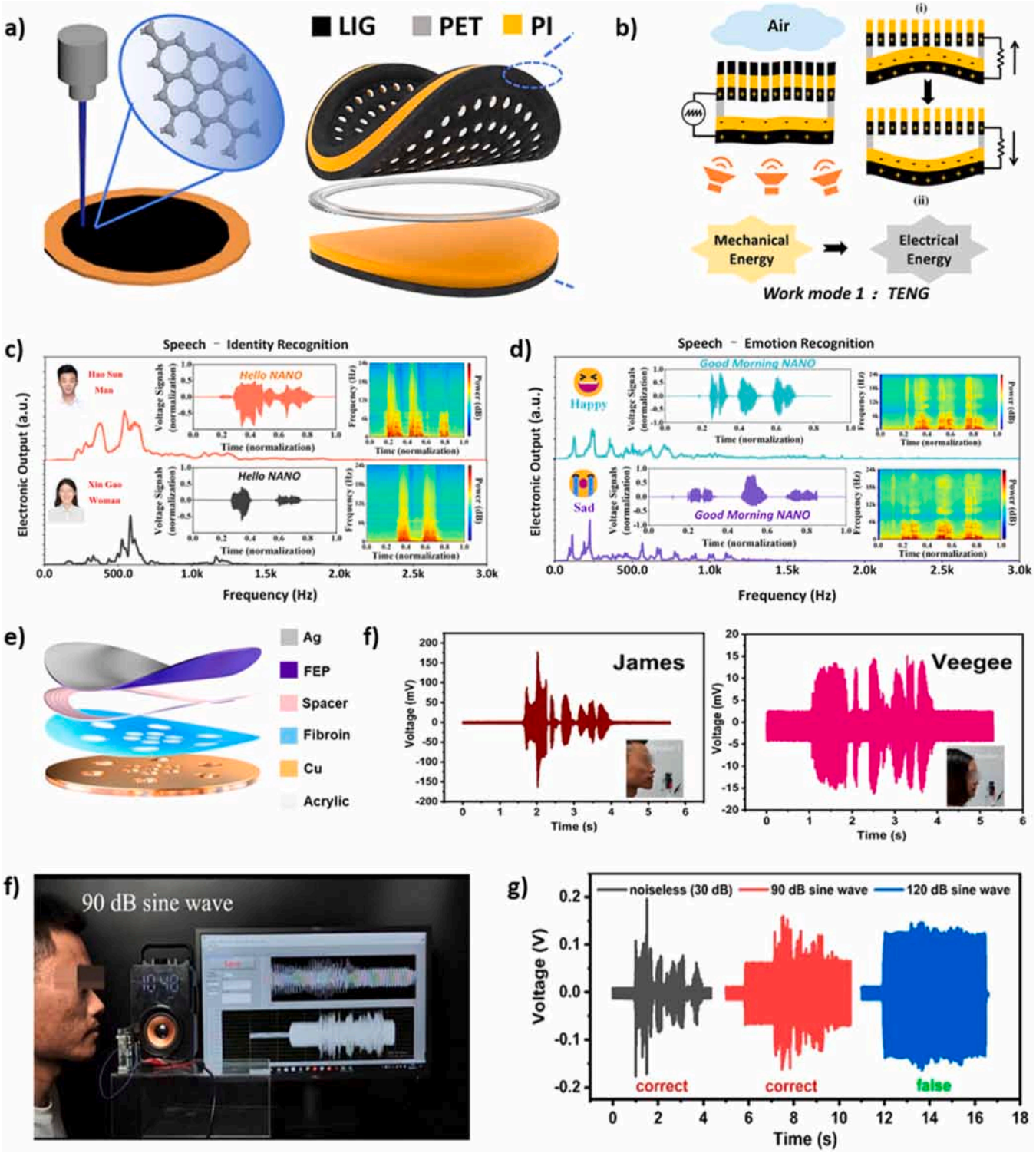

Fig. 33. Self-powered TENGs acoustic sensors for speech and emotion sensing. (a) The production and the constituents of the acoustic sensor, (b) the working mechanism of the TENG part of the device, the acoustic sensing capabilities of the device in terms of (c) speech and (d) emotion sensing. (e) the schematic and constituents of the VGST, (f) the speech recognition capabilities of the sensor, and the sensing performance under external noise (g) picture of the experimental setup and (h) performance of the sensor when external noise is applied.
(a)–(d) Reproduce with permission from Ref. [312]. Copyright 2022, Wiley-VCH. (e)–(h) Reproduce under Creative Commons CC BY 4.0 from Ref. [307].

In that regard, Sun et al., have developed an acoustic transducer where both sound sensing and emission is possible [312]. The device utilized LIG (laser-induced graphene) electrodes, a PI film, and PET spacers. Schematics of the device are given in Fig. 33 **(a)**. The working mechanism of the TENG is given in Fig. 33 **(b)**. The triboelectric output of the device is used for sound sensing, and the thermoacoustic ability of LIG is utilized in the loudspeaker. High sensitivity (4500 mV/Pa) and wide frequency response (20–20,000 Hz) is achieved through the device. The researchers showcased the system in a robot called "NANO", with which they could interact. Using ML, NANO could perform

multi-dimensional speech recognition and emotion perception with an accuracy of 99.66 % in training and 96.63 % in test samples. The response of the device to two speakers is given in Fig. 33 **(c)** and **(d)**. The device correctly identified 6 different speakers and showed emotional recognition for a man and a woman. Researchers also reported that the device maintained durability over 1,000,000 cycles within 60 days.

Luo et al. show an eco-friendlier approach to the materials used in the system [307]. Their VGST (voice and gesture translator) consists of silk fibroin sprayed onto Cu film and Ag-sputtered FEP film separated by a spacer. The schematic of the device is given in Fig. 33 **(e).** Holes are cut into the Cu film to allow the oscillation of the FEP film, creating the voltage output used for sensing. The VGST has a wide range of frequency response (20–20,000 Hz) and high sensitivity (167 mV/dB). As for voice and gesture recognition, the accuracy reached 97 %. The device is trained by two men and a woman and could identify the speaker accurately as can be seen in Fig. 33 **(f)**. The performance of the device is tested further using external sounds up to 120 dB s, as shown in Fig. 33 **(g)** and **(h)**.

Yang et al., implemented a Faraday cage into the design in the form of a steel shell and a steel mesh to isolate electromagnetic interference for their T-MIC [308]. A 400 Å Cu layer is evaporated onto the FEP film as the triboelectric layers. The vibration between FEP and the metal film is the cause of triboelectrification and the output voltage. The sensor is capable of detecting a wide frequency range (20–20,000 Hz) at a resolution of 1 Hz, showcasing a high sensitivity. In addition, the HRI potential of the system is realized when the T-MIC is installed on a robot. The robot responded to voice signals such as “go forward”, “turn right”, and “go backward”. It also used T-MIC as a switch to turn itself on and off. T-MIC also had a speech-to-text function for the phrase “Hello, it’s a nice day”. With acoustic sensors utilizing ML more, low-cost TENG devices could be trained more effectively for more advanced recognition. Fine-tuning musical instruments, precise and faster person identification, and bioacoustics are prospective fields where TENGs could be implemented.

Triboelectric nanogenerator-based sensors are used extensively in the various fields including, tactile perception, HMI, healthcare monitoring, and biomedical devices. These types of sensors demonstrate great potential on fast response time and low-energy consumption. Addition to that, triboelectric nanogenerator-based sensors can open a new perspective on tactile perception by differentiating in-contact materials. In this regard, these types of sensors can be very useful for next-generation robotics. However, despite the advantages we have mentioned, more work is needed in this area in order to be used frequently in industrial applications and to get ahead of competitor sensing technologies such as, capacitive, iontronic and resistive sensing. Many problems are still not fully resolved and there are some limitations that need to be overcome. Firstly, sensitivity of the triboelectric sensors is lower than their capacitive, iontronic and resistive counterparts. Addition to that, incapability of measuring static pressures makes this type of sensing unpractical in many fields. The performance of triboelectrification is also highly sensitive to environmental conditions like humidity and temperature. Therefore, changing environmental conditions alters the performance of the sensors which is not desirable. Moreover, the triboelectrification performance highly depends on the fabrication process of the triboelectric layers. In this regard, consistently manufacturing sensors of the same quality remains a challenging task. Besides these, TENG sensors are often susceptible to external factors like background noise and changes in intensity, which complicate data analysis. As a result, manually processing data with weak and varied features can be quite challenging. Therefore, using machine learning enables effective analysis and accurate predictions for processing the TENG outputs [313].

5. Summary and perspectives

Interest in 21st century energy harvesting technologies is growing due to environmental concerns, political reasons, and rising energy demands. Macro-scale (kW) energy harvesters like solar cells, wind turbines stand out in terms of technology readiness level and they have an important place in environmentally friendly energy production. However, especially with the developments in the IOTs, harvesting micro scale energy has also become a great need. Since, meeting the energy needs of IOT devices with external batteries is not always a practical solution. For these reasons, TENGs have received considerable attention to harvest waste mechanical energy at small frequencies. This interest is increasing as new application areas are put forward by the pioneers of the field. This review aims to elucidate the fundamental aspects of TENGs, providing a guide for researchers new to the field.

Firstly, the basics of TENGs are explained under three main headings. These are contact electrification mechanisms, operating modes of TENGs, and operational models of TENGs. The possible mechanisms of contact electrification, one of the oldest mysteries in history, are discussed for solid-solid surfaces. The amount of the charges created on the surfaces upon contact is the main factor determining TENGs performance. However, the actual mechanism of contact electrification is controversial. Electron, ion and material transfers have been proposed as sources of contact charge. Strong evidence for each mechanism is presented in the literature, such as contact charge mosaics, the correlation between the amount of contact charges and the zeta potentials of the surfaces, and thermionic emissions observed on charged surfaces. The increase in interest of TENGs and the studies on understanding the mechanisms of contact electrification feed each other. Understanding the mechanism of contact electrification will enable engineers to construct TENG devices with much larger efficiencies. Likewise increasing interest in TENGs will motivate scientists to work for understanding the contact electrification mechanism. The working modes of TENGs and their advantages and disadvantages are discussed. One of the most important advantages of TENGs is that they have different working modes which are vertical contact separation, lateral sliding, single electrode and freestanding modes. The fact that TENGs have different modes provides application-specific flexibility in device design, as long as their advantages and disadvantages are carefully evaluated. Theoretical models explaining the operational mechanisms of TENGs are discussed. The models are investigated under two headings, namely equivalent circuit models and quasi electrostatic models. Equivalent circuit models are created using lumped parameter models that represent TENGs as circuit elements that act as voltage or current sources with inherent capacitance or impedance. The capacitive model is the first model in which TENGs are modeled as equivalent circuits. It describes the TENG device as voltage source and capacitance. Later, Thevenin’s and Norton’s Models are proposed. TENGs are modeled as current source and impedance in Norton’s equivalent circuit. Using Norton’s equivalent circuit to model the TENG system becomes crucial when TENG devices exhibit high inherent impedance. Accurately measuring open circuit voltage can be challenging under high inherent impedance conditions in a TENG system. This difficulty arises because voltage measurement units are limited by limited impedance of the measurement systems. Conversely, quasi electrostatic models are based on classical electromagnetic theory, focusing on the internal dynamics of TENGs by incorporating Maxwell’s equations. The first model based on classical electromagnetics is the distance dependent electrical field (DDEF) model. Later, a 3D mathematical (finite-sized charged plane (FSCP)) model is developed. In these models, electric fields as the result of contact charge separation are calculated between two conductive electrodes. Equivalent circuit models are used because they are practical. However, they show large deviations from the experimental results due to the edge effect as the contact separation distance increases compared to quasi electrostatic models.

Secondly, strategies to increase efficiency of TENGs are discussed. Energy harvesting efficiency and energy transfer efficiency decide the overall efficiency of a TENG system. Energy harvesting efficiency depends on the contact charge density and separation distance of the

contact charges. The separation distance of the contact charges is mostly limited by design and is often not possible to change much. Therefore, increasing contact charge density is the main strategy to increase energy harvesting efficiency of a TENG system. Increasing contact charge density starts with proper material selection from the TENG series. That is combining tribonegative and tribopositive surfaces in design is the starting point. Modification of the contact layers are also frequently proposed. These modifications can be physical or chemical modification of the surfaces, as well as structural changes by developing composite structures or changing the chemistry of the contact layers. However, charge density is limited by the discharge of contact charges, which is described as air breakdown. Air breakdown limits can be increased by applying alternative lubricants between the contact layers or by performing the measurement under vacuum. Contact charge density can also be increased by charge pumping and charge excitation by designing special circuits. To realize TENGs' true potential, it is also crucial to efficiently transfer the harvested energy to storage devices. The conversion and transfer of the harvested electrical energy is done by power management circuits. Output requirements of these circuits are determined by the TENG application and powered electronics. To satisfy these requirements there are two strategies to improve, namely energy conversion and storage efficiency. The first one is boosting transferred charge to an external circuit with methods such as cycle for maximize energy output and charge pumping. Cycle for maximized energy output involves the instantaneous short-circuiting of TENG electrodes for maximized charge transfer and charge pumping involves coupling of external TENG or circuit for boosting transferred charge quantity. The second task of power management circuits is efficient power conversion involving rectification and regulation of the generated signal. Rectification converts the AC generated by TENG into DC for use in electronic devices. This process can be bypassed using TENG setups that generate DC instead of AC. TENGs typically generate high voltage and low current. To be used for powering electronic devices, voltage should be stepped down. This can be achieved using inductive and capacitive transformers or buck converters. Using these circuit elements, the power management circuits of TENG systems should be designed specifically to match the power generated by the TENG with the power required by the externally connected electronics.

Finally, the applications of TENGs are discussed through recent examples. TENG applications can be classified according to the source of mechanical energy (blue, wind, biomechanical etc.) or the end purpose (harvesting or sensing). In this review, applications are first divided into harvesting and sensing and then examined according to the source of energy. TENGs have the potential to provide the energy required for the operation of IoT devices by harvesting energy at the micro scale. This reduces the frequency of battery charging in devices and may even eliminate the need for external charging of these batteries. Additionally, TENGs themselves can be used as self-powered sensors to monitor changes in input mechanical energy. For TENGs to reach their full potential, key challenges must be addressed, and important research directionsas follows should be pursued:

1. Fundamental research, both experimental and computational, needs to be prioritized for a better understanding of the mechanism of contact electrification and therefore for the design of TENG devices with higher efficiency. One of the major challenges for the commercial use of TENGs isthe strong dependence of contact charge density on environmental factors like humidity and temperature. A deeper understanding of the mechanism will also help in minimizing the environmental impact on device performance.
2. This field of research is a relatively new; therefore, there has not yet been a consensus on measurement and reporting of the results. The output power of a TENG device is highly dependent on factors such as pressure, frequency and humidity of the environment. Therefore, it is possible to get different results even in TENG systems made with the same materials. If a material is developed for the triboelectric and conductive layers, the contact charge should be separately examined under a standard condition and reported before constructing a TENG device with the triboelectric layer. It will be equally important to measure and report the output performance of the constructed TENG device at specific frequencies and relative humidity values as a standard. Moreover, output voltage and current values in the literature are often reported as several peaks. However, given the chaotic nature of the contact electrification, a statistical approach should be adopted instead.
3. The low stability of TENG devices remains another key challenge. Triboelectric layers wear out over time due to friction, especially in devices TENG devices operating in freestanding and lateral sliding modes. However, as explained in the theoretical models section, the contact charges formed in the triboelectric layers reach saturation after a few cycles. The power output obtained is through induced electrons between the conductive layers. Therefore, smart switches to be implemented in the device can break the contact after the surface charges reach saturation, allowing the electrodes to change their positions without touching each other. This ensures that the device remains stable as the surfaces will not come into contact with each other after the first few cycles. Additionally, as mentioned in the relevant parts of the review, injecting lubricants between the two triboelectric layers can enhance performance by suppressing the air breakdown effect and extend device lifespan by reducing friction.
4. Various power management circuit designs have been proposed in the literature to enhance energy harvesting and transfer efficiency. All of these circuit designs feature rigid structures, limiting the ability of TENGs to be used in flexible, stretchable or wearable applications. Complete systems, including flexible or stretchable power management circuits and TENG transducers, need to be developed to fully realize the potential of wearable TENGs.

CRediT authorship contribution statement

Cicek Melih Ogeday: Writing – review & editing, Writing – original draft, Formal analysis, Conceptualization. **Cakir Onuralp:** Writing – review & editing, Writing – original draft, Investigation, Conceptualization. **Cugunlular Murathan:** Writing – review & editing, Writing – original draft, Investigation, Formal analysis. **Durukan Mete Batuhan:** Writing – review & editing, Writing – original draft, Visualization, Investigation, Formal analysis, Conceptualization. **Doganay Doga:** Writing – review & editing, Writing – original draft, Visualization, Investigation, Formal analysis, Conceptualization. **Unalan Husnu:** Writing – review & editing, Writing – original draft, Visualization, Project administration, Conceptualization. **Wei Di:** Writing – review & editing, Writing – original draft, Project administration, Conceptualization. **Demircioglu Onur:** Writing – review & editing, Writing – original draft, Investigation, Conceptualization.

Declaration of Competing Interest

The authors declare that they have no known competing financial interests or personal relationships that could have appeared to influence the work reported in this paper.

Acknowledgements

D.D. and H.E.U. acknowledges support from the Middle East Technical University through the Scientific Research Projects Programme under project number TEZ-D-308–2021-10715. D.W. acknowledges support from the National Natural Science Foundation (grant number 22479016).

Data availability

No data was used for the research described in the article.

References

[1] S. Al-Sarawi, M. Anbar, R. Abdullah, A.B. Al Hawari, Internet of things market analysis forecasts, 2020–2030, in: Proceedings of the 2020 Fourth World Conference on Smart Trends in Systems, Security and Sustainability (WorldS4), IEEE, 2020, pp. 449–53. ⟨https://doi.org/10.1109/WorldS450073.2020.9210375⟩.

[2] A. Ferguson, Faraday's diary: being the various philosophical notes of experimental investigation made by Michael Faraday, DCL, FRS, during the years 1820–1862 and bequeathed by him to the Royal Institution of Great Britain, Nature 130 (1932) 828–830, https://doi.org/10.1038/130828a0.

[3] J. Wimshurst LXIII, Alternating and experimental influence-machine, Lond. Edinb. Dublin Philos. Mag. J. Sci. 31 (1891) 507–511, https://doi.org/10.1080/14786449108620150.

[4] F.A. Furfari, A history of the Van de Graaff generator, IEEE Ind. Appl. Mag. 11 (2005) 10–14, https://doi.org/10.1109/MIA.2005.1380320.

[5] F.R. Fan, Z.Q. Tian, Z. Lin Wang, Flexible triboelectric generator, Nano Energy 1 (2012) 328–334, https://doi.org/10.1016/j.nanoen.2012.01.004.

[6] F.-R. Fan, L. Lin, G. Zhu, W. Wu, R. Zhang, Z.L. Wang, Transparent triboelectric nanogenerators and self-powered pressure sensors based on micropatterned plastic films, Nano Lett. 12 (2012) 3109–3114, https://doi.org/10.1021/nl300988z.

[7] G. Zhu, C. Pan, W. Guo, C.-Y. Chen, Y. Zhou, R. Yu, Z.L. Wang, Triboelectric-generator-driven pulse electrodeposition for micropatterning, Nano Lett. 12 (2012) 4960–4965, https://doi.org/10.1021/nl302560k.

[8] S. Wang, L. Lin, Z.L. Wang, Nanoscale triboelectric-effect-enabled energy conversion for sustainably powering portable electronics, Nano Lett. 12 (2012) 6339–6346, https://doi.org/10.1021/nl303573d.

[9] C. Wu, A.C. Wang, W. Ding, H. Guo, Z.L. Wang, Triboelectric nanogenerator: a foundation of the energy for the new era, Adv. Energy Mater. 9 (2019), https://doi.org/10.1002/aenm.201802906.

[10] D. Choi, Y. Lee, Z.-H. Lin, S. Cho, M. Kim, C.K. Ao, S. Soh, C. Sohn, C.K. Jeong, J. Lee, M. Lee, S. Lee, J. Ryu, P. Parashar, Y. Cho, J. Ahn, I.-D. Kim, F. Jiang, P. S. Lee, G. Khandelwal, S.-J. Kim, H.S. Kim, H.-C. Song, M. Kim, J. Nah, W. Kim, H. G. Menge, Y.T. Park, W. Xu, J. Hao, H. Park, J.-H. Lee, D.-M. Lee, S.-W. Kim, J. Y. Park, H. Zhang, Y. Zi, R. Guo, J. Cheng, Z. Yang, Y. Xie, S. Lee, J. Chung, I.-K. Oh, J.-S. Kim, T. Cheng, Q. Gao, G. Cheng, G. Gu, M. Shim, J. Jung, C. Yun, C. Zhang, G. Liu, Y. Chen, S. Kim, X. Chen, J. Hu, X. Pu, Z.H. Guo, X. Wang, J. Chen, X. Xiao, X. Xie, M. Jarin, H. Zhang, Y.-C. Lai, T. He, H. Kim, I. Park, J. Ahn, N.D. Huynh, Y. Yang, Z.L. Wang, J.M. Baik, D. Choi, Recent advances in triboelectric nanogenerators: from technological progress to commercial applications, ACS Nano 17 (2023) 11087–11219, https://doi.org/10.1021/acsnano.2c12458.

[11] W.-G. Kim, D.-W. Kim, I.-W. Tcho, J.-K. Kim, M.-S. Kim, Y.-K. Choi, Triboelectric nanogenerator: structure, mechanism, and applications, ACS Nano 15 (2021) 258–287, https://doi.org/10.1021/acsnano.0c09803.

[12] A.K.T. Assis, The experimental and historical foundations of electricity, Apeiron (2010).

[13] Plato, Timaeus, n.d.

[14] S.L. Miller, 33. A Production of Amino Acids under Possible Primitive Earth Conditions, n.d.

[15] L.B. Loeb, The basic mechanisms of static electrification, Science (1979) 102 (1945) 573–576, https://doi.org/10.1126/science.102.2658.573.

[16] D.J. Lacks, T. Shinbrot, Long-standing and unresolved issues in triboelectric charging, Nat. Rev. Chem. 3 (2019) 465–476, https://doi.org/10.1038/s41570-019-0115-1.

[17] William Gilbert, On the Loadstone and Magnetic Bodies and on the Great Magnet the Earth. A New Physiology Demonstrated with Many Arguments and Experiments. A Translation By P. Fleury Mottelay, Bernard Quaritch Ltd, London, 1893.

[18] C.F. de C. Dufay, Quatrieme mémoire sur l'électricité. De l'attraction et répulsion des corps électriques, Hist. de l'Acad. R. Des Sci. Avec Les. M. de Math. de Phys. Pour La m. Ême Ann. (1733) 457–477.

[19] Benjamin Franklin, Experiments and Observations On Electricity, London, 1751.

[20] J.C. Wilcke, Dispvtatio Physica Experimentalis, De Electricitatibvs Contrariis: Qvam Consentiente, 1757.

[21] P.E. Shaw, Experiments on tribo-electricity. I. The tribo-electric series, Philos. Trans. R. Soc. Lond. 217 (1917) 37.

[22] P.E. Shaw, The electrical charges from like solids, Nature 118 (1926).

[23] S. Pence, V.J. Novotny, A.F. Diaz, Effect of Surface Moisture on Contact Charge of Polymers Containing Ions, 1994. ⟨https://pubs.acs.org/sharingguidelines⟩.

[24] T.A. de L. Burgo, C.A. Rezende, S. Bertazzo, A. Galembeck, F. Galembeck, Electric potential decay on polyethylene: role of atmospheric water on electric charge build-up and dissipation, J. Electrostat. 69 (2011) 401–409, https://doi.org/10.1016/j.elstat.2011.05.005.

[25] H.T. Baytekin, B. Baytekin, S. Soh, B.A. Grzybowski, Is water necessary for contact electrification? Angew. Chem. 123 (2011) 6898–6902, https://doi.org/10.1002/ange.201008051.

[26] A. Šutka, K. Malnieks, L. Lapčinskis, P. Kaufelde, A. Linarts, A. Berziņa, R. Zabels, V. Jurķans, I. Gorņevs, J. Blums, M. Knite, The role of intermolecular forces in contact electrification on polymer surfaces and triboelectric nanogenerators, Energy Environ. Sci. 12 (2019) 2417–2421, https://doi.org/10.1039/c9ee01078e.

[27] K. Shi, B. Chai, H. Zou, Z. Wen, M. He, J. Chen, P. Jiang, X. Huang, Contact electrification at adhesive interface: boosting charge transfer for high-performance triboelectric nanogenerators, Adv. Funct. Mater. 33 (2023), https://doi.org/10.1002/adfm.202307678.

[28] L. Lapčinskis, K. Mālnieks, J. Blūms, M. Knite, S. Oras, T. Käämbre, S. Vlassov, M. Antsov, M. Timusk, A. Šutka, The adhesion-enhanced contact electrification and efficiency of triboelectric nanogenerators, Macromol. Mater. Eng. 305 (2020), https://doi.org/10.1002/mame.201900638.

[29] J. Lowell, A.C. Rose-Innes, Contact electrification, Adv. Phys. 29 (1980) 947–1023, https://doi.org/10.1080/00018738000101466.

[30] R. Xu, S. Ye, K. Xu. Theory Contact Electrification, 1953.

[31] L.S. McCarty, G.M. Whitesides, Electrostatic charging due to separation of ions at interfaces: contact electrification of ionic electrets, Angew. Chem. - Int. Ed. 47 (2008) 2188–2207, https://doi.org/10.1002/anie.200701812.

[32] S.R. Waitukaitis, V. Lee, J.M. Pierson, S.L. Forman, H.M. Jaeger, Size-dependent same-material tribocharging in insulating grains, Phys. Rev. Lett. 112 (2014), https://doi.org/10.1103/PhysRevLett.112.218001.

[33] Z.L. Wang, A.C. Wang, On the origin of contact-electrification, Mater. Today 30 (2019) 34–51, https://doi.org/10.1016/j.mattod.2019.05.016.

[34] C. Liu, A.J. Bard, Electrostatic electrochemistry at insulators, Nat. Mater. 7 (2008) 505–509, https://doi.org/10.1038/nmat2160.

[35] C.Y. Liu, A.J. Bard, Chemical redox reactions induced by cryptoelectrons on a PMMA surface, J. Am. Chem. Soc. 131 (2009) 6397–6401, https://doi.org/10.1021/ja806785x.

[36] C. yang Liu, A.J. Bard, Electrostatic electrochemistry: nylon and polyethylene systems, Chem. Phys. Lett. 485 (2010) 231–234, https://doi.org/10.1016/j.cplett.2009.12.009.

[37] B. Baytekin, H.T. Baytekin, B.A. Grzybowski, What really drives chemical reactions on contact charged surfaces? J. Am. Chem. Soc. 134 (2012) 7223–7226, https://doi.org/10.1021/ja300925h.

[38] S. Li, Z. Zhang, P. Peng, X. Li, Z.L. Wang, D. Wei, A green approach to induce and steer chemical reactions using inert solid dielectrics, Nano Energy 122 (2024) 109286, https://doi.org/10.1016/j.nanoen.2024.109286.

[39] S. Li, J. Liu, Z.L. Wang, D. Wei, Mechano-driven chemical reactions, Green Energy Environ. (2024), https://doi.org/10.1016/j.gee.2024.08.001.

[40] J.A. Mendley, Frictional electrification of polar polymers, Nature 171 (1953) 1077.

[41] A.F. Diaz, Contact electrification of materials: the chemistry of ions on polymer surfaces, J. Adhes. 67 (1998) 111–122, https://doi.org/10.1080/00218469808011102.

[42] W.D, D.D. Diaz A.F, Contact electrification: ion transfer to metals and polymers, Chem. Mater. 3 (1991) 997.

[43] J.A. Wiles, M. Fialkowski, M.R. Radowski, G.M. Whitesides, B.A. Grzybowski, Effects of surface modification and moisture on the rates of charge transfer between metals and organic materials, J. Phys. Chem. B 108 (2004) 20296–20302, https://doi.org/10.1021/jp0457904.

[44] A. Šutka, A. Linarts, K. Mālnieks, K. Stiprais, L. Lapčinskis, Dramatic increase in polymer triboelectrification by transition from a glassy to rubbery state, Mater. Horiz. 7 (2020) 520–523, https://doi.org/10.1039/C9MH01425J.

[45] K.P. Homewood, Do "dirty" surfaces matter in contact electrification experiements? J. Electrost. (1981).

[46] J. Wang, C. Wu, Y. Dai, Z. Zhao, A. Wang, T. Zhang, Z.L. Wang, Achieving ultrahigh triboelectric charge density for efficient energy harvesting, Nat. Commun. 8 (2017), https://doi.org/10.1038/s41467-017-00131-4.

[47] A. Šutka, K. Mālnieks, L. Lapčinskis, M. Timusk, K. Kalniņš, A. Kovaļovs, J. Bitenieks, M. Knite, D. Stevens, J. Grunlan, Contact electrification between identical polymers as the basis for triboelectric/flexoelectric materials, Phys. Chem. Chem. Phys. 22 (2020) 13299–13305, https://doi.org/10.1039/D0CP01947J.

[48] John Henniker, Triboelectricity in polymers, Nature 196 (1962) 474, https://doi.org/10.1038/196474a0.

[49] S.V. Pepper, Auger analysis of films formed on metals in sliding contact with halogenated polymers, J. Appl. Phys. 45 (1974) 2947–2956, https://doi.org/10.1063/1.1663707.

[50] W.A. Brainard, D.H. Buckley, Adhesion and friction of PTFE in contact with metals as studied by Auger spectroscopy, field ion and scanning electron microscopy, Wear 26 (1973) 75–93, https://doi.org/10.1016/0043-1648(73)90151-8.

[51] W.R. Salaneck, A. Paton, D.T. Clark, Double mass transfer during polymer-polymer contacts, J. Appl. Phys. 47 (1976) 144–147, https://doi.org/10.1063/1.322306.

[52] J. Sohma, Mechanochemistry of polymers, Prog. Polym. Sci. 14 (1989) 451–596, https://doi.org/10.1016/0079-6700(89)90004-X.

[53] Y.-R. Luo, Handbook of Bond Dissociation Energies in Organic Compounds, CRC Press, 2002, https://doi.org/10.1201/9781420039863.

[54] O. Verners, L. Lapčinskis, P.C. Sherrell, A. Šutka, Contact electrification at dielectric polymer interfaces: on bond scission, material transfer, and electron transfer, Adv. Mater. Interfaces 10 (2023), https://doi.org/10.1002/admi.202300562.

[55] H. Fu, J. Gong, J. Cao, Z. Zhang, Z. Long, B. Yang, J. Chen, Y. Chen, X. Tao, Understanding contact electrification *via* direct covalent bond cleavage of polymer chains for ultrahigh electrostatic charge density, Energy Environ. Sci. 17 (2024) 3776–3787, https://doi.org/10.1039/D4EE00395K.

[56] M. Rubens, P. Falireas, K. Vanbroekhoven, W. Van Hecke, G.E. Kaya, B. Baytekin, R. Vendamme, Molecular design of lignin-derived side-chain phenolic polymers toward functional radical scavenging materials with antioxidant and antistatic properties, Biomacromolecules (2023), https://doi.org/10.1021/acs.biomac.3c00275.

[57] M. Özel, F. Demir, A. Aikebaier, J. Kwiczak-Yiğitbaşı, H.T. Baytekin, B. Baytekin, Why does wood not get contact charged? Lignin as an antistatic additive for common polymers, Chem. Mater. 32 (2020) 7438–7444, https://doi.org/10.1021/acs.chemmater.0c02421.
[58] H.T. Baytekin, B. Baytekin, T.M. Hermans, B. Kowalczyk, B.A. Grzybowski, Control of surface charges by radicals as a principle of antistatic polymers protecting electronic circuitry, Science (1979) 341 (2013) 1368–1371, https://doi.org/10.1126/science.1241326.
[59] B.D. Terris, J.E. Stern, ' D. Rugar, H.J. Mamin, Contact Electrification Using Force Microscopy, n.d.
[60] H.T. Baytekin, A.Z. Patashinski, M. Branicki, B. Baytekin, S. Soh, B. A. Grzybowski, The mosaic of surface charge in contact electrification, Science 333 (6040) (2011). ⟨http://science.sciencemag.org/⟩.
[61] C. Yun, S.H. Lee, J. Ryu, K. Park, J.W. Jang, J. Kwak, S. Hwang, Can static electricity on a conductor drive a redox reaction: contact electrification of Au by polydimethylsiloxane, charge inversion in water, and redox reaction, J. Am. Chem. Soc. 140 (2018) 14687–14695, https://doi.org/10.1021/jacs.8b07297.
[62] H.T. Baytekin, B. Baytekin, J.T. Incorvati, B.A. Grzybowski, Material transfer and polarity reversal in contact charging, Angew. Chem. - Int. Ed. 51 (2012) 4843–4847, https://doi.org/10.1002/anie.201200057.
[63] R.K. Pandey, H. Kakehashi, H. Nakanishi, S. Soh, Correlating material transfer and charge transfer in contact electrification, J. Phys. Chem. C 122 (2018) 16154–16160, https://doi.org/10.1021/acs.jpcc.8b04357.
[64] M. Sow, D.J. Lacks, R.M. Sankaran, Effects of material strain on triboelectric charging: Influence of material properties, J. Electrostat. 71 (2013) 396–399, https://doi.org/10.1016/j.elstat.2012.11.021.
[65] M. Sow, D.J. Lacks, R. Mohan Sankaran, Dependence of contact electrification on the magnitude of strain in polymeric materials, J. Appl. Phys. 112 (2012) 084909, https://doi.org/10.1063/1.4761967.
[66] M. Sow, R. Widenor, A. Kumar, S.W. Lee, D.J. Lacks, R.M. Sankaran, Strain-induced reversal of charge transfer in contact electrification, Angew. Chem. 124 (2012) 2749–2751, https://doi.org/10.1002/ange.201107256.
[67] K. Shi, B. Chai, H. Zou, Z. Wen, M. He, J. Chen, P. Jiang, X. Huang, Contact electrification at adhesive interface: boosting charge transfer for high-performance triboelectric nanogenerators, Adv. Funct. Mater. 33 (2023), https://doi.org/10.1002/adfm.202307678.
[68] P.C. Sherrell, A. Sutka, N.A. Shepelin, L. Lapcinskis, O. Verners, L. Germane, M. Timusk, R.A. Fenati, K. Malnieks, A.V. Ellis, Probing Contact electrification: a cohesively sticky problem, ACS Appl. Mater. Interfaces 13 (2021) 44935–44947, https://doi.org/10.1021/acsami.1c13100.
[69] A. Šutka, L. Lapčinskis, D. He, H. Kim, J.D. Berry, J. Bai, M. Knite, A.V. Ellis, C. K. Jeong, P.C. Sherrell, Engineering polymer interfaces: a review toward controlling triboelectric surface charge, Adv. Mater. Interfaces 10 (2023), https://doi.org/10.1002/admi.202300323.
[70] J. Li, N.A. Shepelin, P.C. Sherrell, A.V. Ellis, Poly(dimethylsiloxane) for triboelectricity: from mechanisms to practical strategies, Chem. Mater. 33 (2021) 4304–4327, https://doi.org/10.1021/acs.chemmater.1c01275.
[71] X. Guo, J. You, D. Wei, J. Shao, Z.L. Wang, A generalized model for tribovoltaic nanogenerator, Appl. Phys. Rev. 11 (2024), https://doi.org/10.1063/5.0196998.
[72] J. Shao, M. Willatzen, Z.L. Wang, Theoretical modeling of triboelectric nanogenerators (TENGs), J. Appl. Phys. 128 (2020), https://doi.org/10.1063/5.0020961.
[73] S. Niu, Z.L. Wang, Theoretical systems of triboelectric nanogenerators, Nano Energy 14 (2014) 161–192, https://doi.org/10.1016/j.nanoen.2014.11.034.
[74] S. Niu, S. Wang, L. Lin, Y. Liu, Y.S. Zhou, Y. Hu, Z.L. Wang, Theoretical study of contact-mode triboelectric nanogenerators as an effective power source, Energy Environ. Sci. 6 (2013) 3576–3583, https://doi.org/10.1039/c3ee42571a.
[75] S. Niu, Y.S. Zhou, S. Wang, Y. Liu, L. Lin, Y. Bando, Z.L. Wang, Simulation method for optimizing the performance of an integrated triboelectric nanogenerator energy harvesting system, Nano Energy 8 (2014) 150–156, https://doi.org/10.1016/j.nanoen.2014.05.018.
[76] R.D.I.G. Dharmasena, J.H.B. Deane, S.R.P. Silva, Nature of power generation and output optimization criteria for triboelectric nanogenerators, Adv. Energy Mater. 8 (2018), https://doi.org/10.1002/aenm.201802190.
[77] R.D.I.G. Dharmasena, K.D.G.I. Jayawardena, C.A. Mills, J.H.B. Deane, J. V. Anguita, R.A. Dorey, S.R.P. Silva, Triboelectric nanogenerators: providing a fundamental framework, Energy Environ. Sci. 10 (2017) 1801–1811, https://doi.org/10.1039/c7ee01139c.
[78] R.D.I.G. Dharmasena, K.D.G.I. Jayawardena, C.A. Mills, R.A. Dorey, S.R.P. Silva, A unified theoretical model for triboelectric nanogenerators, Nano Energy 48 (2018) 391–400, https://doi.org/10.1016/j.nanoen.2018.03.073.
[79] J. Shao, M. Willatzen, Y. Shi, Z.L. Wang, 3D mathematical model of contact-separation and single-electrode mode triboelectric nanogenerators, Nano Energy 60 (2019) 630–640, https://doi.org/10.1016/j.nanoen.2019.03.072.
[80] J.J. Shao, T. Jiang, Z.L. Wang, Theoretical foundations of triboelectric nanogenerators (TENGs), Sci. China Technol. Sci. 63 (2020) 1087–1109, https://doi.org/10.1007/s11431-020-1604-9.
[81] W. Zhong, B. Xu, Y. Gao, Engraved pattern spacer triboelectric nanogenerators for mechanical energy harvesting, Nano Energy 92 (2022) 106782, https://doi.org/10.1016/j.nanoen.2021.106782.
[82] H.S. Wang, C.K. Jeong, M.-H. Seo, D.J. Joe, J.H. Han, J.-B. Yoon, K.J. Lee, Performance-enhanced triboelectric nanogenerator enabled by wafer-scale nanogrates of multistep pattern downscaling, Nano Energy 35 (2017) 415–423, https://doi.org/10.1016/j.nanoen.2017.04.012.
[83] L. Liu, X. Yang, L. Zhao, W. Xu, J. Wang, Q. Yang, Q. Tang, Nanowrinkle-patterned flexible woven triboelectric nanogenerator toward self-powered wearable electronics, Nano Energy 73 (2020) 104797, https://doi.org/10.1016/j.nanoen.2020.104797.
[84] M.A.P. Mahmud, J. Lee, G. Kim, H. Lim, K.-B. Choi, Improving the surface charge density of a contact-separation-based triboelectric nanogenerator by modifying the surface morphology, Microelectron. Eng. 159 (2016) 102–107, https://doi.org/10.1016/j.mee.2016.02.066.
[85] Z. Fang, K.H. Chan, X. Lu, C.F. Tan, G.W. Ho, Surface texturing and dielectric property tuning toward boosting of triboelectric nanogenerator performance, J. Mater. Chem. A Mater. 6 (2018) 52–57, https://doi.org/10.1039/C7TA07696G.
[86] Y. Xi, F. Zhang, Y. Shi, Effects of surface micro-structures on capacitances of the dielectric layer in triboelectric nanogenerator: a numerical simulation study, Nano Energy 79 (2021) 105432, https://doi.org/10.1016/j.nanoen.2020.105432.
[87] W. Yang, X. Wang, H. Li, J. Wu, Y. Hu, Z. Li, H. Liu, Fundamental research on the effective contact area of micro-/nano-textured surface in triboelectric nanogenerator, Nano Energy 57 (2019) 41–47, https://doi.org/10.1016/j.nanoen.2018.12.029.
[88] D. Tantraviwat, P. Buarin, S. Suntalelat, W. Sripumkhai, P. Pattamang, G. Rujijanagul, B. Inceesungvorn, Highly dispersed porous polydimethylsiloxane for boosting power-generating performance of triboelectric nanogenerators, Nano Energy 67 (2020) 104214, https://doi.org/10.1016/j.nanoen.2019.104214.
[89] X. Yin, Z. Chen, H. Chen, Q. Wang, Q. Chen, C. Wang, C. Ye, Optimization strategy of triboelectric nanogenerators for high humidity environment service performance, EcoMat 6 (2024), https://doi.org/10.1002/eom2.12493.
[90] J. Kim, S. Jung, D. Kim, J. Gao, Y.S. Lee, H. Park, H. Song, J.M. Baik, Overcoming moisture-induced charge decay in tribo-materials, Adv. Energy Mater. 15 (2025), https://doi.org/10.1002/aenm.202304437.
[91] A. Schella, S. Herminghaus, M. Schröter, Influence of humidity on tribo-electric charging and segregation in shaken granular media, Soft Matter 13 (2017) 394–401, https://doi.org/10.1039/C6SM02041K.
[92] V. Nguyen, R. Yang, Effect of humidity and pressure on the triboelectric nanogenerator, Nano Energy 2 (2013) 604–608, https://doi.org/10.1016/j.nanoen.2013.07.012.
[93] D. Jang, Y. Kim, T.Y. Kim, K. Koh, U. Jeong, J. Cho, Force-assembled triboelectric nanogenerator with high-humidity-resistant electricity generation using hierarchical surface morphology, Nano Energy 20 (2016) 283–293, https://doi.org/10.1016/j.nanoen.2015.12.021.
[94] Q. Zhou, K. Lee, K.N. Kim, J.G. Park, J. Pan, J. Bae, J.M. Baik, T. Kim, High humidity- and contamination-resistant triboelectric nanogenerator with superhydrophobic interface, Nano Energy 57 (2019) 903–910, https://doi.org/10.1016/j.nanoen.2018.12.091.
[95] O. Verners, L. Lapčinskis, L. Ģermane, A. Kasikov, M. Timusk, K. Pudzs, A.V. Ellis, P.C. Sherrell, A. Šutka, Smooth polymers charge negatively: controlling contact electrification polarity in polymers, Nano Energy 104 (2022) 107914, https://doi.org/10.1016/j.nanoen.2022.107914.
[96] A.S. Bhavya, H. Varghese, A. Chandran, K.P. Surendran, Massive enhancement in power output of BoPET-paper triboelectric nanogenerator using 2D-hexagonal boron nitride nanosheets, Nano Energy 90 (2021) 106628, https://doi.org/10.1016/j.nanoen.2021.106628.
[97] J. Ahn, Z.-J. Zhao, J. Choi, Y. Jeong, S. Hwang, J. Ko, J. Gu, S. Jeon, J. Park, M. Kang, D.V. Del Orbe, I. Cho, H. Kang, M. Bok, J.-H. Jeong, I. Park, Morphology-controllable wrinkled hierarchical structure and its application to superhydrophobic triboelectric nanogenerator, Nano Energy 85 (2021) 105978, https://doi.org/10.1016/j.nanoen.2021.105978.
[98] Y. Liu, J. Mo, Q. Fu, Y. Lu, N. Zhang, S. Wang, S. Nie, Enhancement of triboelectric charge density by chemical functionalization, Adv. Funct. Mater. 30 (2020) 2004714, https://doi.org/10.1002/adfm.202004714.
[99] S. Wang, Y. Zi, Y.S. Zhou, S. Li, F. Fan, L. Lin, Z.L. Wang, Molecular surface functionalization to enhance the power output of triboelectric nanogenerators, J. Mater. Chem. A Mater. 4 (2016) 3728–3734, https://doi.org/10.1039/C5TA10239A.
[100] J. Xu, Y. Zou, A. Nashalian, J. Chen, Leverage surface chemistry for high-performance triboelectric nanogenerators, Front Chem. 8 (2020), https://doi.org/10.3389/fchem.2020.577327.
[101] G. Song, Y. Kim, S. Yu, M.-O. Kim, S.-H. Park, S.M. Cho, D.B. Velusamy, S.H. Cho, K.L. Kim, J. Kim, E. Kim, C. Park, Molecularly engineered surface triboelectric nanogenerator by self-assembled monolayers (METS), Chem. Mater. 27 (2015) 4749–4755, https://doi.org/10.1021/acs.chemmater.5b01507.
[102] K.-E. Byun, Y. Cho, M. Seol, S. Kim, S.-W. Kim, H.-J. Shin, S. Park, S. Hwang, Control of triboelectrification by engineering surface dipole and surface electronic state, ACS Appl. Mater. Interfaces 8 (2016) 18519–18525, https://doi.org/10.1021/acsami.6b02802.
[103] W. Sun, D. Yang, N. Luo, H. Li, D. Wang, Influence of surface functionalization on the contact electrification of fabrics, New J. Chem. 46 (2022) 15645–15656, https://doi.org/10.1039/D2NJ02833F.
[104] H. Feng, H. Li, J. Xu, Y. Yin, J. Cao, R. Yu, B. Wang, R. Li, G. Zhu, Triboelectric nanogenerator based on direct image lithography and surface fluorination for biomechanical energy harvesting and self-powered sterilization, Nano Energy 98 (2022) 107279, https://doi.org/10.1016/j.nanoen.2022.107279.
[105] S.H. Park, J. Lee, D.S. Kong, J. Choi, H. Jung, Y.J. Park, H.M. Park, J.H. Jung, M. Lee, Laminating structure for interlayer corona discharge treatment toward ion-based nanogenerators, Small Methods 7 (2023), https://doi.org/10.1002/smtd.202300097.

[106] J. Seo, S. Hajra, M. Sahu, H.J. Kim, Effect of cilia microstructure and ion injection upon single-electrode triboelectric nanogenerator for effective energy harvesting, Mater. Lett. 304 (2021) 130674, https://doi.org/10.1016/j.matlet.2021.130674.
[107] J. Wang, K. Xia, J. liu, T. Li, X. Zhao, B. Shu, H. Li, J. Guo, M. Yu, W. Tang, Z. Zhu, Self-powered silicon PIN photoelectric detection system based on triboelectric nanogenerator, Nano Energy 69 (2020) 104461, https://doi.org/10.1016/j.nanoen.2020.104461.
[108] Y. Fan, S. Li, X. Tao, Y. Wang, Z. Liu, H. Chen, Z. Wu, J. Zhang, F. Ren, X. Chen, E. Fu, Negative triboelectric polymers with ultrahigh charge density induced by ion implantation, Nano Energy 90 (2021) 106574, https://doi.org/10.1016/j.nanoen.2021.106574.
[109] L. Ģērmane, A. Bērziņa, R. Eglītis, M. Iesalnieks, J. Lungevičs, A. Linarts, A. Šutka, L. Lapčinskis, Physical and chemical surface modification of recycled polystyrene films for improved triboelectric properties, Energy Technol. 12 (2024), https://doi.org/10.1002/ente.202400762.
[110] J. Zhao, Y. Shi, Boosting the durability of triboelectric nanogenerators: a critical review and prospect, Adv. Funct. Mater. 33 (2023), https://doi.org/10.1002/adfm.202213407.
[111] Z. Chen, Y. Lu, R. Li, R.J. Orlando, R. Manica, Q. Liu, Liquid-solid triboelectric nanogenerators for a wide operation window based on slippery lubricant-infused surfaces (SLIPS), Chem. Eng. J. 439 (2022) 135688, https://doi.org/10.1016/j.cej.2022.135688.
[112] M. Song, J. Chung, S.-H. Chung, K. Cha, D. Heo, S. Kim, P.T.J. Hwang, D. Kim, B. Koo, J. Hong, S. Lee, Semisolid-lubricant-based ball-bearing triboelectric nanogenerator for current amplification, enhanced mechanical lifespan, and thermal stabilization, Nano Energy 93 (2022) 106816, https://doi.org/10.1016/j.nanoen.2021.106816.
[113] L. Zhou, D. Liu, Z. Zhao, S. Li, Y. Liu, L. Liu, Y. Gao, Z.L. Wang, J. Wang, Simultaneously enhancing power density and durability of sliding-mode triboelectric nanogenerator via interface liquid lubrication, Adv. Energy Mater. 10 (2020) 2002920, https://doi.org/10.1002/aenm.202002920.
[114] X. Liu, J. Zhang, L. Zhang, Y. Feng, M. Feng, N. Luo, D. Wang, Influence of interface liquid lubrication on triboelectrification of point contact friction pair, Tribol. Int 165 (2022) 107323, https://doi.org/10.1016/j.triboint.2021.107323.
[115] G.I. Dzhardimalieva, B.C. Yadav, T.V. Lifintseva, I.E. Uflyand, Polymer chemistry underpinning materials for triboelectric nanogenerators (TENGs): recent trends, Eur. Polym. J. 142 (2021) 110163, https://doi.org/10.1016/j.eurpolymj.2020.110163.
[116] Y. Yu, X. Wang, Chemical modification of polymer surfaces for advanced triboelectric nanogenerator development, Extrem. Mech. Lett. 9 (2016) 514–530, https://doi.org/10.1016/j.eml.2016.02.019.
[117] H. Xiang, Y. Zeng, X. Huang, N. Wang, X. Cao, Z.L. Wang, From triboelectric nanogenerator to multifunctional triboelectric sensors: a chemical perspective toward the interface optimization and device integration, Small 18 (2022) 2107222, https://doi.org/10.1002/smll.202107222.
[118] K.P. Gregory, G.R. Elliott, H. Robertson, A. Kumar, E.J. Wanless, G.B. Webber, V. S.J. Craig, G.G. Andersson, A.J. Page, Understanding specific ion effects and the Hofmeister series, Phys. Chem. Chem. Phys. 24 (2022) 12682–12718, https://doi.org/10.1039/D2CP00847E.
[119] H. Ryu, J. Lee, T. Kim, U. Khan, J.H. Lee, S.S. Kwak, H. Yoon, S. Kim, High-performance triboelectric nanogenerators based on solid polymer electrolytes with asymmetric pairing of ions, Adv. Energy Mater. 7 (2017) 1700289, https://doi.org/10.1002/aenm.201700289.
[120] J.Y. Cheong, J.S.C. Koay, R. Chen, K.C. Aw, T.S. Velayutham, B. Chen, J. Li, C. Y. Foo, W.C. Gan, Maximizing the output power density enhancement of solid polymer electrolyte based-triboelectric nanogenerators via contact electrification-induced ionic polarization, Nano Energy 90 (2021) 106616, https://doi.org/10.1016/j.nanoen.2021.106616.
[121] Y. Wu, Y. Mu, Y. Luo, C. Menon, Z. Zhou, P.K. Chu, S. Feng, Hofmeister effect and electrostatic interaction enhanced ionic conductive organohydrogels for electronic applications, Adv. Funct. Mater. 32 (2022) 2110859, https://doi.org/10.1002/adfm.202110859.
[122] H. Patnam, S.A. Graham, P. Manchi, M.V. Paranjape, J.S. Yu, Single-electrode triboelectric nanogenerators based on ionic conductive hydrogel for mechanical energy harvester and smart touch sensor applications, ACS Appl. Mater. Interfaces 15 (2023) 16768–16777, https://doi.org/10.1021/acsami.3c00386.
[123] J.H. Han, S.Y. Kim, H.C. Moon, Unveiling the impact of tailoring ionic conductor characteristics on the performance of wearable triboelectric nanogenerators, ACS Appl. Mater. Interfaces 16 (2024) 27778–27784, https://doi.org/10.1021/acsami.4c04169.
[124] G. Shi, J. Xiong, W. Wu, Z. Guo, S. Wang, J. Mao, High-strength conductive hydrogels based on the Hofmeister effect for friction nanogenerators, Mater. Today Chem. 40 (2024) 102266, https://doi.org/10.1016/j.mtchem.2024.102266.
[125] M.O. Cicek, M.B. Durukan, B. Yıldız, D. Keskin, D. Doganay, S. Çınar Aygün, M. P. Cakir, H.E. Unalan, Ultra-sensitive bio-polymer iontronic sensors for object recognition from tactile feedback, Adv. Mater. Technol. 8 (2023), https://doi.org/10.1002/admt.202300322.
[126] H. Park, S. Oh, D. Kim, M. Kim, C. Lee, H. Joo, I. Woo, J.W. Bae, J. Lee, Plasticized PVC-gel single layer-based stretchable triboelectric nanogenerator for harvesting mechanical energy and tactile sensing, Adv. Sci. 9 (2022) 2201070, https://doi.org/10.1002/advs.202201070.
[127] Y. Wu, T.J. Cuthbert, Y. Luo, P.K. Chu, C. Menon, Cross-link-dependent ionogel-based triboelectric nanogenerators with slippery and antireflective properties, Small 19 (2023), https://doi.org/10.1002/smll.202301381.
[128] K. Ghosh, C. Iffelsberger, M. Konečný, J. Vyskočil, J. Michalička, M. Pumera, Nanoarchitectonics of triboelectric nanogenerator for conversion of abundant mechanical energy to green hydrogen, Adv. Energy Mater. 13 (2023) 2203476, https://doi.org/10.1002/aenm.202203476.
[129] C. Park, M. Koo, G. Song, S.M. Cho, H.S. Kang, T.H. Park, E.H. Kim, C. Park, Surface-conformal triboelectric nanopores via supramolecular ternary polymer assembly, ACS Nano 14 (2020) 755–766, https://doi.org/10.1021/acsnano.9b07746.
[130] Y. Liu, J. Ping, Y. Ying, Recent progress in 2D-nanomaterial-based triboelectric nanogenerators, Adv. Funct. Mater. 31 (2021) 2009994, https://doi.org/10.1002/adfm.202009994.
[131] R. Zhang, H. Olin, Advances in inorganic nanomaterials for triboelectric nanogenerators, ACS Nanosci. Au 2 (2022) 12–31, https://doi.org/10.1021/acsnanoscienceau.1c00026.
[132] R. Zhang, J. Örtegren, M. Hummelgård, M. Olsen, H. Andersson, H. Olin, A review of the advances in composites/nanocomposites for triboelectric nanogenerators, Nanotechnology 33 (2022) 212003, https://doi.org/10.1088/1361-6528/ac4b7b.
[133] H. Jiang, H. Lei, Z. Wen, J. Shi, D. Bao, C. Chen, J. Jiang, Q. Guan, X. Sun, S.-T. Lee, Charge-trapping-blocking layer for enhanced triboelectric nanogenerators, Nano Energy 75 (2020) 105011, https://doi.org/10.1016/j.nanoen.2020.105011.
[134] Y. Nan, X. Wang, H. Xu, Y. Wu, H. Zhou, Y. Sun, T. Yu, Y. Huang, Synergistic effects of charge transport and trapping in tribomaterials for boosted triboelectric nanogenerators, Nano Energy 110 (2023) 108345, https://doi.org/10.1016/j.nanoen.2023.108345.
[135] N. Wang, D. Yang, W. Zhang, M. Feng, Z. Li, E. Ye, X.J. Loh, D. Wang, Deep trap boosted ultrahigh triboelectric charge density in nanofibrous cellulose-based triboelectric nanogenerators, ACS Appl. Mater. Interfaces 15 (2023) 997–1009, https://doi.org/10.1021/acsami.2c16925.
[136] S.A. Lone, K.C. Lim, K. Kaswan, S. Chatterjee, K.-P. Fan, D. Choi, S. Lee, H. Zhang, J. Cheng, Z.-H. Lin, Recent advancements for improving the performance of triboelectric nanogenerator devices, Nano Energy 99 (2022) 107318, https://doi.org/10.1016/j.nanoen.2022.107318.
[137] M. Kim, D. Park, Md.M. Alam, S. Lee, P. Park, J. Nah, Remarkable output power density enhancement of triboelectric nanogenerators *via* polarized ferroelectric polymers and Bulk MoS_2 composites, ACS Nano 13 (2019) 4640–4646, https://doi.org/10.1021/acsnano.9b00750.
[138] J. Kim, H. Ryu, J.H. Lee, U. Khan, S.S. Kwak, H. Yoon, S. Kim, High permittivity $CaCu_3Ti_4O_{12}$ Particle-induced internal polarization amplification for high performance triboelectric nanogenerators, Adv. Energy Mater. 10 (2020) 1903524, https://doi.org/10.1002/aenm.201903524.
[139] J. Chen, H. Guo, X. He, G. Liu, Y. Xi, H. Shi, C. Hu, Enhancing performance of triboelectric nanogenerator by filling high dielectric nanoparticles into sponge PDMS film, ACS Appl. Mater. Interfaces 8 (2016) 736–744, https://doi.org/10.1021/acsami.5b09907.
[140] J. Chun, J.W. Kim, W. Jung, C.-Y. Kang, S.-W. Kim, Z.L. Wang, J.M. Baik, Mesoporous pores impregnated with Au nanoparticles as effective dielectrics for enhancing triboelectric nanogenerator performance in harsh environments, Energy Environ. Sci. 8 (2015) 3006–3012, https://doi.org/10.1039/C5EE01705J.
[141] I. Appamato, W. Bunriw, V. Harnchana, C. Siriwong, W. Mongkolthanaruk, P. Thongbai, C. Chanthad, A. Chompoosor, S. Ruangchai, T. Prada, V. Amornkitbamrung, Engineering triboelectric charge in natural rubber–Ag nanocomposite for enhancing electrical output of a triboelectric nanogenerator, ACS Appl. Mater. Interfaces 15 (2023) 973–983, https://doi.org/10.1021/acsami.2c17057.
[142] X. Liang, T. Zhao, W. Jiang, X. Yu, Y. Hu, P. Zhu, H. Zheng, R. Sun, C.-P. Wong, Highly transparent triboelectric nanogenerator utilizing in-situ chemically welded silver nanowire network as electrode for mechanical energy harvesting and body motion monitoring, Nano Energy 59 (2019) 508–516, https://doi.org/10.1016/j.nanoen.2019.02.071.
[143] D. Doganay, M.O. Cicek, M.B. Durukan, B. Altuntas, E. Agbahca, S. Coskun, H. E. Unalan, Fabric based wearable triboelectric nanogenerators for human machine interface, Nano Energy 89 (2021) 106412, https://doi.org/10.1016/j.nanoen.2021.106412.
[144] X. Luo, L. Zhu, Y. Wang, J. Li, J. Nie, Z.L. Wang, A flexible multifunctional triboelectric nanogenerator based on MXene/PVA hydrogel, Adv. Funct. Mater. 31 (2021) 2104928, https://doi.org/10.1002/adfm.202104928.
[145] L. Shi, H. Jin, S. Dong, S. Huang, H. Kuang, H. Xu, J. Chen, W. Xuan, S. Zhang, S. Li, X. Wang, J. Luo, High-performance triboelectric nanogenerator based on electrospun PVDF-graphene nanosheet composite nanofibers for energy harvesting, Nano Energy 80 (2021) 105599, https://doi.org/10.1016/j.nanoen.2020.105599.
[146] Y. Qian, J. Yu, F. Zhang, Y. Kang, C. Su, H. Pang, Facile synthesis of sub-10 nm ZnS/ZnO nanoflakes for high-performance flexible triboelectric nanogenerators, Nano Energy 88 (2021) 106256, https://doi.org/10.1016/j.nanoen.2021.106256.
[147] D. Tantraviwat, M. Ngamyingyoud, W. Sripumkhai, P. Pattamang, G. Rujijanagul, B. Inceesungvorn, Tuning the dielectric constant and surface engineering of a $BaTiO_3$/porous PDMS COmposite Film for Enhanced Triboelectric Nanogenerator Output Performance, ACS Omega 6 (2021) 29765–29773, https://doi.org/10.1021/acsomega.1c04222.
[148] S. Sriphan, T. Charoonsuk, T. Maluangnont, N. Vittayakorn, High-performance hybridized composited-based piezoelectric and triboelectric nanogenerators based on $BaTiO_3$/PDMS composite film modified with $Ti_{0.8}O_2$ nanosheets and

silver nanopowders cofillers, ACS Appl. Energy Mater. 2 (2019) 3840–3850, https://doi.org/10.1021/acsaem.9b00513.
[149] L. Lapčinskis, K. Ma¯lnieks, A. Linarts, J. Blu¯ms, K. Šmits, M. Järvekülg, M. Knite, A. Šutka, Hybrid tribo-piezo-electric nanogenerator with unprecedented performance based on ferroelectric composite contacting layers, ACS Appl. Energy Mater. 2 (2019) 4027–4032, https://doi.org/10.1021/acsaem.9b00836.
[150] G. Suo, Y. Yu, Z. Zhang, S. Wang, P. Zhao, J. Li, X. Wang, Piezoelectric and triboelectric dual effects in mechanical-energy harvesting using $BaTiO_3$/polydimethylsiloxane composite film, ACS Appl. Mater. Interfaces 8 (2016) 34335–34341, https://doi.org/10.1021/acsami.6b11108.
[151] J. Wang, H. Wu, Z. Wang, W. He, C. Shan, S. Fu, Y. Du, H. Liu, C. Hu, An ultrafast self-polarization effect in barium titanate filled poly(vinylidene fluoride) composite film enabled by self-charge excitation triboelectric nanogenerator, Adv. Funct. Mater. 32 (2022) 2204322, https://doi.org/10.1002/adfm.202204322.
[152] A. Šutka, K. Mālnieks, L. Lapčinskis, M. Timusk, K. Pudzs, M. Rutkis, Matching the directions of electric fields from triboelectric and ferroelectric charges in nanogenerator devices for boosted performance, IScience 23 (2020) 101011, https://doi.org/10.1016/j.isci.2020.101011.
[153] M.N. Biutty, J.M. Koo, M. Zakia, P.L. Handayani, U.H. Choi, S.Il Yoo, Dielectric control of porous polydimethylsiloxane elastomers with Au nanoparticles for enhancing the output performance of triboelectric nanogenerators, RSC Adv. 10 (2020) 21309–21317, https://doi.org/10.1039/D0RA03522J.
[154] P. Zhang, P.-F. Li, H.-H. Zhang, L. Deng, Effect of Ag nanoparticle size on triboelectric nanogenerator for mechanical energy harvesting, Nanotechnology 33 (2022) 475402, https://doi.org/10.1088/1361-6528/ac8aa2.
[155] Q. Zhou, J.-N. Kim, K.-W. Han, S.-W. Oh, S. Umrao, E.J. Chae, I.-K. Oh, Integrated dielectric-electrode layer for triboelectric nanogenerator based on Cu nanowire-Mesh hybrid electrode, Nano Energy 59 (2019) 120–128, https://doi.org/10.1016/j.nanoen.2019.02.022.
[156] G.-J. Choi, S.-H. Baek, S.-S. Lee, F. Khan, J.H. Kim, I.-K. Park, Performance enhancement of triboelectric nanogenerators based on polyvinylidene fluoride/graphene quantum dot composite nanofibers, J. Alloy. Compd. 797 (2019) 945–951, https://doi.org/10.1016/j.jallcom.2019.05.202.
[157] A. Yar, Z. Kınas, A. Karabiber, A. Ozen, A. Okbaz, F. Ozel, Enhanced performance of triboelectric nanogenerator based on polyamide-silver antimony sulfide nanofibers for energy harvesting, Renew. Energy 179 (2021) 1781–1792, https://doi.org/10.1016/j.renene.2021.07.118.
[158] H. Kang, H.T. Kim, H.J. Woo, H. Kim, D.H. Kim, S. Lee, S. Kim, Y.J. Song, S.-W. Kim, J.H. Cho, Metal nanowire–polymer matrix hybrid layer for triboelectric nanogenerator, Nano Energy 58 (2019) 227–233, https://doi.org/10.1016/j.nanoen.2019.01.046.
[159] M.-K. Kim, M.-S. Kim, H.-B. Kwon, S.-E. Jo, Y.-J. Kim, Wearable triboelectric nanogenerator using a plasma-etched PDMS–CNT composite for a physical activity sensor, RSC Adv. 7 (2017) 48368–48373, https://doi.org/10.1039/C7RA07623A.
[160] X. Pu, J.-W. Zha, C.-L. Zhao, S.-B. Gong, J.-F. Gao, R.K.Y. Li, Flexible PVDF/nylon-11 electrospun fibrous membranes with aligned ZnO nanowires as potential triboelectric nanogenerators, Chem. Eng. J. 398 (2020) 125526, https://doi.org/10.1016/j.cej.2020.125526.
[161] A. Šutka, L. Lapčinskis, O. Verners, L. Ģērmane, K. Smits, A. Pludons, S. Gaidukovs, I. Jeräne, M. Zubkins, K. Pudzs, P.C. Sherrell, J. Blums, Bio-inspired macromolecular ordering of elastomers for enhanced contact electrification and triboelectric energy harvesting, Adv. Mater. Technol. 7 (2022), https://doi.org/10.1002/admt.202200162.
[162] S. Kim, M.K. Gupta, K.Y. Lee, A. Sohn, T.Y. Kim, K.-S. Shin, D. Kim, S.K. Kim, K. H. Lee, H.-J. Shin, D.-W. Kim, S.-W. Kim, Transparent flexible graphene triboelectric nanogenerators, Adv. Mater. 26 (2014) 3918–3925, https://doi.org/10.1002/adma.201400172.
[163] Y. Chen, Z. Tian, X. Wang, N. Ran, C. Wang, A. Cui, H. Lu, M. Zhang, Z. Xue, Y. Mei, P.K. Chu, J. Liu, Z. Hu, Z. Di, 2D transition metal dichalcogenide with increased entropy for piezoelectric electronics, Adv. Mater. 34 (2022) 2201630, https://doi.org/10.1002/adma.202201630.
[164] T. Chekke, R. Narzary, S. Ngadong, B. Satpati, S. Bayan, U. Das, 2D WS2-based single-electrode triboelectric nanogenerator for power generation and motion sensing, J. Electron. Mater. 52 (2023) 2685–2694, https://doi.org/10.1007/s11664-023-10231-1.
[165] B. Hedau, B.-C. Kang, T.-J. Ha, Enhanced triboelectric effects of self-poled MoS_2-embedded PVDF hybrid nanocomposite films for bar-printed wearable triboelectric nanogenerators, ACS Nano 16 (2022) 18355–18365, https://doi.org/10.1021/acsnano.2c06257.
[166] W. He, M. Sohn, R. Ma, D.J. Kang, Flexible single-electrode triboelectric nanogenerators with MXene/PDMS composite film for biomechanical motion sensors, Nano Energy 78 (2020) 105383, https://doi.org/10.1016/j.nanoen.2020.105383.
[167] T. Bhatta, P. Maharjan, H. Cho, C. Park, S.H. Yoon, S. Sharma, M. Salauddin, M. T. Rahman, S.S. Rana, J.Y. Park, High-performance triboelectric nanogenerator based on MXene functionalized polyvinylidene fluoride composite nanofibers, Nano Energy 81 (2021) 105670, https://doi.org/10.1016/j.nanoen.2020.105670.
[168] Z. Chen, Y. Cao, W. Yang, L. An, H. Fan, Y. Guo, Embedding in-plane aligned MOF nanoflakes in silk fibroin for highly enhanced output performance of triboelectric nanogenerators, J. Mater. Chem. A Mater. 10 (2022) 799–807, https://doi.org/10.1039/D1TA08605G.
[169] X. Xie, X. Chen, C. Zhao, Y. Liu, X. Sun, C. Zhao, Z. Wen, Intermediate layer for enhanced triboelectric nanogenerator, Nano Energy 79 (2021) 105439, https://doi.org/10.1016/j.nanoen.2020.105439.
[170] N. Cui, L. Gu, Y. Lei, J. Liu, Y. Qin, X. Ma, Y. Hao, Z.L. Wang, Dynamic behavior of the triboelectric charges and structural optimization of the friction layer for a triboelectric nanogenerator, ACS Nano 10 (2016) 6131–6138, https://doi.org/10.1021/acsnano.6b02076.
[171] J.-H. Zhang, Y. Zhang, N. Sun, Y. Li, J. Du, L. Zhu, X. Hao, Enhancing output performance of triboelectric nanogenerator via large polarization difference effect, Nano Energy 84 (2021) 105892, https://doi.org/10.1016/j.nanoen.2021.105892.
[172] K.N. Kim, S.Y. Kim, S.H. Choi, M. Lee, W. Song, J. Lim, S.S. Lee, S. Myung, All-printed wearable triboelectric nanogenerator with ultra-charged electron accumulation polymers based on MXene nanoflakes, Adv. Electron Mater. 8 (2022) 2200819, https://doi.org/10.1002/aelm.202200819.
[173] P. Bai, G. Zhu, Z.-H. Lin, Q. Jing, J. Chen, G. Zhang, J. Ma, Z.L. Wang, Integrated multilayered triboelectric nanogenerator for harvesting biomechanical energy from human motions, ACS Nano 7 (2013) 3713–3719, https://doi.org/10.1021/nn4007708.
[174] H. Zhou, X. Wei, B. Wang, E. Zhang, Z. Wu, Z.L. Wang, A multi-layer stacked triboelectric nanogenerator based on a rotation-to-translation mechanism for fluid energy harvesting and environmental protection, Adv. Funct. Mater. 33 (2023), https://doi.org/10.1002/adfm.202210920.
[175] W. Du, X. Han, L. Lin, M. Chen, X. Li, C. Pan, Z.L. Wang, A three dimensional multi-layered sliding triboelectric nanogenerator, Adv. Energy Mater. 4 (2014), https://doi.org/10.1002/aenm.201301592.
[176] B. Chen, W. Tang, T. Jiang, L. Zhu, X. Chen, C. He, L. Xu, H. Guo, P. Lin, D. Li, J. Shao, Z.L. Wang, Three-dimensional ultraflexible triboelectric nanogenerator made by 3D printing, Nano Energy 45 (2018) 380–389, https://doi.org/10.1016/j.nanoen.2017.12.049.
[177] A. Šutka, K. Mālnieks, A. Linarts, L. Lapčinskis, O. Verners, M. Timusk, Triboelectric laminates with volumetric electromechanical response for mechanical energy harvesting, Adv. Mater. Technol. 6 (2021), https://doi.org/10.1002/admt.202100163.
[178] A. Šutka, A. Šutka, H. Dundurs, B. del Rosal, M. Iesalnieks, K. Mālnieks, A. Linarts, A.J. Barlow, R.T. Leon, A.V. Ellis, P.C. Sherrell, Recycled polystyrene waste to triboelectric nanogenerators: volumetric electromechanically responsive laminates from same-material contact electrification, Adv. Energy Sustain. Res. 5 (2024), https://doi.org/10.1002/aesr.202300259.
[179] A. Linarts, P.C. Sherrell, K. Mālnieks, A.V. Ellis, A. Šutka, Electrospinning triboelectric laminates: a pathway for scaling energy harvesters, Small 19 (2023), https://doi.org/10.1002/smll.202205563.
[180] Z.Lin Wang, Triboelectric nanogenerators as new energy technology and self-powered sensors–principles, problems and perspectives, Faraday Discuss. 176 (2014) 447–458, https://doi.org/10.1039/c4fd00159a.
[181] S. Lu, W. Lei, L. Gao, X. Chen, D. Tong, P. Yuan, X. Mu, H. Yu, Regulating the high-voltage and high-impedance characteristics of triboelectric nanogenerator toward practical self-powered sensors, Nano Energy 87 (2021) 106137, https://doi.org/10.1016/J.NANOEN.2021.106137.
[182] A.M. El-Mohandes, R. Zheng, Active matching circuit to enhance the generated power of triboelectric nanogenerators, Nano Energy 80 (2021), https://doi.org/10.1016/J.NANOEN.2020.105588.
[183] Y. Zi, S. Niu, J. Wang, Z. Wen, W. Tang, Zhong, L. Wang, ARTICLE Standards and figure-of-merits for quantifying the performance of triboelectric nanogenerators, Nat. Commun. (2015), https://doi.org/10.1038/ncomms9376.
[184] H. Qin, G. Cheng, Y. Zi, G. Gu, B. Zhang, W. Shang, F. Yang, J. Yang, Z. Du, Z. L. Wang, High energy storage efficiency triboelectric nanogenerators with unidirectional switches and passive power management circuits, Adv. Funct. Mater. 28 (2018) 1805216, https://doi.org/10.1002/ADFM.201805216.
[185] G. Cheng, Z.H. Lin, L. Lin, Z.L. Du, Z.L. Wang, Pulsed nanogenerator with huge instantaneous output power density, ACS Nano 7 (2013) 7383–7391, https://doi.org/10.1021/NN403151T/SUPPL_FILE/NN403151T_SI_001.PDF.
[186] W. Shang, G. Gu, W. Zhang, H. Luo, T. Wang, B. Zhang, J. Guo, P. Cui, F. Yang, G. Cheng, Z. Du, Rotational pulsed triboelectric nanogenerators integrated with synchronously triggered mechanical switches for high efficiency self-powered systems, Nano Energy 82 (2021), https://doi.org/10.1016/J.NANOEN.2020.105725.
[187] P. Yang, L. Zhou, Y. Gao, J. Xiao, D. Liu, Z. Zhao, W. Qiao, J. Liu, Z.L. Wang, J. Wang, Achieving high-performance triboelectric nanogenerator by DC pump strategy, Adv. Mater. Technol. (2023) 2201957, https://doi.org/10.1002/ADMT.202201957.
[188] H. Qin, G. Gu, W. Shang, H. Luo, W. Zhang, P. Cui, B. Zhang, J. Guo, G. Cheng, Z. Du, A universal and passive power management circuit with high efficiency for pulsed triboelectric nanogenerator, Nano Energy 68 (2020), https://doi.org/10.1016/J.NANOEN.2019.104372.
[189] G. Cheng, H. Zheng, F. Yang, L. Zhao, M. Zheng, J. Yang, H. Qin, Z. Du, Z.L. Wang, Managing and maximizing the output power of a triboelectric nanogenerator by controlled tip–electrode air-discharging and application for UV sensing, Nano Energy 44 (2018) 208–216, https://doi.org/10.1016/J.NANOEN.2017.11.062.
[190] S. Xu, W. Ding, H. Guo, X. Wang, Z. Lin Wang, Boost the performance of triboelectric nanogenerators through circuit oscillation, Adv. Energy Mater. (2019), https://doi.org/10.1002/aenm.201900772.
[191] L. Cheng, Q. Xu, Y. Zheng, X. Jia, Y. Qin, A self-improving triboelectric nanogenerator with improved charge density and increased charge accumulation speed, Nat. Commun. 9 (1) (2018) 1–8, https://doi.org/10.1038/s41467-018-06045-z.

[192] L. Xu, T.Z. Bu, X.D. Yang, C. Zhang, Z.L. Wang, Ultrahigh charge density realized by charge pumping at ambient conditions for triboelectric nanogenerators, Nano Energy 49 (2018) 625–633, https://doi.org/10.1016/J.NANOEN.2018.05.011.
[193] Y. Bai, L. Xu, S. Lin, J. Luo, H. Qin, K. Han, Z. Lin Wang, Y. Bai, L. Xu, S. Lin, J. Luo, H. Qin, K. Han, Z.L. Wang, Charge pumping strategy for rotation and sliding type triboelectric nanogenerators, Adv. Energy Mater. 10 (2020) 2000605, https://doi.org/10.1002/AENM.202000605.
[194] Z. Yang, Y. Yang, H. Wang, F. Liu, Y. Lu, L. Ji, Z.L. Wang, J. Cheng, Charge pumping for sliding-mode triboelectric nanogenerator with voltage stabilization and boosted current, Adv. Energy Mater. 11 (2021) 2101147, https://doi.org/10.1002/AENM.202101147.
[195] W. Liu, Z. Wang, G. Wang, G. Liu, J. Chen, X. Pu, Y. Xi, X. Wang, H. Guo, C. Hu, Z. L. Wang, Integrated charge excitation triboelectric nanogenerator, Nat. Commun. 10 (1) (2019) 1–9, https://doi.org/10.1038/s41467-019-09464-8.
[196] L. Long, W. Liu, Z. Wang, W. He, G. Li, Q. Tang, H. Guo, X. Pu, Y. Liu, C. Hu, High performance floating self-excited sliding triboelectric nanogenerator for micro mechanical energy harvesting, Nat. Commun. 12 (1) (2021) 1–10, https://doi.org/10.1038/s41467-021-25047-y.
[197] X. Liang, T. Jiang, Y. Feng, P. Lu, J. An, Z.L. Wang, Triboelectric nanogenerator network integrated with charge excitation circuit for effective water wave energy harvesting, Adv. Energy Mater. 10 (2020) 2002123, https://doi.org/10.1002/AENM.202002123.
[198] S. Niu, Z.L. Wang, Theoretical systems of triboelectric nanogenerators, Nano Energy 14 (2014) 161–192, https://doi.org/10.1016/J.NANOEN.2014.11.034.
[199] A. Ghaffarinejad, J.Y. Hasani, R. Hinchet, Y. Lu, H. Zhang, A. Karami, D. Galayko, S.-W. Kim, P. Basset, A conditioning circuit with exponential enhancement of output energy for triboelectric nanogenerator, Nano Energy 51 (2018) 173–184, https://doi.org/10.1016/j.nanoen.2018.06.034.
[200] S. Xu, L. Zhang, W. Ding, H. Guo, X. Wang, Z.L. Wang, Self-doubled-rectification of triboelectric nanogenerator, Nano Energy 66 (2019) 104165, https://doi.org/10.1016/J.NANOEN.2019.104165.
[201] A. Ghaffarinejad, J. Yavand Hasani, D. Galayko, P. Basset, Superior performance of half-wave to full-wave rectifier as a power conditioning circuit for triboelectric nanogenerators: application to contact-separation and sliding mode TENG, Nano Energy 66 (2019), https://doi.org/10.1016/j.nanoen.2019.104137.
[202] A. Ghaffarinejad, J.Y. Hasani, R. Hinchet, Y. Lu, H. Zhang, A. Karami, D. Galayko, S.W. Kim, P. Basset, A conditioning circuit with exponential enhancement of output energy for triboelectric nanogenerator, Nano Energy 51 (2018), https://doi.org/10.1016/j.nanoen.2018.06.034.
[203] G. Qiao, J. Wang, X. Yu, R. Jia, T. Cheng, Z.L. Wang, A bidirectional direct current triboelectric nanogenerator with the mechanical rectifier, Nano Energy 79 (2021) 105408, https://doi.org/10.1016/j.nanoen.2020.105408.
[204] D. Liu, X. Yin, H. Guo, L. Zhou, X. Li, C. Zhang, J. Wang, Z.L. Wang, A constant current triboelectric nanogenerator arising from electrostatic breakdown, Sci. Adv. 5 (2019), https://doi.org/10.1126/sciadv.aav6437.
[205] X. Li, D. Wei, Z.L. Wang, Direct current triboelectric nanogenerators, a perspective from material selections, Nanoenergy Adv. 3 (2023) 343–375, https://doi.org/10.3390/nanoenergyadv3040018.
[206] Z. Zhao, L. Zhou, S. Li, D. Liu, Y. Li, Y. Gao, Y. Liu, Y. Dai, J. Wang, Z.L. Wang, Selection rules of triboelectric materials for direct-current triboelectric nanogenerator, Nat. Commun. 12 (2021) 4686, https://doi.org/10.1038/s41467-021-25046-z.
[207] Z. Zhao, L. Zhou, S. Li, D. Liu, Y. Li, Y. Gao, Y. Liu, Y. Dai, J. Wang, Z.L. Wang, Selection rules of triboelectric materials for direct-current triboelectric nanogenerator, Nat. Commun. 12 (1) (2021) 1–8, https://doi.org/10.1038/s41467-021-25046-z.
[208] L. Zhou, D. Liu, Z. Zhao, S. Li, Y. Liu, L. Liu, Y. Gao, Z.L. Wang, J. Wang, Simultaneously enhancing power density and durability of sliding-mode triboelectric nanogenerator via interface liquid lubrication, Adv. Energy Mater. 10 (2020) 2002920, https://doi.org/10.1002/AENM.202002920.
[209] Y. Gao, D. Liu, L. Zhou, S. Li, Z. Zhao, X. Yin, S. Chen, Z.L. Wang, J. Wang, A robust rolling-mode direct-current triboelectric nanogenerator arising from electrostatic breakdown effect, Nano Energy 85 (2021) 106014, https://doi.org/10.1016/J.NANOEN.2021.106014.
[210] C. Chen, H. Guo, L. Chen, Y.C. Wang, X. Pu, W. Yu, F. Wang, Z. Du, Z.L. Wang, Direct current fabric triboelectric nanogenerator for biomotion energy harvesting, ACS Nano 14 (2020) 4585–4594, https://doi.org/10.1021/ACSNANO.0C00138/SUPPL_FILE/NN0C00138_SI_006.AVI.
[211] S. Niu, X. Wang, F. Yi, Y.S. Zhou, Z.L. Wang, A universal self-charging system driven by random biomechanical energy for sustainable operation of mobile electronics, Nat. Commun. 6 (1) (2015) 1–8, https://doi.org/10.1038/ncomms9975.
[212] K. Zhang, X. Wang, Y. Yang, Z.L. Wang, Hybridized electromagnetic-triboelectric nanogenerator for scavenging biomechanical energy for sustainably powering wearable electronics, ACS Nano 9 (2015), https://doi.org/10.1021/nn507455f.
[213] G. Zhu, J. Chen, T. Zhang, Q. Jing, Z.L. Wang, Radial-arrayed rotary electrification for high performance triboelectric generator, Nat. Commun. 5 (2014), https://doi.org/10.1038/ncomms4426.
[214] X. Pu, M. Liu, L. Li, C. Zhang, Y. Pang, C. Jiang, L. Shao, W. Hu, Z.Lin Wang, X. Pu, M. Liu, L. Li, C. Zhang, Y. Pang, C. Jiang, L. Shao, W. Hu, Z.L. Wang, Efficient charging of Li-ion batteries with pulsed output current of triboelectric nanogenerators, Adv. Sci. 3 (2016) 1500255, https://doi.org/10.1002/ADVS.201500255.
[215] W. Tang, T. Zhou, C. Zhang, F.R. Fan, C.B. Han, Z.L. Wang, A power-transformed-and-managed triboelectric nanogenerator and its applications in a self-powered wireless sensing node, Nanotechnology 25 (2014), https://doi.org/10.1088/0957-4484/25/22/225402.
[216] W. Tang, T. Zhou, C. Zhang, F. Ru Fan, C. Bao Han, Z. Lin Wang, A power-transformed-and-managed triboelectric nanogenerator and its applications in a self-powered wireless sensing node, Nanotechnology 25 (2014) 225402, https://doi.org/10.1088/0957-4484/25/22/225402.
[217] W. Liu, Z. Wang, G. Wang, Q. Zeng, W. He, L. Liu, X. Wang, Y. Xi, H. Guo, C. Hu, Z.L. Wang, Switched-capacitor-convertors based on fractal design for output power management of triboelectric nanogenerator, Nat. Commun. 11 (2020), https://doi.org/10.1038/s41467-020-15373-y.
[218] F. Xi, Y. Pang, W. Li, T. Jiang, L. Zhang, T. Guo, G. Liu, C. Zhang, Z.L. Wang, Universal power management strategy for triboelectric nanogenerator, Nano Energy 37 (2017), https://doi.org/10.1016/j.nanoen.2017.05.027.
[219] F. Xi, Y. Pang, G. Liu, S. Wang, W. Li, C. Zhang, Z.L. Wang, Self-powered intelligent buoy system by water wave energy for sustainable and autonomous wireless sensing and data transmission, Nano Energy 61 (2019), https://doi.org/10.1016/j.nanoen.2019.04.026.
[220] Y. Song, H. Wang, X. Cheng, G. Li, X. Chen, H. Chen, L. Miao, X. Zhang, H. Zhang, High-efficiency self-charging smart bracelet for portable electronics, Nano Energy 55 (2019) 29–36, https://doi.org/10.1016/J.NANOEN.2018.10.045.
[221] H. Zhou, G. Liu, T. Bu, Z. Wang, J. Cao, Z. Wang, Z. Zhang, S. Dong, J. Zeng, X. Cao, C. Zhang, Autonomous cantilever buck switch for ultra-efficient power management of triboelectric nanogenerator, Appl. Energy 357 (2024) 122475, https://doi.org/10.1016/J.APENERGY.2023.122475.
[222] Z. Xiao, Y. Luo, H. Yuan, T. Zheng, S. Xu, G. Dai, J. Yang, Coupling charge pump and BUCK circuits to efficiently enhance the output performance of triboelectric nanogenerator, Nano Energy 115 (2023) 108749, https://doi.org/10.1016/J.NANOEN.2023.108749.
[223] X. Cheng, L. Miao, Y. Song, Z. Su, H. Chen, X. Chen, J. Zhang, H. Zhang, High efficiency power management and charge boosting strategy for a triboelectric nanogenerator, Nano Energy 38 (2017) 438–446, https://doi.org/10.1016/J.NANOEN.2017.05.063.
[224] Z.L. Wang, T. Jiang, L. Xu, Toward the blue energy dream by triboelectric nanogenerator networks, Nano Energy 39 (2017) 9–23, https://doi.org/10.1016/j.nanoen.2017.06.035.
[225] J. Ahn, J. Kim, Y. Jeong, S. Hwang, H. Yoo, Y. Jeong, J. Gu, M. Mahato, J. Ko, S. Jeon, J. Ha, H. Seo, J. Choi, M. Kang, C. Han, Y. Cho, C.H. Lee, J. Jeong, I. Oh, I. Park, All-recyclable triboelectric nanogenerator for sustainable ocean monitoring systems, Adv. Energy Mater. 12 (2022), https://doi.org/10.1002/aenm.202201341.
[226] J. Feng, H. Zhou, Z. Cao, E. Zhang, S. Xu, W. Li, H. Yao, L. Wan, G. Liu, 0.5 m triboelectric nanogenerator for efficient blue energy harvesting of all-sea areas, Adv. Sci. 9 (2022), https://doi.org/10.1002/advs.202204407.
[227] L. Liu, X. Yang, L. Zhao, H. Hong, H. Cui, J. Duan, Q. Yang, Q. Tang, Nodding duck structure multi-track directional freestanding triboelectric nanogenerator toward low-frequency ocean wave energy harvesting, ACS Nano 15 (2021) 9412–9421, https://doi.org/10.1021/acsnano.1c00345.
[228] S. Liu, X. Liang, P. Chen, H. Long, T. Jiang, Z.L. Wang, Multilayered helical spherical triboelectric nanogenerator with charge shuttling for water wave energy harvesting, Small Methods 7 (2023), https://doi.org/10.1002/smtd.202201392.
[229] O. Demircioglu, M.O. Cicek, D. Doganay, G. Gazaloglu, C. Baykal, S. Cinar, H. E. Unalan, Triboelectric nanogenerators for blue energy harvesting in simulated wave conditions, Nano Energy 107 (2023) 108157, https://doi.org/10.1016/j.nanoen.2022.108157.
[230] C. Rodrigues, M. Ramos, R. Esteves, J. Correia, D. Clemente, F. Gonçalves, N. Mathias, M. Gomes, J. Silva, C. Duarte, T. Morais, P. Rosa-Santos, F. Taveira-Pinto, A. Pereira, J. Ventura, Integrated study of triboelectric nanogenerator for ocean wave energy harvesting: performance assessment in realistic sea conditions, Nano Energy 84 (2021) 105890, https://doi.org/10.1016/j.nanoen.2021.105890.
[231] Y. Yang, J. Wen, F. Chen, Y. Hao, X. Gao, T. Jiang, B. Chen, Z.L. Wang, Barycenter self-adapting triboelectric nanogenerator for sea water wave high-entropy energy harvesting and self-powered forecasting in marine meteorology, Adv. Funct. Mater. 32 (2022), https://doi.org/10.1002/adfm.202200521.
[232] Y. Wang, X. Liu, Y. Wang, H. Wang, H. Wang, S.L. Zhang, T. Zhao, M. Xu, Z. L. Wang, Flexible seaweed-like triboelectric nanogenerator as a wave energy harvester powering marine internet of things, ACS Nano 15 (2021) 15700–15709, https://doi.org/10.1021/acsnano.1c05127.
[233] D. Tan, Q. Zeng, X. Wang, S. Yuan, Y. Luo, X. Zhang, L. Tan, C. Hu, G. Liu, Anti-overturning fully symmetrical triboelectric nanogenerator based on an elliptic cylindrical structure for all-weather blue energy harvesting, Nanomicro Lett. 14 (2022) 124, https://doi.org/10.1007/s40820-022-00866-w.
[234] C. Zhang, L. Zhou, P. Cheng, D. Liu, C. Zhang, X. Li, S. Li, J. Wang, Z.L. Wang, Bifilar-pendulum-assisted multilayer-structured triboelectric nanogenerators for wave energy harvesting, Adv. Energy Mater. 11 (2021), https://doi.org/10.1002/aenm.202003616.
[235] R. Ahamed, K. McKee, I. Howard, Advancements of wave energy converters based on power take off (PTO) systems: a review, Ocean Eng. 204 (2020) 107248, https://doi.org/10.1016/j.oceaneng.2020.107248.
[236] J. Wu, L. Qin, N. Chen, C. Qian, S. Zheng, Investigation on a spring-integrated mechanical power take-off system for wave energy conversion purpose, Energy 245 (2022) 123318, https://doi.org/10.1016/j.energy.2022.123318.
[237] S. Yong, J. Wang, L. Yang, H. Wang, H. Luo, R. Liao, Z.L. Wang, Auto-switching self-powered system for efficient broad-band wind energy harvesting based on dual-rotation shaft triboelectric nanogenerator, Adv. Energy Mater. 11 (2021), https://doi.org/10.1002/aenm.202101194.

[238] X. Li, Y. Cao, X. Yu, Y. Xu, Y. Yang, S. Liu, T. Cheng, Z.L. Wang, Breeze-driven triboelectric nanogenerator for wind energy harvesting and application in smart agriculture, Appl. Energy 306 (2022) 117977, https://doi.org/10.1016/j.apenergy.2021.117977.
[239] S. Liu, X. Li, Y. Wang, Y. Yang, L. Meng, T. Cheng, Z.L. Wang, Magnetic switch structured triboelectric nanogenerator for continuous and regular harvesting of wind energy, Nano Energy 83 (2021) 105851, https://doi.org/10.1016/j.nanoen.2021.105851.
[240] Y. Wang, X. Li, X. Yu, J. Zhu, P. Shen, Z.L. Wang, T. Cheng, Driving-torque self-adjusted triboelectric nanogenerator for effective harvesting of random wind energy, Nano Energy 99 (2022) 107389, https://doi.org/10.1016/j.nanoen.2022.107389.
[241] L. He, C. Zhang, B. Zhang, O. Yang, W. Yuan, L. Zhou, Z. Zhao, Z. Wu, J. Wang, Z. L. Wang, A dual-mode triboelectric nanogenerator for wind energy harvesting and self-powered wind speed monitoring, ACS Nano 16 (2022) 6244–6254, https://doi.org/10.1021/acsnano.1c11658.
[242] R. Zhang, R. Xia, X. Cao, N. Wang, Nutshell powder-based green triboelectric nanogenerator for wind energy harvesting, Adv. Mater. Interfaces 9 (2022), https://doi.org/10.1002/admi.202200293.
[243] Y. Feng, L. Zhang, Y. Zheng, D. Wang, F. Zhou, W. Liu, Leaves based triboelectric nanogenerator (TENG) and TENG tree for wind energy harvesting, Nano Energy 55 (2019) 260–268, https://doi.org/10.1016/j.nanoen.2018.10.075.
[244] L. Zhang, B. Meng, Y. Tian, X. Meng, X. Lin, Y. He, C. Xing, H. Dai, L. Wang, Vortex-induced vibration triboelectric nanogenerator for low speed wind energy harvesting, Nano Energy 95 (2022) 107029, https://doi.org/10.1016/j.nanoen.2022.107029.
[245] I.-W. Tcho, W.-G. Kim, J.-K. Kim, D.-W. Kim, S.-Y. Yun, J.-H. Son, Y.-K. Choi, A flutter-driven triboelectric nanogenerator for harvesting energy of gentle breezes with a rear-fixed fluttering film, Nano Energy 98 (2022) 107197, https://doi.org/10.1016/j.nanoen.2022.107197.
[246] W. Sun, Z. Ding, Z. Qin, F. Chu, Q. Han, Wind energy harvesting based on fluttering double-flag type triboelectric nanogenerators, Nano Energy 70 (2020) 104526, https://doi.org/10.1016/j.nanoen.2020.104526.
[247] R. Riemer, A. Shapiro, Biomechanical energy harvesting from human motion: theory, state of the art, design guidelines, and future directions, J. Neuroeng. Rehabil. 8 (2011) 22, https://doi.org/10.1186/1743-0003-8-22.
[248] M. Li, B. Xu, Z. Li, Y. Gao, Y. Yang, X. Huang, Toward 3D double-electrode textile triboelectric nanogenerators for wearable biomechanical energy harvesting and sensing, Chem. Eng. J. 450 (2022) 137491, https://doi.org/10.1016/j.cej.2022.137491.
[249] J. Xia, Z. Zheng, Y. Guo, Mechanically and electrically robust, electro-spun PVDF/PMMA blend films for durable triboelectric nanogenerators, Compos Part A Appl. Sci. Manuf. 157 (2022) 106914, https://doi.org/10.1016/j.compositesa.2022.106914.
[250] M. Qu, L. Shen, J. Wang, N. Zhang, Y. Pang, Y. Wu, J. Ge, L. Peng, J. Yang, J. He, Superhydrophobic, humidity-resistant, and flexible triboelectric nanogenerators for biomechanical energy harvesting and wearable self-powered sensing, ACS Appl. Nano Mater. 5 (2022) 9840–9851, https://doi.org/10.1021/acsanm.2c02026.
[251] Z. Zheng, D. Yu, Y. Guo, Dielectric modulated glass fiber fabric-based single electrode triboelectric nanogenerator for efficient biomechanical energy harvesting, Adv. Funct. Mater. 31 (2021), https://doi.org/10.1002/adfm.202102431.
[252] Y. Yun, S. Jang, S. Cho, S.H. Lee, H.J. Hwang, D. Choi, Exo-shoe triboelectric nanogenerator: toward high-performance wearable biomechanical energy harvester, Nano Energy 80 (2021) 105525, https://doi.org/10.1016/j.nanoen.2020.105525.
[253] M.Y. So, B. Xu, Z. Li, C.L. Lai, C. Jiang, Flexible corrugated triboelectric nanogenerators for efficient biomechanical energy harvesting and human motion monitoring, Nano Energy 106 (2023) 108033, https://doi.org/10.1016/j.nanoen.2022.108033.
[254] Z. Zhou, L. Weng, T. Tat, A. Libanori, Z. Lin, L. Ge, J. Yang, J. Chen, Smart insole for robust wearable biomechanical energy harvesting in harsh environments, ACS Nano 14 (2020) 14126–14133, https://doi.org/10.1021/acsnano.0c06949.
[255] Z. Lin, Y. Wu, Q. He, C. Sun, E. Fan, Z. Zhou, M. Liu, W. Wei, J. Yang, An airtight-cavity-structural triboelectric nanogenerator-based insole for high performance biomechanical energy harvesting, Nanoscale 11 (2019) 6802–6809, https://doi.org/10.1039/C9NR00083F.
[256] H.L. Wang, Z.H. Guo, G. Zhu, X. Pu, Z.L. Wang, Boosting the power and lowering the impedance of triboelectric nanogenerators through manipulating the permittivity for wearable energy harvesting, ACS Nano 15 (2021) 7513–7521, https://doi.org/10.1021/acsnano.1c00914.
[257] Y. Zou, J. Xu, Y. Fang, X. Zhao, Y. Zhou, J. Chen, A hand-driven portable triboelectric nanogenerator using whirligig spinning dynamics, Nano Energy 83 (2021) 105845, https://doi.org/10.1016/j.nanoen.2021.105845.
[258] D. Tan, J. Zhou, K. Wang, C. Zhang, Z. Li, D. Xu, Wearable bistable triboelectric nanogenerator for harvesting torsional vibration energy from human motion, Nano Energy 109 (2023) 108315, https://doi.org/10.1016/j.nanoen.2023.108315.
[259] J. Lee, D. Heo, H. Lyu, J.W. Hur, S. Kim, Z.-H. Lin, J.Y. Park, S. Lee, Slinky-inspired triboelectric–electromagnetic hybrid generator, Curr. Appl. Phys. 49 (2023) 109–114, https://doi.org/10.1016/j.cap.2023.02.020.
[260] L. Feng, Z.L. Wang, X. Cao, L. Zhang, Accordion-inspired parallelly assembled triboelectric nanogenerator: For efficient biomechanical energy harvesting and music responding, Nano Today 49 (2023) 101760, https://doi.org/10.1016/j.nantod.2023.101760.
[261] Q. Zhou, S. Chen, J. Lai, S. Deng, J. Pan, J.M. Baik, F. Xia, High rotational speed hand-powered triboelectric nanogenerator toward a battery-free point-of-care detection system, RSC Adv. 11 (2021) 23221–23227, https://doi.org/10.1039/D1RA03323A.
[262] J. Wang, Z. Jiang, W. Sun, X. Xu, Q. Han, F. Chu, Yoyo-ball inspired triboelectric nanogenerators for harvesting biomechanical energy, Appl. Energy 308 (2022) 118322, https://doi.org/10.1016/j.apenergy.2021.118322.
[263] L.C. Rome, L. Flynn, E.M. Goldman, T.D. Yoo, Generating electricity while walking with loads, Science 309 (1979) (2005) 1725–1728, https://doi.org/10.1126/science.1111063.
[264] I. Ali, M.R. Islam, J. Yin, S.J. Eichhorn, J. Chen, N. Karim, S. Afroj, Advances in smart photovoltaic textiles, ACS Nano 18 (2024) 3871–3915, https://doi.org/10.1021/acsnano.3c10033.
[265] S. Xiang, N. Zhang, X. Fan, From fiber to fabric: progress towards photovoltaic energy textile, Adv. Fiber Mater. 3 (2021) 76–106, https://doi.org/10.1007/s42765-020-00062-8.
[266] N. Li, Z. Yin, W. Zhang, C. Xing, T. Peng, B. Meng, J. Yang, Z. Peng, A triboelectric-inductive hybrid tactile sensor for highly accurate object recognition, Nano Energy 96 (2022) 107063, https://doi.org/10.1016/j.nanoen.2022.107063.
[267] Z. Zhao, Q. Huang, C. Yan, Y. Liu, X. Zeng, X. Wei, Y. Hu, Z. Zheng, Machine-washable and breathable pressure sensors based on triboelectric nanogenerators enabled by textile technologies, Nano Energy 70 (2020) 104528, https://doi.org/10.1016/j.nanoen.2020.104528.
[268] T. Jin, Z. Sun, L. Li, Q. Zhang, M. Zhu, Z. Zhang, G. Yuan, T. Chen, Y. Tian, X. Hou, C. Lee, Triboelectric nanogenerator sensors for soft robotics aiming at digital twin applications, Nat. Commun. 11 (2020) 5381, https://doi.org/10.1038/s41467-020-19059-3.
[269] Z. Song, J. Yin, Z. Wang, C. Lu, Z. Yang, Z. Zhao, Z. Lin, J. Wang, C. Wu, J. Cheng, Y. Dai, Y. Zi, S.-L. Huang, X. Chen, J. Song, G. Li, W. Ding, A flexible triboelectric tactile sensor for simultaneous material and texture recognition, Nano Energy 93 (2022) 106798, https://doi.org/10.1016/j.nanoen.2021.106798.
[270] X. Zhao, Z. Zhang, L. Xu, F. Gao, B. Zhao, T. Ouyang, Z. Kang, Q. Liao, Y. Zhang, Fingerprint-inspired electronic skin based on triboelectric nanogenerator for fine texture recognition, Nano Energy 85 (2021) 106001, https://doi.org/10.1016/j.nanoen.2021.106001.
[271] X. Qu, Z. Liu, P. Tan, C. Wang, Y. Liu, H. Feng, D. Luo, Z. Li, Z.L. Wang, Artificial tactile perception smart finger for material identification based on triboelectric sensing, Sci. Adv. 8 (2022), https://doi.org/10.1126/sciadv.abq2521.
[272] G. Lee, J.H. Son, S. Lee, S.W. Kim, D. Kim, N.N. Nguyen, S.G. Lee, K. Cho, Fingerpad-inspired multimodal electronic skin for material discrimination and texture recognition, Adv. Sci. 8 (2021), https://doi.org/10.1002/advs.202002606.
[273] W. Ye, J. Lin, X. Zhang, Q. Lian, Y. Liu, H. Wang, S. Wu, H. Chen, T. Guo, Self-powered perception system based on triboelectric nanogenerator and artificial neuron for fast-speed multilevel feature recognition, Nano Energy 100 (2022) 107525, https://doi.org/10.1016/j.nanoen.2022.107525.
[274] H. Qiao, S. Sun, P. Wu, Non-equilibrium-growing aesthetic ionic skin for fingertip-like strain-undisturbed tactile sensation and texture recognition, Adv. Mater. 35 (2023), https://doi.org/10.1002/adma.202300593.
[275] X. Rong, J. Zhao, H. Guo, G. Zhen, J. Yu, C. Zhang, G. Dong, Material recognition sensor array by electrostatic induction and triboelectric effects, Adv. Mater. Technol. 5 (2020), https://doi.org/10.1002/admt.202000641.
[276] B. Dong, Y. Yang, Q. Shi, S. Xu, Z. Sun, S. Zhu, Z. Zhang, D.-L. Kwong, G. Zhou, K.-W. Ang, C. Lee, Wearable triboelectric–human–machine interface (THMI) using robust nanophotonic readout, ACS Nano 14 (2020) 8915–8930, https://doi.org/10.1021/acsnano.0c03728.
[277] T. An, D.V. Anaya, S. Gong, L.W. Yap, F. Lin, R. Wang, M.R. Yuce, W. Cheng, Self-powered gold nanowire tattoo triboelectric sensors for soft wearable human-machine interface, Nano Energy 77 (2020) 105295, https://doi.org/10.1016/j.nanoen.2020.105295.
[278] W. Zhang, L. Deng, L. Yang, P. Yang, D. Diao, P. Wang, Z.L. Wang, Multilanguage-handwriting self-powered recognition based on triboelectric nanogenerator enabled machine learning, Nano Energy 77 (2020) 105174, https://doi.org/10.1016/j.nanoen.2020.105174.
[279] X. Pu, Q. Tang, W. Chen, Z. Huang, G. Liu, Q. Zeng, J. Chen, H. Guo, L. Xin, C. Hu, Flexible triboelectric 3D touch pad with unit subdivision structure for effective XY positioning and pressure sensing, Nano Energy 76 (2020) 105047, https://doi.org/10.1016/j.nanoen.2020.105047.
[280] Z. Zhou, K. Chen, X. Li, S. Zhang, Y. Wu, Y. Zhou, K. Meng, C. Sun, Q. He, W. Fan, E. Fan, Z. Lin, X. Tan, W. Deng, J. Yang, J. Chen, Sign-to-speech translation using machine-learning-assisted stretchable sensor arrays, Nat. Electron 3 (2020) 571–578, https://doi.org/10.1038/s41928-020-0428-6.
[281] Y. Luo, Z. Wang, J. Wang, X. Xiao, Q. Li, W. Ding, H.Y. Fu, Triboelectric bending sensor based smart glove towards intuitive multi-dimensional human-machine interfaces, Nano Energy 89 (2021) 106330, https://doi.org/10.1016/j.nanoen.2021.106330.
[282] D. Doganay, O. Demircioglu, M. Cugunlular, M.O. Cicek, O. Cakir, H.U. Kayaci, S. Ç. Aygün, H.E. Unalan, Wet spun core-shell fibers for wearable triboelectric nanogenerators, Nano Energy 116 (2023) 108823, https://doi.org/10.1016/j.nanoen.2023.108823.
[283] Z. Liu, Z. Zhao, X. Zeng, X. Fu, Y. Hu, Expandable microsphere-based triboelectric nanogenerators as ultrasensitive pressure sensors for respiratory and pulse monitoring, Nano Energy 59 (2019) 295–301, https://doi.org/10.1016/j.nanoen.2019.02.057.

[284] R. Guo, Y. Fang, Z. Wang, A. Libanori, X. Xiao, D. Wan, X. Cui, S. Sang, W. Zhang, H. Zhang, J. Chen, Deep learning assisted body area triboelectric hydrogel sensor network for infant care, Adv. Funct. Mater. 32 (2022), https://doi.org/10.1002/adfm.202204803.
[285] Y. Fang, Y. Zou, J. Xu, G. Chen, Y. Zhou, W. Deng, X. Zhao, M. Roustaei, T. K. Hsiai, J. Chen, Ambulatory cardiovascular monitoring via a machine-learning-assisted textile triboelectric sensor, Adv. Mater. 33 (2021), https://doi.org/10.1002/adma.202104178.
[286] X. Qu, J. Xue, Y. Liu, W. Rao, Z. Liu, Z. Li, Fingerprint-shaped triboelectric tactile sensor, Nano Energy 98 (2022) 107324, https://doi.org/10.1016/j.nanoen.2022.107324.
[287] M. Zhu, Z. Sun, T. Chen, C. Lee, Low cost exoskeleton manipulator using bidirectional triboelectric sensors enhanced multiple degree of freedom sensory system, Nat. Commun. 12 (2021) 2692, https://doi.org/10.1038/s41467-021-23020-3.
[288] H. Lei, J. Xiao, Y. Chen, J. Jiang, R. Xu, Z. Wen, B. Dong, X. Sun, Bamboo-inspired self-powered triboelectric sensor for touch sensing and sitting posture monitoring, Nano Energy 91 (2022) 106670, https://doi.org/10.1016/j.nanoen.2021.106670.
[289] D. Bhatia, K.-S. Lee, M.U.K. Niazi, H.-S. Park, Triboelectric nanogenerator integrated origami gravity support device for shoulder rehabilitation using exercise gaming, Nano Energy 97 (2022) 107179, https://doi.org/10.1016/j.nanoen.2022.107179.
[290] Y. Tufan, H. Öztatlı, D. Doganay, A. Buyuksungur, M.O. Cicek, İ.T. Döş, Ç. Berberoğlu, H.E. Unalan, B. Garipcan, B. Ercan, Multifunctional silk fibroin/carbon nanofiber scaffolds for in vitro cardiomyogenic differentiation of induced pluripotent stem cells and energy harvesting from simulated cardiac motion, ACS Appl. Mater. Interfaces 15 (2023) 42271–42283, https://doi.org/10.1021/acsami.3c08601.
[291] Y. Bai, T. Zhao, C. Cai, S. Zhang, J. Wang, Y. Liu, M. Chi, T. Liu, G. Du, Z. Wei, X. Meng, Y. Shao, S. Wang, B. Luo, S. Nie, Rational design of triboelectric materials and devices for self-powered food sensing, Small (2024), https://doi.org/10.1002/smll.202407359.
[292] Z. Tian, Z. Zhu, S. Yue, Y. Liu, Y. Li, Z.-Z. Yu, D. Yang, Self-powered, self-healing, and anti-freezing triboelectric sensors for violation detection in sport events, Nano Energy 122 (2024) 109276, https://doi.org/10.1016/j.nanoen.2024.109276.
[293] M.B. Durukan, M.O. Cicek, D. Doganay, M.C. Gorur, S. Çınar, H.E. Unalan, Multifunctional and physically transient supercapacitors, triboelectric nanogenerators, and capacitive sensors, Adv. Funct. Mater. 32 (2022), https://doi.org/10.1002/adfm.202106066.
[294] O. Cakir, D. Doganay, M. Cugunlular, M.O. Cicek, O. Demircioglu, S. Coskun, H. E. Unalan, Post-treatment optimization for silver nanowire networks in transparent droplet-based TENG sensors, Nano Energy 128 (2024) 109940, https://doi.org/10.1016/j.nanoen.2024.109940.
[295] Y. Du, P. Shen, H. Liu, Z. Zhang, T. Ren, R. Shi, Z. Wang, D. Wei, Conformal self-powered inertial displacement sensor with geometric optimization for in situ noninvasive data acquisition, Adv. Funct. Mater. (2024), https://doi.org/10.1002/adfm.202409602.
[296] Y. Du, P. Shen, H. Liu, Y. Zhang, L. Jia, X. Pu, F. Yang, T. Ren, D. Chu, Z. Wang, D. Wei, Multi-receptor skin with highly sensitive tele-perception somatosensory, Sci. Adv. 10 (2024), https://doi.org/10.1126/sciadv.adp8681.
[297] H.-J. Ko, D.-S. Kwon, S. Pyo, J. Kim, Curved flap array-based triboelectric self-powered sensor for omnidirectional monitoring of wind speed and direction, Nano Energy 102 (2022) 107717, https://doi.org/10.1016/j.nanoen.2022.107717.
[298] H.-J. Ko, D.-S. Kwon, K. Bae, J. Kim, Self-suspended shell-based triboelectric nanogenerator for omnidirectional wind-energy harvesting, Nano Energy 96 (2022) 107062, https://doi.org/10.1016/j.nanoen.2022.107062.
[299] Z. Wang, Y. Wang, Q. Gao, G. Bao, T. Cheng, Z.L. Wang, Triboelectric fluid sensors: principles, development, and perspectives, Adv. Mater. Technol. 8 (2023), https://doi.org/10.1002/admt.202201029.
[300] Q. Xu, Y. Lu, S. Zhao, N. Hu, Y. Jiang, H. Li, Y. Wang, H. Gao, Y. Li, M. Yuan, L. Chu, J. Li, Y. Xie, A wind vector detecting system based on triboelectric and photoelectric sensors for simultaneously monitoring wind speed and direction, Nano Energy 89 (2021) 106382, https://doi.org/10.1016/j.nanoen.2021.106382.
[301] J. Gu, X. Gong, T. Lu, L. Zheng, H. Li, Self-powered wind detection and positioning system for hot air balloon based on multi-module triboelectric nanogenerator, Nano Energy 116 (2023) 108791, https://doi.org/10.1016/j.nanoen.2023.108791.
[302] S. Li, Z. Zhao, D. Liu, J. An, Y. Gao, L. Zhou, Y. Li, S. Cui, J. Wang, Z.L. Wang, A self-powered dual-type signal vector sensor for smart robotics and automatic vehicles, Adv. Mater. 34 (2022), https://doi.org/10.1002/adma.202110363.
[303] K. Dai, X. Wang, F. Yi, C. Jiang, R. Li, Z. You, Triboelectric nanogenerators as self-powered acceleration sensor under high-g impact, Nano Energy 45 (2018) 84–93, https://doi.org/10.1016/j.nanoen.2017.12.022.
[304] X. Yin, D. Liu, L. Zhou, X. Li, G. Xu, L. Liu, S. Li, C. Zhang, J. Wang, Z.L. Wang, A motion vector sensor via direct-current triboelectric nanogenerator, Adv. Funct. Mater. 30 (2020), https://doi.org/10.1002/adfm.202002547.
[305] Z. Xie, Z. Zeng, F. Yang, J. Lv, Y. Wang, R. Wu, J. Liu, Z.L. Wang, T. Cheng, Sliding triboelectric circular motion sensor with real-time hardware processing, Adv. Mater. Technol. 6 (2021), https://doi.org/10.1002/admt.202100655.
[306] C. Liu, Y. Wang, N. Zhang, X. Yang, Z. Wang, L. Zhao, W. Yang, L. Dong, L. Che, G. Wang, X. Zhou, A self-powered and high sensitivity acceleration sensor with V-Q-a model based on triboelectric nanogenerators (TENGs), Nano Energy 67 (2020) 104228, https://doi.org/10.1016/j.nanoen.2019.104228.
[307] H. Luo, J. Du, P. Yang, Y. Shi, Z. Liu, D. Yang, L. Zheng, X. Chen, Z.L. Wang, Human–machine interaction via dual modes of voice and gesture enabled by triboelectric nanogenerator and machine learning, ACS Appl. Mater. Interfaces 15 (2023) 17009–17018, https://doi.org/10.1021/acsami.3c00566.
[308] H. Yang, J. Lai, Q. Li, X. Zhang, X. Li, Q. Yang, Y. Hu, Y. Xi, Z.L. Wang, High-sensitive and ultra-wide spectrum multifunctional triboelectric acoustic sensor for broad scenario applications, Nano Energy 104 (2022) 107932, https://doi.org/10.1016/j.nanoen.2022.107932.
[309] Y. Jiang, Y. Zhang, C. Ning, Q. Ji, X. Peng, K. Dong, Z.L. Wang, Ultrathin eardrum-inspired self-powered acoustic sensor for vocal synchronization recognition with the assistance of machine learning, Small 18 (2022), https://doi.org/10.1002/smll.202106960.
[310] H. Yao, Z. Wang, Y. Wu, Y. Zhang, K. Miao, M. Cui, T. Ao, J. Zhang, D. Ban, H. Zheng, Intelligent sound monitoring and identification system combining triboelectric nanogenerator-based self-powered sensor with deep learning technique, Adv. Funct. Mater. 32 (2022), https://doi.org/10.1002/adfm.202112155.
[311] H. Guo, X. Pu, J. Chen, Y. Meng, M.-H. Yeh, G. Liu, Q. Tang, B. Chen, D. Liu, S. Qi, C. Wu, C. Hu, J. Wang, Z.L. Wang, A highly sensitive, self-powered triboelectric auditory sensor for social robotics and hearing aids, Sci. Robot. 3 (2018), https://doi.org/10.1126/scirobotics.aat2516.
[312] H. Sun, X. Gao, L. Guo, L. Tao, Z.H. Guo, Y. Shao, T. Cui, Y. Yang, X. Pu, T. Ren, Graphene-based dual-function acoustic transducers for machine learning-assisted human–robot interfaces, InfoMat 5 (2023), https://doi.org/10.1002/inf2.12385.
[313] R. Li, D. Wei, Z. Wang, Synergizing machine learning algorithm with triboelectric nanogenerators for advanced self-powered sensing systems, Nanomaterials 14 (2024) 165, https://doi.org/10.3390/nano14020165.